Sensing and Imaging Biomolecules with Plasmonic Nanoparticle Assemblies Coupled with Darkfield Microscopy

Nguyen Hoang Le

A Dissertation

submitted to the Faculty of Graduate Studies

in Partial Fulfillment of the Requirements for the Degree of

Doctor of Philosophy

Department of Chemistry

York University

Toronto, Ontario

March 2022

Abstract

Noble metal nanoparticles exhibit unique optical properties arising from the resonant oscillations of their conduction electrons with light. This phenomenon is called localized surface plasmon resonance (LSPR). The LSPR frequency is extremely sensitive to the size, shape, refractive index at the metal-dielectric interface, and other nearby metal nanoparticles. In an assembly of proximal nanoparticles, the LSPR of individual particles can couple to yield enhanced light scattering and large spectral shifts, which are useful for many applications including diagnostics and sensing. This dissertation presents a complex nanostructure comprising a core gold nanoparticle surrounded by multiple satellite gold nanoparticles for biosensing application. Chapter 2 introduces the fabrication and characterization of the core-satellite assemblies via a layer-by-layer process. Using ATP-aptamer as the linker, we demonstrated the detection of ATP based on the disassembly of the nanostructure, which can be readily captured by darkfield microscopy. The detection limit, dynamic range, and sensitivity can be tuned by controlling the size of the assembly. We found that the aptamer-linked nanoparticle assemblies were selective to only ATP, and not other adenine-containing compounds. Additionally, sensing of ATP in buffer and in bulk cell lysates was demonstrated. Chapter 3 presents the methodology for detecting ATP directly from lysed cells, down to the single-cell level without the need for purification or extraction. The intracellular ATP levels of two ovarian cancer cell lines were quantified to elucidate the differences and cellular distribution, and the potential of the stick-and-peel platform for mapping the microenvironment of 2D heterogeneous surfaces was demonstrated. In chapter 4, the optical properties of nanoparticle assemblies were tuned by changing the morphology of the nano building block, where the incorporation of gold nanoshells as satellites led to an extended redshift of LSPR to a much longer wavelength compared with using solid gold nanoparticles as

satellites. This tunability in the LSPR of the assemblies allows for color-based analysis and color-coding of the plasmonic sensors. Lastly, Chapter 5 outlines the development of a multiplexed assay using the nanoparticle assemblies. Two types of assemblies, targeting either ATP or a nucleic acid (DNA-210), were fabricated with different DNA linkers in the same sensing area. The multiplexing was demonstrated by the selective disassembly process. Moreover, the ability to tune the optical properties of nanostructures using different morphologies was integrated; two different morphology of nanostructures, i.e. solid-solid and solid-shell nanostructures, for two targets, ATP and DNA-210, respectively, were fabricated. Based on a difference in scattered color, two types of biosensors among thousands of nanoparticle assemblies can be easily identified. Finally, we demonstrated duplex detection based on the change in the scattering intensity and the color read-out. Reflecting on the contributions of our work, this dissertation advances the fundamental knowledge and practical design of chip-based sensing platforms comprising complex plasmonic nanostructures. The work contributes to the sensing field by addressing some of the challenges in point-of-care or point-of-need measurement applications and provides an alternative bioanalytical tool for single-cell based analysis.

Acknowledgments

I would like to express my deep gratitude to everyone who has helped me throughout my time in graduate school. First, I would like to offer my special thanks to Professor Jennifer Chen, my advisor, for the support, encouragement, and guidance during my Ph.D. study. Without her persistent help, this thesis would not have been possible. I also thank her for teaching me how to be a professional researcher, from effective writing, presentation skills to career development. I would also like to thank my committee members, Dr. Derek Wilson and Dr. Ryan Hili for the constructive feedback and support; your advising has strengthened my knowledge and encouraged me to think outside of my field. I would also like to thank Dr. Philip Johnson and Dr. Christa Brosseau for taking the time to attend my examination.

During my research, I received great assistance from many technical staffs. I would like to thank Gang Ye for his introduction to cell culture and his work on cell preparation. Also, I would like to extend my thanks to Magdalena Jaklewicz and Ilya Gourevich for their technical help with SEM.

I must thank all of the Chen group members with whom I have worked, past and present: Brian Malile, Gurbrinder Ghotra, Nicole Cathcart, Rithu Devasya, Shakiba Ghaffari, Nicholas Tulsiram, Fred Wong, and Christopher Kerr for their wonderful collaboration and friendly environment.

Lastly, my deep and sincere gratitude to my family for all of the love, support, and encouragement along with this journey. To my parents, thank you for giving me the opportunity to study abroad, and I cannot thank them enough for the encouragement and moral support they have provided. To my little sisters, thank you for taking care of our mom and dad and always being there for me. To my girls, Michelle and Emma, you are my inspiration to achieve greatness and

bring so much joy to my life. To my wife, thank you for sharing this journey along with me. She has supported me since day one and I would not be able to accomplish it without her.

Table of Contents

List of Figures

CHAPTER 1

CHAPTER 2

CHAPTER 4

CHAPTER 5

CHAPTER 6

APPENDIX

List of Tables

List of Schemes

List of Abbreviations

3BP	3-bromopyruvate
ACE	aptamer-complementary element
ADDL	amyloid-beta-derived diffusible ligand
ADP	adenosine-5’-diphosphate
AgNPs	silver nanoparticles
AMP	adenosine-5’-monophosphate
APTMS	(3-aminopropyl) triethoxysilane
ATP	adenosine-5’-triphosphate
Au60	60 nm diameter of spherical gold nanoparticles
Au30	30 nm diameter of spherical gold nanoparticles
AuNPs	gold nanoparticles
BSA	bovine serum albumin
BSPP	bis(p-sulfonatophenyl) phenyl phosphine
CCD	charge-coupled device
CTP	cytidine-5’-triphosphate
DF	dark field
DMEM	Dulbecco's modified eagle medium
FRET	Förster resonance energy transfer
FDTD	finite-difference time-domain method
GTP	guanine-5’-triphosphate
HEPES	4-(2-hydroxyethyl)-1-piperazineethanesulfonic acid
HPLC	high-peformance liquid chromatography
HSI	hue, saturation and intensity analysis
KCN	potassium cyanide
LBL	layer by layer
LSPR	localized surface plasmon resonance
miRNA	micro RNA
Mpeg-SVA	poly (ethylene glycol) methyl ether-succinimidyl valerate
MUA	mercaptoundecanoic acid
NaCl	sodium chloride

NPs	nanoparticles
PB	phosphate buffer
PDMS	polydimethylsiloxane
PVP	poly(vinylpyrrolidone)
QDs	quantum dots
SELEX	systematic evolution of ligands by exponential enrichment
SEM	scanning electron microscope
SERS	surface-enhanced Raman spectroscopy
ssDNA	single-stranded DNA
SiO_2	silicon dioxide
SDS	sodium dodecylsulfate
TCEP	tris(2-carboxyethyl)phosphine hydrochloride
TEM	transmission electron microscopy
Triton X-100	2-[4-(2,4,4-trimethylpentan-2-yl)phenoxy]ethanol
UV-vis	ultraviolet-visible

Chapter 1 - Introduction

Localized surface plasmon resonance in noble metal nanoparticles gives rise to unique optical properties such as strong scattering and absorption of light. Therefore, plasmonic nanoparticles (NPs) are attractive for applications, including diagnostics, sensing, and photothermal therapy. Metal nanoparticles can be readily conjugated with biological molecules, including proteins and nucleic acids, and have additional advantages such as biocompatibility and photostability. For instance, the strong light scattering of bioconjugated gold nanoparticles (AuNPs) allows for imaging or detecting of a specific target using simple dark-field (DF) optical microscopy. Notably, the plasmon coupling in complex nanostructures (i.e., the core-satellite assemblies) results in dramatically enhanced and tunable optical properties, opening up new opportunities for optical sensing.

This chapter introduces the pertinent background information for the scope of this Ph.D. work, beginning with the fundamentals of LSPR and plasmon coupling, followed by the various concepts of LSPR-based sensing, including changes in the local refractive index and distance-dependent plasmon coupling. The enhanced optical properties with nanostructures such as dimer and core-satellite assemblies are explained. Additionally, we lay the groundwork of how it is possible to tune the LSPR of core-satellite nanostructures through variations of their size, interparticle distance, and composition that allow us to tailor the design of nanostructures for specific applications. Lastly, the fundamental science pertaining to aptamer, focusing on the ATP aptamer that was used as the linker in the thesis, is introduced.

1.1 Localized Surface Plasmon Resonance in Metal Nanoparticles

Noble metal nanoparticles exhibit strong scattering and absorption of light because of their interaction with the electromagnetic field of the incident light, which leads to a collective oscillation of the free electrons in the metal. Figure 1.1 depicts the LSPR phenomenon of spherical nanoparticles in which the particles' free electrons participate in the collective oscillation.[1] As the wave of the light passes, the electron density is polarized to one side, leading to a restoring force from the Coulombic attraction between electrons and nuclei. The resulting oscillation of the electron cloud relative to the nuclear framework occurs at a specific frequency of light.

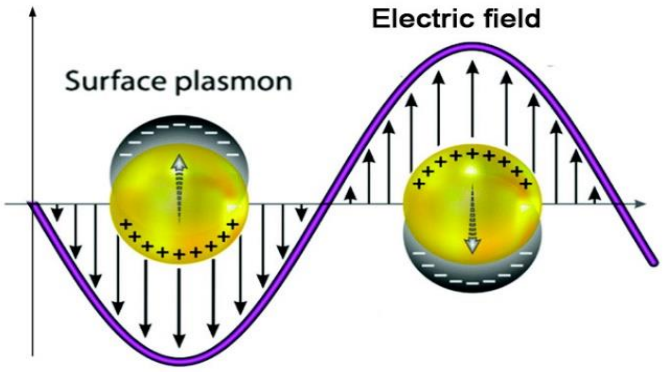

Figure 1.1. Schematic diagram illustrating the localized surface plasmon on a spherical nanoparticle surface. Reprinted with permission from ref 1. Copyright 2020 Royal Society of Chemistry.

The phenomenon of LSPR strongly depends on the size and shape of the nanoparticle and the dielectric constant of the material.[2] When the shape of the nanoparticle changes, the electronic polarization changes correspondingly, causing a difference in the oscillation frequency. For example, spherical AuNPs exhibit a single LSPR peak while Au nanorods have two resonances: one due to plasmon oscillation along the nanorod's short axis (transverse mode) and another due to plasmon oscillation along the long axis (longitudinal mode). Additionally, increasing nanoparticle size leads to an increase in the density of electrons and charge distribution;

consequently the retardation effect in larger particles often leads to a redshift and broadening of the LSPR peak.[3] Changing the refractive index of the surrounding medium also affects the LSPR frequency. In practice, chemical adsorption on the surface or a change of the solvent will alter the refractive index, resulting in shifts of the LSPR.[4] This is one of the fundamental mechanisms of LSPR-based sensing.

To understand the factors that affect LSPR, Mie theory is often evoked. By solving Maxwell's equations, Mie theory describes the scattering and absorption of light by spherical particles resulting from the interaction of the electromagnetic waves with a small sphere.[5] For a metal nanosphere with a particle size much smaller than the wavelength of light (λ), with an assumption of only dipole oscillations contributing to the extinction cross-section, C_{ext}, the nanoparticle extinction cross-section is defined as

$$C_{ext}(\lambda) = \frac{24\pi^2 R^3 \varepsilon_m^{\frac{3}{2}} N}{\lambda} \frac{\varepsilon_i}{(\varepsilon_r + \chi\varepsilon_m)^2 + \varepsilon_i^2} \qquad \text{Eqn. 1}$$

where R is the radius of the nanoparticle; N is the density of free electrons in the particle; ε_m is the dielectric constant of the surrounding medium which is related to the refractive index of the medium n ($\varepsilon_m = n^2$); ε_i and ε_r are the imaginary and real part of the complex dielectric function of the bulk metallic nanoparticle, respectively; χ is a factor relating to the shape of the particle which describes how easily electrons are polarized in a particular geometry (e.g. a high value of the shape factor χ implies greater ease of the polarization of the electrons at the interface of the nanoparticle and the medium). For example, χ is two for a spherical particle, while it can increase up to 20 for a nanorod depending on the aspect ratio (length/width).[6–8] From equation 1, the maximum C_{ext} (i.e. LSPR peak) is observed when the condition of $\varepsilon_r = -\chi\varepsilon_m$ is satisfied. The real and imaginary components of the complex dielectric functions of bulk silver and gold are shown in Figure 1.2a-

b, which illustrates where the condition for maximum C_{ext} is met.[9] For spherical nanoparticles in water ($\varepsilon_m = 1.7$), ε_r is equal to −3.4 (i.e. $\varepsilon_r = -2\varepsilon_m$) at 520 nm for gold and ca. 400 nm for silver (Fig. 1.2a).[10] When the resonant condition for Ag and Au is met, their LSPR, such as shown in Figure 1.2c, is within the visible region; therefore, they are often used as colorants and optical transducers for sensing applications. It should be noted that the imaginary part of the dielectric function, which describes the material's ability to dissipate energy, also affects the broadening of the LSPR peak. Because the imaginary part of the dielectric function of Ag is less than that of Au across the visible region, as shown in Figure 1.2b, less plasmon damping occurs and a higher scattering efficiency and narrower plasmon bandwidth are observed for Ag compared with Au NPs. For sensing applications based on the spectral shift of LSPR, the sharper and narrower LSPR of Ag NPs is significantly advantageous over that of Au NPs; however, Au is often chosen over Ag because of its chemical stability and resistance to oxidation.

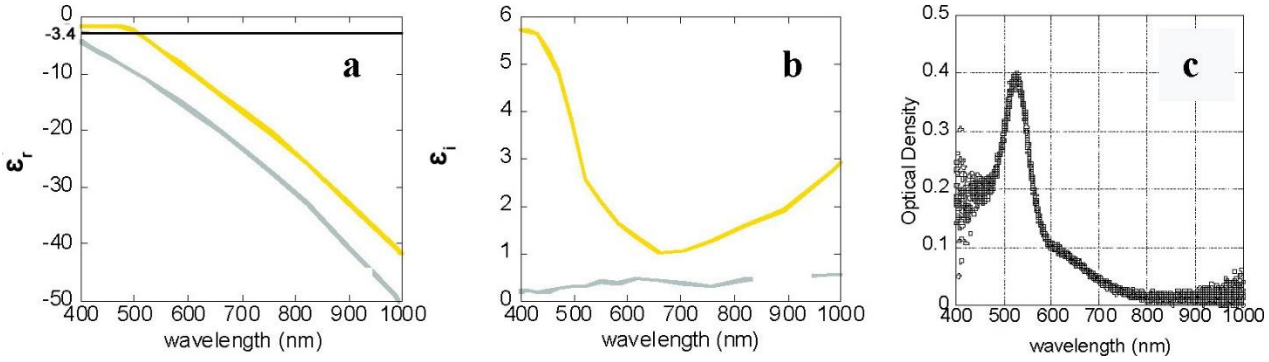

Figure 1.2. (a) Real and (b) imaginary parts of the complex dielectric functions of silver (grey) and gold (yellow). (c) Absorption spectrum of gold colloid solution. Reprinted with permission from ref 10. Copyright 2011 American Chemical Society.

1.1.1 Biosensing Based on Refractive-Index Changes

When the molecular targets get close to the surface of a noble metal nanostructure, the refractive index surrounding the nanostructure is altered. Thus, the molecular adsorption at the

surface of the nanostructures directly leads to local refractive index changes; these changes can then be monitored via the LSPR spectral shift. The spectral shift induced by the refractive index change is widely used as an optical sensing mechanism[11,12] and is described by equation 2[13]

$$\Delta\lambda = m\Delta n\left[1 - exp\left(\frac{-2d}{l_d}\right)\right] \qquad \text{Eqn. 2}$$

where m is the bulk refractive index response of the NPs, also known as the sensitivity factor (in nm per refractive index unit, nm/RIU), Δn is the change in refractive index in RIU induced by analyte, d is the effective thickness of the adsorbed layer (in nm), and l_d is the characteristic electromagnetic field decay length (in nm). In a sensing platform based on LSPR spectral shifts, the sensing performance depends both on the degree of spectral shift per unit of refractive index and plasmon characteristics (i.e., spectral linewidth). In general, a narrower LSPR peak allows more efficient detection of the spectral shift and precise analysis of sensing events, leading to improved sensitivity. A figure of merit (FOM) obtained by dividing the sensitivity by the full-width half maximum (FWHM) of the peak is used to characterize a nanoparticle's sensing capabilities.

$$FOM = \frac{\Delta\lambda/_{\Delta n}}{FWHM} \qquad (eq\ 3)$$

where $\Delta\lambda$ (e.g., eV or nm) is the amount of spectral shift resulting from the dielectric medium, and FWHM (e.g. eV or nm) is the full width of the plasmon resonance at half its maximum value. It should be noted that the FOM depends on the material of the nanoparticles. For example, silver is the most sensitive to refractive index changes among most plasmonic materials due to the high absolute value of the real part of the dielectric constant.[14,15] Silver also has a low imaginary part of the dielectric constant,[7,10] which decreases damping and thus yields sharp LSPR peaks.

An approach to enhance sensitivity is to increase the spectral shift as much as possible in response to refractive index changes. This can be achieved by tuning the nanostructure geometry such as the size and shape.[3,16] For example, when the NP volume increases, sensitivity also increases because more molecules would effectively change the refractive index around a larger nanoparticle. It should be noted that larger spherical particles have greater sensitivity factors (or m-values), but the size also affects the broadening of LSPR due to damping and retardation, leading to a decrease in resolution.[17] Alternatively, sensitivity can be tuned via different shapes of nanoparticles without changing particle volume. For example, triangular prisms are found to be more sensitive to changes in RI than nanospheres, at 350 nm/ RIU vs 160 nm/RIU, respectively.[18] Recent theoretical studies show the refractive-index sensitivity linearly increases as the LSPR frequency of the same material shifts to longer wavelengths.[19] In general, it is suggested that the more red-shifted (lower in energy) LSPR is, the higher is its refractive index sensitivity.[10]

An example of refractive index-based sensing is the use of silver prisms to detect amyloid-beta-derived diffusible ligand (ADDL) for the early diagnosis of Alzheimer's disease.[12] Figure 1.3a shows a sandwich assay upon binding of the protein target. The silver prism array was firstly functionalized with an antibody for the ADDL molecules and the ADDLs were then allowed to bind to the antibodies. Finally, a second capping antibody was introduced that can bind to the surface-bound ADDL and complete the sandwich assay. The sandwich assay was used to analyze the ADDL proteins extracted from the cerebrospinal fluid of Alzheimer's patient sample; a spectral shift ~ 44 nm (Fig. 1.3c) in the LSPR of silver prisms was detected compared with negligible shifts in the control patient sample (Fig. 1.3b). The platform was also used to measure the binding kinetics of ADDL and demonstrated extremely low detection concentrations in the femtomolar range. The conventional refractive index-based sensing platform shows great sensing performance

metrics such as high sensitivity and potential for multiplexing; however, it is still limited by the resolution of the spectral shift induced by the change in refractive index surrounding the particles. For example, the detection of small molecules remains a challenge because of the insignificant change in refractive index upon binding to the nanoparticle surface.[16] To increase the limit of detection, many strategies have been explored such as changing the nanoparticle's material, size, and shape[3] or amplifying the detection signal, including the incorporation of enzyme[20] and coupling of plasmonic nanoparticles.[21]

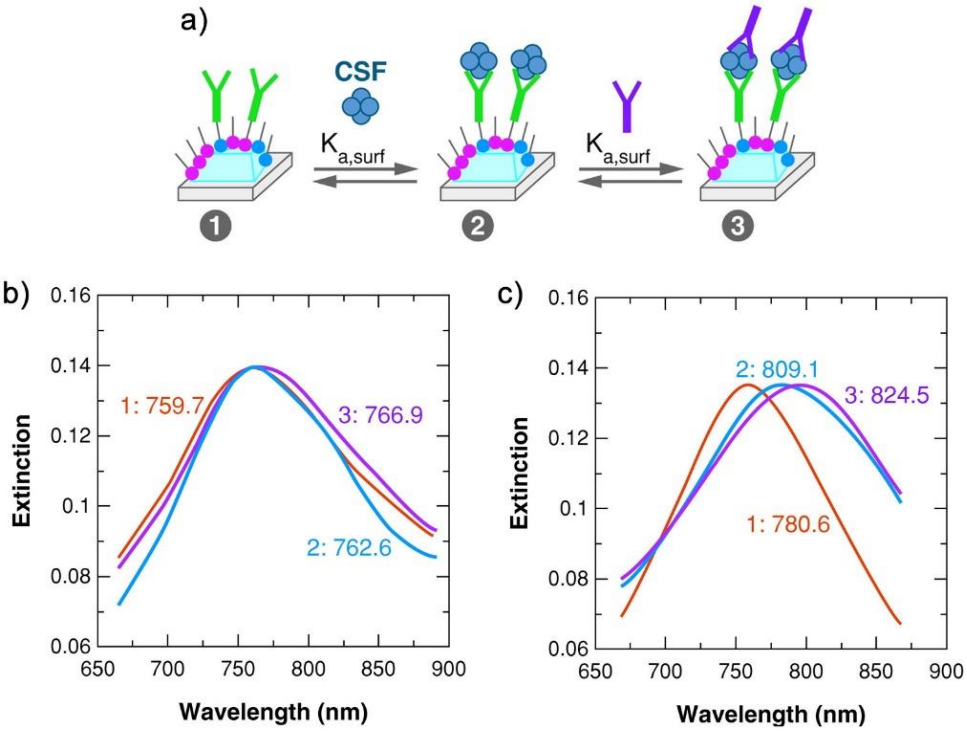

Figure 1.3. LSPR-based sensing assay using silver prism for detecting amyloid-beta-derived diffusible ligand (ADDL) in human cerebrospinal fluid (CSF) samples using the antibody sandwich assay. (a) The three steps of assay include (1) functionalization with 100-mM anti-ADDL, (2) the introduction of human CSF, and (3) the introduction of the second capping antibody. (b) Localized surface plasmon resonance spectra for each step of the assay for an age-matched control patient. (c) LSPR spectra for each step of the assay for an Alzheimer's patient. Reprinted with permission from ref 12. Copyright 2005 American Chemical Society.

Furthermore, interest in multiplexing has grown because the ability to detect multiple targets offers advantages such as the reduction of sample volume and cost, and especially the acquisition of greater information from a single experiment. AuNPs are widely used as the optical transducer for multiplexed sensing. Van Duyne and co-workers developed the first multiplexed sensor using plasmonic nanoarray combined with microscopy (Fig 1.4a).[22] A single-chip array comprises five different regions consisting of gold nanodiscs with a diameter of 190 nm and heights that vary from 20 to 100 nm. The feasibility of multiplexed detection was demonstrated by simultaneously exposing different nanoarray wells to varying concentrations of targets. Recent work by the Kurabayashi group demonstrated that the spectral shift with gold nanorods could achieve the multiplexing of cytokine antigens (Fig. 1.4b). The microfluidic channels containing gold nanorods functionalized with different antibody probes combined with darkfield microscopy can simultaneously detect different cytokine proteins from the human blood sample.[23] Overall, this multiplexed sensing platform based on the spectral shift is complicated to perform as it requires special instrumentation (i.e., liquid tunable filter), expertise in lithography, and the need for mathematical algorithms for fitting. Along with the increase in the use of plasmonic NPs and microfluidic for multiplexing, it is necessary to design a simple and rapid assay. Towards these goals, developing closely-coupled nanostructures can significantly aid in improving the simplicity in fabrication, signal detection and analysis, and sensitivity and selectivity (see Chapter 5).

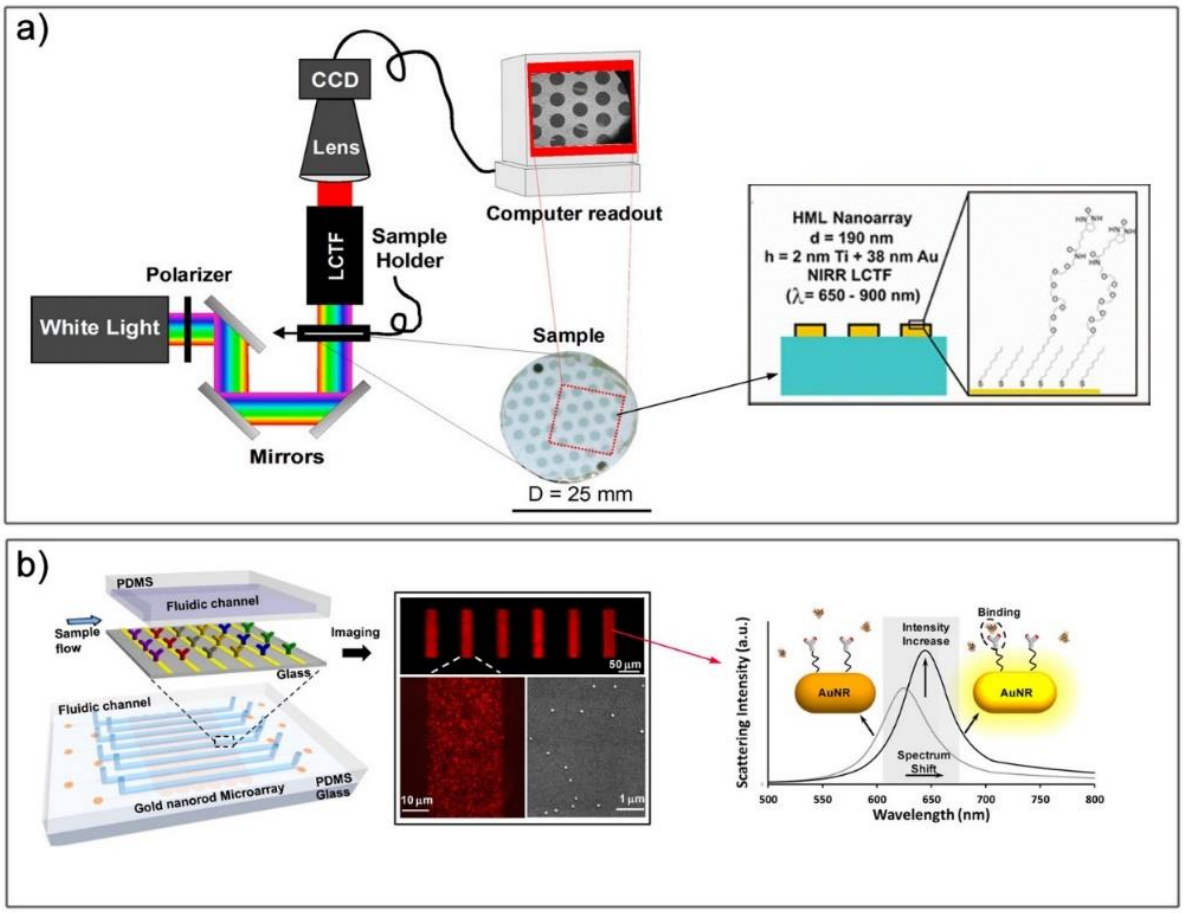

Figure 1.4. Schematic of the multiplexed assay based on shifts of LSPR. (a) An LSPR instrument setup with the sample containing microarrays of gold nanodiscs, and (b) microfluidic chip comprising a microarray of gold nanorods for different targets. Reprinted with permission from ref 22 and ref 23. Copyright 2013 and 2015 American Chemical Society.

1.2 Plasmon Coupling and Hybridization Theory

When two or more plasmonic nanoparticles are close to one another, their LSPRs couple with each other to generate hybridized plasmons. The magnitude of the LSPR shift or the strength of plasmon coupling strongly depends on the interparticle distance, particle geometry, and the LSPR of individual particles. Modelling methods are often used to understand the optical properties between nanostructures. Mie theory, as discussed in Section 1.1 is an example of an early technique for modelling plasmonic structures, but its application is limited to a single

spherical structure. Recent modelling advances using numerical simulation methods, notably Finite-Difference Time-Domain (FDTD), are useful for investigating arbitrarily complex geometries. The FDTD simulation method works on the principle of discretizing all objects into very small elements of a geometry for which Maxwell's equations are solved (see Appendix A1 for more details). By inputting the geometry and material of the nanostructure, the plasmon energies or optical spectra can be generated without the need to empirically solve the underlying fundamental physics. In addition to the modelling methods, the plasmon hybridization theory has been developed to provide a framework for understanding coupled plasmons in complex nanostructures. It offers a principle that can be applied to guide the design of nanostructures and predict their resonant properties.

Plasmon hybridization theory is a relatively new concept developed by Prodan and Nordlander.[24] They formalized the conduction electron as an incompressible fluid model, where an irrotational liquid of negatively charged electrons sits on metal's positively charged rigid ion core. The kinetic and potential energy of the interaction between incompressible fluid conductive electrons and rigid metal core based on the Lagrangian model[24,25] is then used to find plasmon resonance of nanoparticles. The simple formalism can be applied to investigating the plasmonic interaction of a single nanostructure (i.e., nanoshells, concentric nanoshells) and complex nanostructures including dimers, trimers, heptamers, and core-satellite assemblies. The interaction of plasmon resonance in complex structures can be viewed as analogous to the molecular orbitals theory, where the electron orbitals of individual atoms hybridize to form molecular orbitals.[26,27] In this section, we will discuss complex nanostructures, including dimers, core-satellite assemblies and nanoshells, and describe the optical properties of nanostructures using plasmon hybridization theory.

1.2.1 Nanoparticle Dimer

The plasmonic nanoparticle dimer is the simplest model of the multiparticle structure to illustrate the optical properties arising from plasmon hybridization. When two plasmonic nanoparticles come into proximity with each other, the near-field of one particle can interact with the other particle, giving rise to new plasmon oscillation modes: low-energy "bonding" and high-energy "antibonding" modes, as illustrated in Figure 1.5. The magnitude and direction of the spectral shift depend on the orientation of the nanoparticle pair with respect to the polarization axis of the incident light.[28–30] These two modes differ in their dipole moment and coupling to incident light: for longitudinal polarization, the high-energy mode has no net dipole moment because the dipoles on each nanoparticle are anti-aligned, thus light is neither absorbed nor emitted/scattered. The modes with no dipole moment are considered optically forbidden, known as a "dark" mode. However, they still have attracted much interest because the vanishing dipole moment of the dark modes with low radiation loss and damping leads to a stronger near-field enhancement than the bright mode.[31] Hence, the dark modes are explored for hot electron generation[32] and surface-enhanced Raman spectroscopy (SERS).[33] However, the challenge of how to excite dark modes limits its use. Because of the absence of a net dipole moment in homodimers, dark modes cannot be excited by plane electromagnetic waves; they can only be excited using near-field excitation or fast electrons, as in electron energy loss spectroscopy[34] or cylindrical vector beams.[31] In contrast, the lower-energy mode has mutually aligned longitudinal dipoles, producing a mode with a large induced dipole and a strong coupling to the far-field, referred to as the "bright" mode. The lower-energy mode with enhanced optical properties can be easily excited by electromagnetic waves, making it useful for sensing applications.

The strength of plasmon coupling depends on the distance between the particles and the direction of polarization. In particular, the extinction spectrum of a dimer nanostructure can exhibit either a redshift or blueshift relative to the LSPR of an individual particle depending on the direction of the incident electric field. For example, when the incident light field is polarized along the interparticle axis or longitudinal polarization, the LSPR peak exhibits a redshift to a longer wavelength. The magnitude of the redshift is determined by interparticle distance and follows the interaction energy between two dipoles ($\Delta\lambda_{redshift} \approx distance^{-3}$).[35] The distance-dependent concept was explained by the dipole-dipole coupling model,[29] which suggests that the gap distance can influence the repulsive forces for the surface charges. For example, a decrease of gap distance results in the increase of attractive force between the charges on the two particles (Fig. 1.5c). The repulsive forces within each particle, therefore, are weakened, leading to a correspondingly lower resonance frequency. In contrast, when the electric field is perpendicular to the interparticle axis or transverse polarization, the observed LSPR is a blueshift with respect to the individual particle due to the excitation of the high-energy mode (Fig. 1.5b). The blueshift increases with decreasing gap distance as the dipole-dipole coupling model suggests enhanced repulsive forces in both particles (Fig. 1.5d).

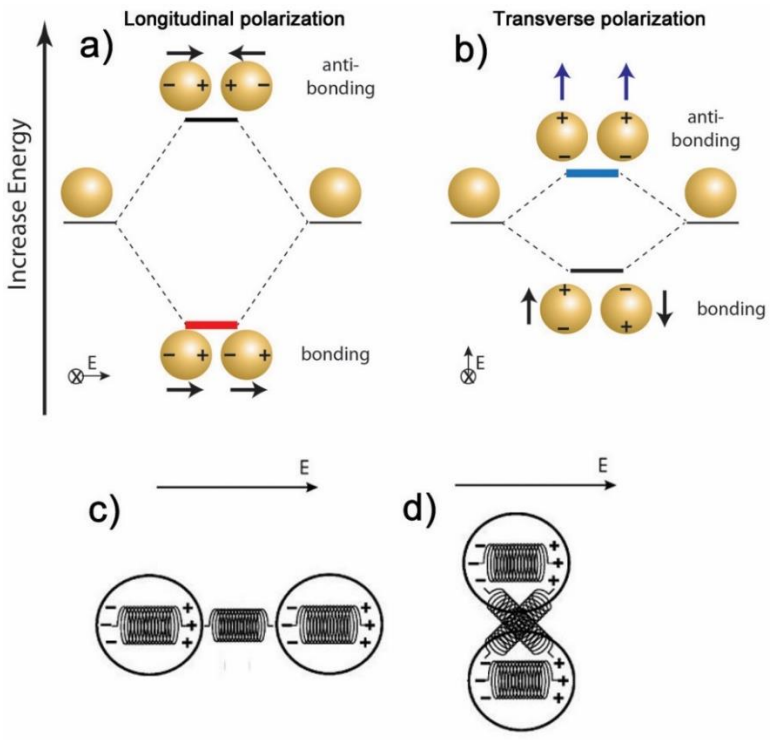

Figure 1.5. Plasmon hybridization model of a homodimer, depicting bonding and antibonding combinations of dipole moments. (a) The longitudinal modes are excited by the electric field (E) that is parallel to the interparticle axis, whereas the light field is orthogonal to the interparticle axis resulting in the excitation of transverse modes (b). The electromagnetic interaction between closely spaced nanoparticles. (c) a pair of close particles with the longitudinal polarization and (d) a pair of close particles with transverse polarization. The arrows in the scheme indicate the dipole moments of the individual particles. (c-d) Reproduced with permission from ref 29. Copyright 2003 Elsevier Science.

Besides homodimers, heterodimers such as AgNP/AuNP[30], AuNP/Au shell[36], or asymmetric nanoshell dimers[37] have been studied. The plasmon hybridization theory can also be used to explain the optical properties of these nanostructures. When the unidentical NPs are paired, the plasmon modes of the constituent nanoparticles hybridize, forming the bonding and anti-bonding heterodimer modes. However, due to symmetry breaking, both the bonding and anti-bonding modes are observed in the optical spectrum. The anti-bonding mode, otherwise dark in the homodimer, is significantly weaker in intensity compared to the bonding mode in the heterodimer.[7] For example, a heterodimer of Ag-Au exhibits two distinct peaks resulting from the

excitation of both bonding and anti-bonding modes (Fig. 1.6a). The redshift of the bonding modes with respect to the gold particle plasmon resonance is predicted by the plasmon hybridization theory. However, there exist interactions of higher-order modes and the dipole-multipoles between the particles, e.g. dipole – quadrupole or dipole – octupole that could lead to unexpected hybridized modes.[36] For example, in a heterodimer of Ag/Au, it was observed that the antibonding modes are red-shifted with respect to the Ag plasmon resonance due to the coupling of the AgNP LSPR to the quasi-continuum of interband transitions in Au; this should be blue-shifted according to the hybridization theory (Fig. 1.6b). The magnitude of the shift in the energy of the bonding mode is smaller for the heterodimer than that for the homodimer because of the energy levels offset of the constituents (Fig. 1.6b). It should be noted that the bonding plasmon frequency (or sigma mode) depends not only on the interparticle distance but also on the plasmon frequency supported by individual particles. Hence, changing different materials can influence the plasmon coupling, leading to the shift of LSPR and tunable optical properties (see Chapter 4).

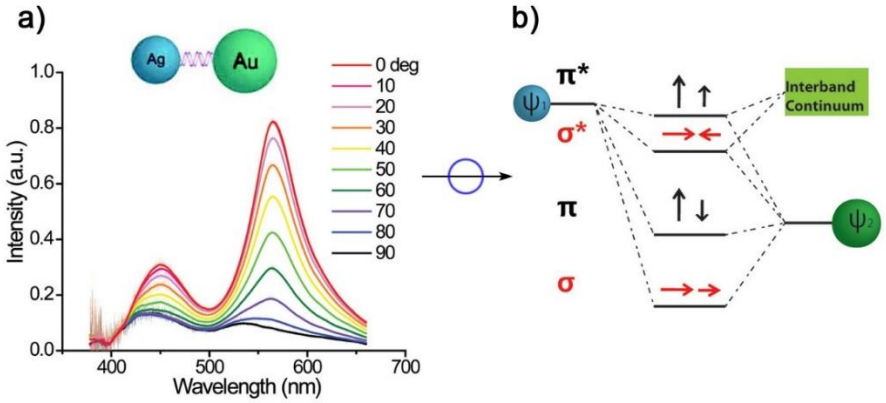

Figure 1.6. Plasmon coupling of a compositionally asymmetric dimer composed of a 30-nm silver and a 40-nm gold nanoparticle. (a) Scattering spectra of the asymmetric dimer as a function of the polarizer angle (0-90°) which is elucidated by (b) the hybridization model with σ and σ* representing the bonding and antibonding modes, respectively in longitudinal polarization, and with π and π* represents the bonding and antibonding modes, respectively in transverse polarization. Reprinted with permission from ref 30. Copyright 2010 American Chemical Society.

1.2.2 Core–Satellite Nanoparticle Assemblies

Plasmonic nanoparticle assemblies comprising a core NP with multiple surrounding satellite NPs is another example of coupled nanostructures that exhibit enhanced light scattering intensity and large LSPR spectral shifts. The electric field enhancement is more significant than dimers or trimers due to more orbit satellites. Hence, the core-satellite nanostructures have been explored for SERS[38] and LSPR-based sensors.[39,40] The optical properties can be described by the plasmon hybridization model,[26,41,42] which suggests that the plasmon coupling between the core and the orbit of satellites leads to the shift of LSPR to a low-energy mode and a high-energy mode with respect to the primitive plasmons of the building blocks. Figure 1.7a shows the dipole-dipole interaction of a single core and multiple satellites as a degenerate ensemble of individual dipoles. The spectral shift results from a low-energy mode, which is referred to in the literature as radiant or longitudinal modes.[41] This mode can be excited by an external field aligned along the longitudinal axis of the nanostructure with a redshift to a longer wavelength similar to the longitudinal coupling in homodimer or heterodimer. The simulated surface charge study using modelling found that the radiant mode exhibits the most enhanced polarization from the surface charge interaction between the core and satellites (Fig. 1.7c), wherein the satellites exhibit dipole moments aligned toward the core charges, yielding an energetically favorable overall charge distribution and enhanced far-field scattering. As a result, the LSPR shifts to longer wavelengths with significantly enhanced scattering intensity.[41,42] Conversely, a high-energy mode exhibits a blueshift with respect to the LSPR of the building blocks. Because of the weak polarization in the overall charge distribution, the high-energy mode, which is referred to as nonradiant, usually appears much less prominent than the lower-energy radiant mode; the simulated surface charge study suggested a dominant satellite-to-satellite coupling in the high-energy nonradiant mode (Fig.

1.7b). In the LSPR of core-satellite assemblies, the appearance of a shoulder on the left side of the LSPR spectrum likely reflects the excitation of nonradiant modes. The magnitude of the nonradiant mode depends on the strength of satellite-to-satellite coupling. Hence the shoulder of the spectra appears less pronounced for the smaller satellite NPs and more pronounced for the bigger satellite NPs.

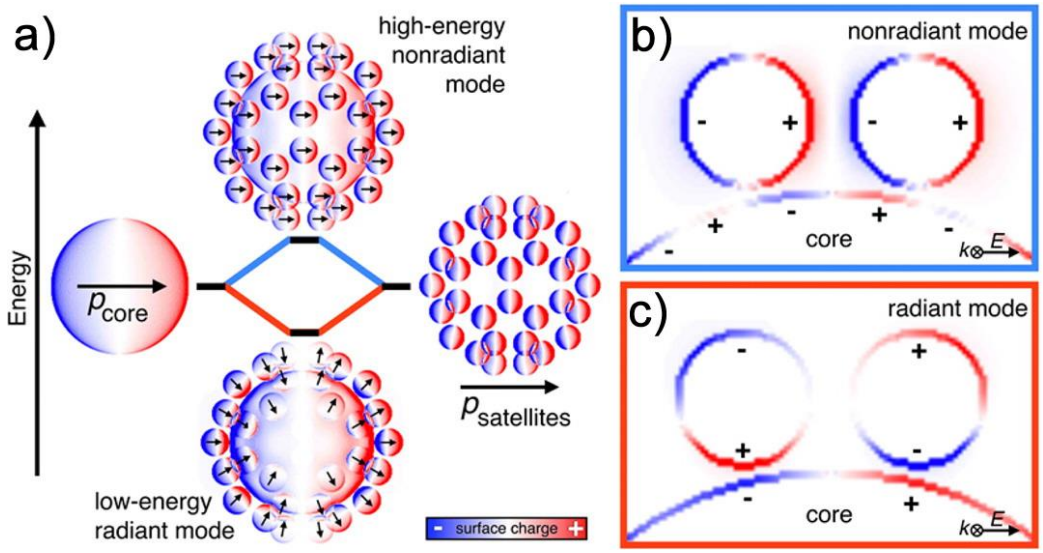

Figure 1.7. Plasmon hybridization model of the core-satellite nanostructure, depicting the radiant mode and the nonradiant mode using polarization states. (a) Main excitation states are shown by surface charge densities with black arrows representing the orientation of the local dipole moments. (b) The high-energy nonradiant mode with strong coupling between neighboring satellite particles demonstrates surface charges at the cross-section of coupling satellites. (c) Surface charges in low-energy radiant mode show the dominant core-to-satellite coupling. Reprint with permission from ref 41. Copyright 2016 American Chemical Society.

In core-satellite nanostructures, the strength of plasmon coupling (and the shift of LSPR induced by it) depends on the interparticle distance, the number and size of NPs, and the plasmon energy of the individual constituents. The plasmonic coupling of NP assemblies is distance-dependent between core and satellite NPs similar to dimer structures; when the distances between

core and satellite NPs reduce, the plasmon coupling is stronger, leading to a spectral shift to longer wavelengths. Yoon *et al.* demonstrated the plasmon coupling as a function of the gap distance between core and satellite NPs (Fig. 1.8a).[43] Furthermore, the plasmon coupling also depends on the number of nanoparticles that constitute the complex nanostructures. In another study, Yoon *et al.* showed that the LSPR peak continuously redshifts as more satellite nanoparticles attach to a core (Figure 1.8b). The shift of plasmon coupling is almost linear with an increasing number of satellites.[44] This linear relation has been observed in various combinations such as Au core−Au satellite[41,44,45] and Ag core–Au satellite[46] assemblies. In general, the addition of the satellites to the assembly causes more plasmon modes to be mixed in the hybridized plasmons, leading to the continuing redshift of the LSPR band. Finally, plasmon hybridization also depends on the LSPR of the individual building block. Since LSPR is extremely sensitive to the dielectric constants of materials, different materials and/or morphologies yield LSPR at different wavelengths. Thus, the energy of plasmon coupling of the NP assemblies can be determined by their components. In literature, Au and Ag are the most common building blocks for the core-satellite nanostructure, and the optical properties of the complex nanostructures have been studied experimentally and theoretically.[47] To understand the effect of materials on plasmon coupling, Figure 1.8c compares the extinction spectra of the core-satellite assemblies with different materials. The data show the differences in the shift of energy of the coupled plasmon modes when the NP assemblies are made of the same NP size and the gap distance but different compositions. Since the LSPR of the AuNP is much lower in energy than AgNP, the nanostructures comprising of AuNPs exhibit the bonding modes that resonate at a longer wavelength than that for the AgNP assemblies. Overall, the plasmon coupling of the complex nanostructures depends not only on interparticle distance but also on the size of clusters and the building blocks.

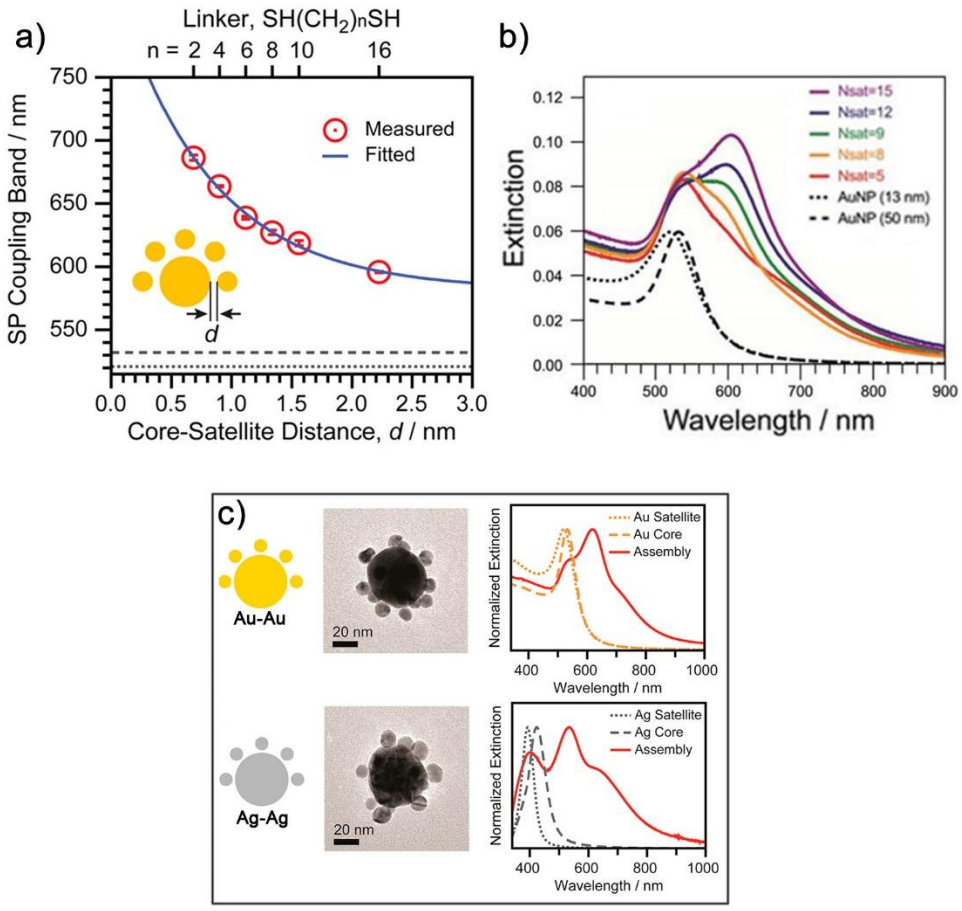

Figure 1.8. The effect of plasmon coupling in the core-satellite nanostructure. a) distance-dependent showed by a plot of the peak positions of the surface plasmon coupling bands of the nanoparticle assemblies as a function of the gap distance (dot-circles) and its best fit to an exponential function (solid line). b) The effect of the assembly size monitored by UV-vis spectra of core-satellite AuNP assemblies with a varying number of satellite AuNPs. c) The effect of building blocks as demonstrated by comparing the extinction spectra of nanostructures assembled by Au – Au vs Ag – Ag. The diameter of the core and the satellite NPs are 50 nm and 13 nm, respectively. Reprint with permissions from ref 43, ref 44, and ref 47. Copyright 2012 and 2013 American Chemical Society, and Korean Chemical Society.

1.2.3 Metal Nanoshells

Another plasmonic nanostructure that illustrates the concept of plasmon hybridization is metal nanoshells. Metal nanoshells consisting of a dielectric core (i.e. SiO_2) coated with a thin metal shell (i.e. Au or Ag) were firstly synthesized by Halas and coworkers.[48] Metal nanoshells

are widely used in sensing applications because their LSPR can be tuned to wavelengths in the visible and infrared regions by controlling the relative core and shell dimensions.[48,49] The optical properties of nanoshells can be described by plasmon hybridization between two plasmons supported by a nanoscale sphere and cavity.[50] The sphere and cavity plasmons hybridize and form two new modes: a lower energy symmetric or "bonding" plasmon and a higher energy antisymmetric or "antibonding" plasmon (Fig. 1.9a). The antibonding plasmon (denoted as ω_+), in which the dipole moments of the sphere and cavity are anti-aligned, is blueshifted to higher energy whereas the bonding plasmon (denoted as ω_-), in which the dipole moments are aligned, is strongly redshifted to lower energy (Fig. 1.9a). The charge configuration of the antisymmetric mode causes the sphere and cavity dipole moments to oppose each other and subtract, resulting in a small total dipole moment for the nanoshell. This means that the high-energy mode cannot couple efficiently to light and is sometimes referred to as a "dark" mode. The symmetric mode, however, has a very large total dipole moment because the sphere and cavity dipole moments add together. Thus, the lower-energy mode can couple to light very efficiently. The energy of the plasmon coupling depends on how strongly the primitive sphere and cavity plasmons interact; in other words, the strength of this interaction can be controlled by the thickness of the shell layer as shown in Figure 1.9b. When the shell is made thinner, the inner and outer surface of the nanoshell can interact more strongly, which redshifts the bonding plasmon mode further. By changing the ratio of the core radius to the shell thickness, the LSPR of nanoshells can be tuned to any frequency throughout the visible and infrared.[50] Because of this tunability, nanoshells present another interesting morphology for deriving coupled nanostructures, although this area is less explored than those of solid nanoparticles.

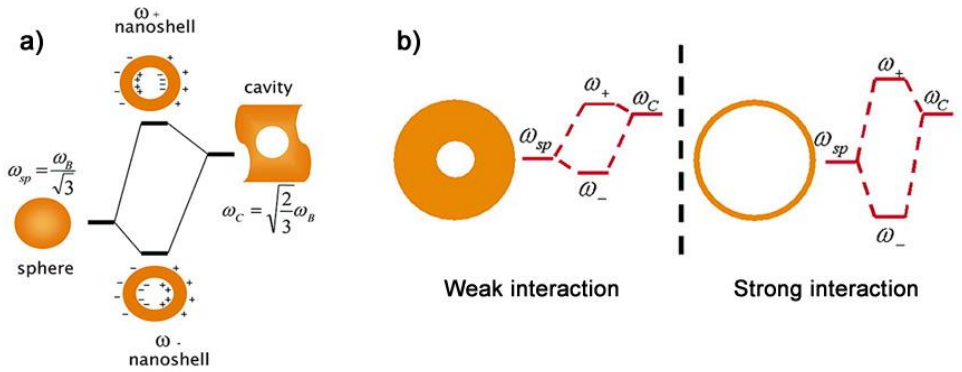

Figure 1.9. Schematic of plasmon hybridization theory applied to the nanoshell dipolar mode. Energy level diagrams (a) depicting plasmon hybridization in metal nanoshells resulting from the interacting sphere and cavity plasmons with the two hybridized plasmon modes being an anti-symmetric plasmon (ω_+) and a symmetric plasmon resonance (ω_-), and (b) illustrating the dependence of nanoshell plasmon energies on the strength of the interaction between the sphere and cavity plasmons, determined by the thickness of the metallic shell. Reprinted with permission from ref 50. Copyright 2007 American Chemical Society.

1.3 Biosensing Based on Plasmon Coupling

Since LSPR spectral shift depends on the distance between the interacting particles, plasmon coupling has been explored for sensing applications from bulk colloids to discrete individual NPs. Particularly, the distance-dependent concept offers an optical response for detecting various biomolecules, including proteins, nucleic acids, antibodies and small molecules. This sensing platform offers rapid detection that can be achieved by the color change, which can be detected visually or measured spectroscopically. This section introduces the sensing applications based on the colorimetric response that have exploited the distance-dependent concept of the coupled nanostructures.

1.3.1 Colloidal Colorimetric Sensing

Plasmon coupling can be used for colorimetric detection of analytes in bulk solution via the colloidal aggregation of DNA-functionalized gold nanoparticles.[51] In the presence of the target

nucleic acid, AuNPs are cross-linked and brought into close proximity, leading to a color change from red to purple that can be visually detected (Fig. 1.10a). This approach can also be used for different targets by engineering DNA cross-linkers. For example, Liu and Lu incorporated DNA aptamers as cross-linkers and demonstrated the colorimetric sensing of adenosine and cocaine.[52] Beside the aggregation through cross-linked DNA, the sensing can also be achieved through the disassembly process. Here, the aggregate is disassembled in the presence of adenosine, yielding the color change from purple to red and a blueshift in the UV-vis spectrum (Fig. 1.10b). Colloidal-based colorimetric sensing has desirable properties, including rapid, easy performance and high selectivity; however, it suffers from stability issues,[53] where coagulation and false positives may arise due to environmental factors such as a change in the ionic strength, pH, and temperature. To avoid unexpected colloidal coagulation, the nanoparticles can be anchored on a substrate and used as chip-based nanosensors.

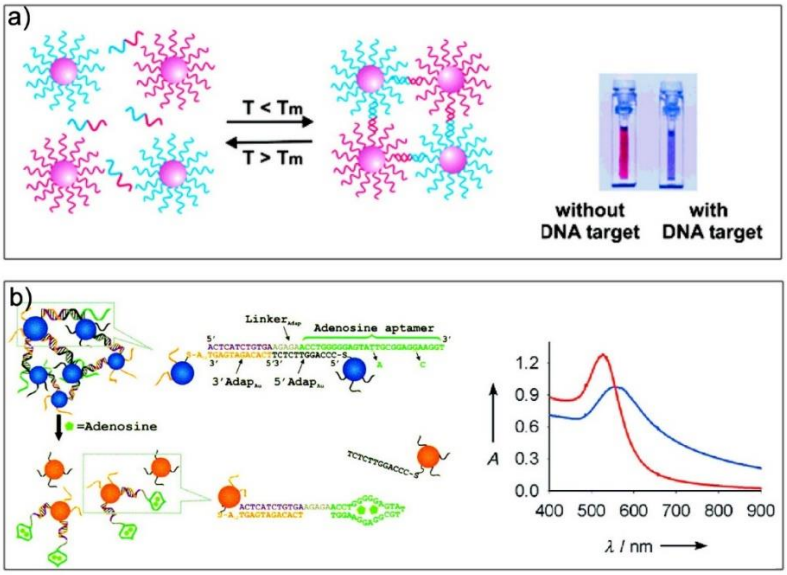

Figure 1.10. Colorimetric sensing based on colloidal NP solution in bulk. (a) Detection of complementary target DNA via aggregation based on the change of solution color from red to blue. (b) Detection of adenosine achieved by blueshift of LSPR via disassembly. Reprinted with permission from ref 51 and ref 52. Copyright 1997 American Association for the Advancement of Science and 2006 Wiley-VCH.

1.3.2 Single-Nanostructure Sensing

Sensing based on discrete individual nanostructures is an alternative approach to using bulk solutions or films. By reducing the number of probe particles,[16,54] researchers have demonstrated enhanced sensitivity and low detection limit down to attomolar[55] and even single molecule level[56] using single nanostructures. Single NPs on a substrate can serve as chip-based sensors that are invaluable for studying biomolecular interactions. Individual NPs can be readily imaged and measured using darkfield (DF) microscopy due to their high scattering cross-sections (~ 4-5 orders magnitude greater than emission cross-section of organic fluorophores).[57] A typical DF microscope consists of a dark-field condenser, white light illumination, and a color charge-coupled device (CCD) camera or a spectrometer. The scattered light from plasmonic NPs can be collected by a digital camera as a DF image or measured spectroscopically using single-nanostructure optical setups (see Appendix A2 for details). It is important to note that DF microscopy enables the monitoring of hundreds to thousands of plasmonic NPs simultaneously, hence DF imaging may offer multiplexing capability that is desirable for point-of-care diagnostics.[1,58] In addition to the development of image-based analysis, the colors of single nanoparticles can be converted to spectral wavelengths that offer a simple and rapid method for throughput acquisition and automatic analysis (see Appendix A3).

1.3.2.1 Dimer Nanostructure as Plasmon Ruler

In a dimer nanostructure, the pair of NPs can be used to measure the molecular length of a linking molecule based on the distance between the two NPs; this concept is known as the plasmon ruler. This concept is similar to the Förster resonance energy transfer (FRET) phenomenon from a pair of fluorescent dyes.[59] FRET is based on the energy transfer from the excited donor to the acceptor dyes and the energy transfer efficiency depends highly on the relative distance between

the pair. While FRET has become a valuable tool in probing distances and dynamic changes in biomolecules, there is increasing interest in using metal NP plasmonic rulers because of their stronger optical signals and absence of photobleaching. In addition, a pair of plasmonic NPs can probe a longer distance compared to dye-pair FRET. For example, the distance of energy transfer between two fluorophore dyes is limited to <10 nm.[60] Because of the strong field coupling, the distance detectable between NPs in a dimer can be up to 70 nm for a 40-nm gold NP dimer; the range can be extended by increasing the size of particles.

The first application of plasmon ruler and sensing based on individual dimers was conducted by Alivisatos and co-workers to detect a nucleic-acid binding event.[61] A gold NP dimer linked by ssDNA was fabricated on a substrate and monitored by light scattering using spectroscopy. The binding event was demonstrated by the distance-dependent plasmon coupling phenomenon, in which a single nucleic-acid binding event led to the formation of dsDNA linkers and geometric extension of the dimer; the hybridized plasmon shifts spectrally. The distance change-induced plasmon shift can be used to monitor DNA hybridization and measure nanoscale distances (Fig. 1.11).

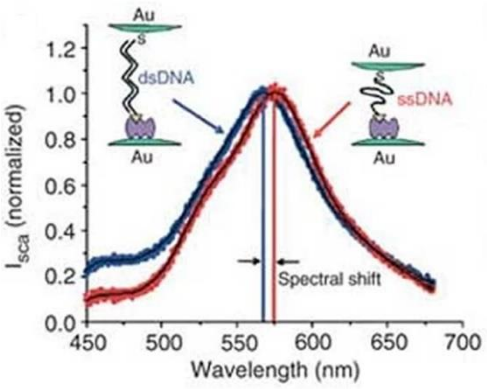

Figure 1.11. Plasmon ruler of gold dimer nanostructure based on spectral shift upon DNA hybridization and spectral shift between a gold particle dimer connected with ssDNA (red) and dsDNA (blue). Reprinted with permission from ref 61. Copyright 2005 Nature Publishing Group.

The LSPR spectral shift is a function of the interparticle gap and the particle size. El-Sayed and co-worker[28] studied the distance dependence of plasmon coupling systematically with gold nanodisc and proposed the plasmon ruler equation

$$\Delta\lambda/\lambda_0 \approx 0.18\, exp(\frac{-s}{0.23D})$$

Where $\Delta\lambda/\lambda_0$ is the fractional plasmon shift, and s is the interparticle gap scaled by the particle diameter D. The equation is validated based on a comparison with the experiments of Alivisatos and his coworkers on gold nanoparticle plasmon rulers assembled by DNA linkers of different lengths.[62] The universal scaling model has become a quantitative guide for the design of plasmon rulers.

Plasmon ruler is an active area of research, and it is expected that different plasmonic nanostructures can be developed exhibiting even greater sensitivity and selectivity. Recently, a three-dimensional plasmon ruler has been developed, which shows a remarkable sensitivity to the interparticle distance and the spatial arrangement of the nanoparticles.[63] This type of plasmon ruler opens a new generation of plasmonic biosensors that are extremely sensitive to changes in their surrounding environment.

1.3.2.2 Core-Satellite Nanostructure

The core-satellite nanostructure is preferable to a dimer structure because of the higher scattering intensity and larger spectral shift due to the plasmon coupling from a higher number of orbit satellite NPs. AuNPs are commonly used for assemblies because of their high stability. The sensing can be achieved through aggregation or disassembly of the nanostructure. Waldeisen *et al.* determined a figure of merit (FOM) to optimize the diameter of core and satellite NPs for

colorimetric detection with 30 – 50 nm.[64] The core-satellite nanostructures were applied for monitoring the activities of protein[64,65] and detecting biomarkers[66,67] and nucleic acids.[68,69] The first application of the substrate-based plasmon-ruler concept with core-satellite assemblies was implemented by Alivisatos and co-workers, where they monitored the trajectories of single biomolecules in live cells and in-vivo.[65] In their work, the core-satellite assemblies comprising a single layer of peptide-linked 40-nm satellite AuNP around a 40-nm core AuNP were used to monitor early-stage caspase-3 activity for the apoptosis process in live cells (Fig. 1.12a). In the presence of caspase-3, the peptide linkers were cleaved and the satellite AuNPs were detached from the core AuNP, leading to a decrease in the plasmon coupling and a significant blue shift and lower intensity in the LSPR. Under darkfield microscopy, the scattered light changed from yellow/orange to green. In a similar idea, Lee and coworkers engineered a different peptide linker to fabricate the NP assemblies and disassembled the nanostructure to detect protease trypsin (Fig. 1.12b).[64] In these early works, the detection relies on the cleavage of linker for the disassembly process. This leads to one of our motivations to develop linkers for a broader range of targets that do not undergo enzymatic cleavage mechanisms. The chip-based sensor comprising individual

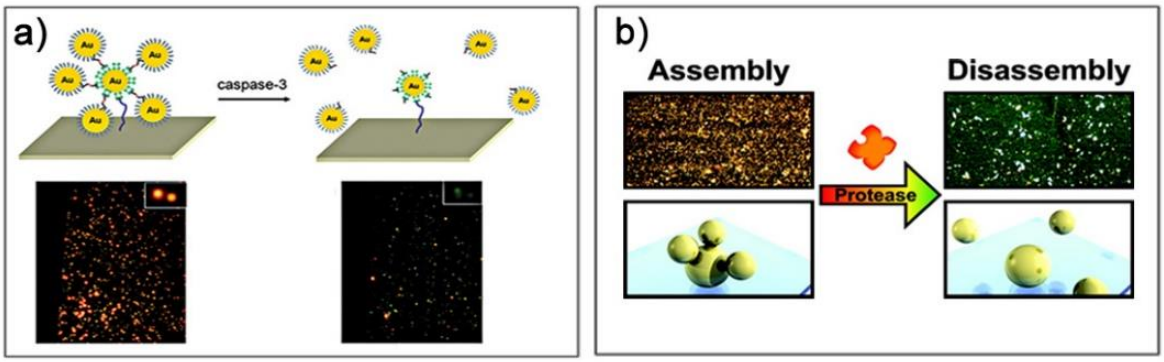

Figure 1.12. Colorimetric sensing based on individual plasmonic nanostructures. Gold nanoparticle assemblies anchored on a substrate for detecting (a) caspase-3 and (b) trypsin protease enzyme via a color change from red to green upon disassembly. Reprinted with permission from ref 64 and ref 65. Copyright 2011 American Chemical Society and 2009 National Academy of Science.

plasmonic nanostructure is at the beginning stage of the development and it is expected that this platform can be integrated into microfluidics or portable nanodevices for biomedical applications.

1.4 DNA Aptamer

One of the important components of reconfigurable dimers or assemblies is the biomolecular linker. The linker is important not only for the fabrication process but also for controlling the optical properties of the nanostructure. For example, the optical properties can be tuned by changing the length of the linkers.[70] The linker can also act as the molecular recognition probe to detect the analyte. Taking advantage of high-affinity chemisorption of various functional groups, and especially the covalent bonding of thiol-gold (ca 200 kJ/mol),[71,72] noble metal NPs can conjugate with various biomolecules including nucleic acids,[73] peptides,[74] proteins,[65] and antibodies.[75] Antibodies are widely employed as the recognition elements because they can selectively bind to a broad range of analytes with high affinity. However, they suffer from disadvantages, including lack of variety, stability, and cost of production.[76] Nucleic acid aptamers, on the other hand, have attracted attention as alternative molecular recognition elements.

Aptamers are short single-stranded RNA or DNA molecules that can bind to targets such as proteins, peptides, small molecules, and even live cells with high specificity and affinity. The aptamers are selected through a process, named Systematic Evolution of Ligands by Exponential Enrichment (SELEX), which was developed in 1990 by Tuerk and Gold,[77] and Ellington and Szostak.[78] Although aptamers recognize and bind targets similar to antibodies, they have advantages such as good thermal stability, ease of modification, facile chemical synthesis with a short production time, and high binding affinity to a broad range of targets. As a result, aptamers are explored for therapeutic applications[79] and biosensing.[80] The well-characterized DNA aptamer for ATP or adenosine is widely used as a model for the development of biosensors and analytical

methodologies. This section introduces the properties of ATP-aptamer, including its binding affinity and binding model.

1.4.1 ATP Aptamer

The 27-nucleotide DNA aptamer for adenosine is one of the most studied since its report in 1995 by Huizenga and Szostak.[81] It has similar affinities and binds with high specificity to adenosine derivatives, including adenosine monophosphate (AMP), adenosine diphosphate (ADP), and adenosine triphosphate (ATP). It was initially believed that a G-quadruplex structure was formed in this aptamer.[81] A subsequent NMR study by Chin *et al.* showed a hairpin-duplex structure containing two recognition pockets – the first comprising G6, G22, and A23, and the second G9, A10, and G19 (Fig. 1.13a).[82] The tertiary structure of the aptamer folds into a double-stranded-like helical structure in which two AMP molecules are inserted at adjacent sites within a rectangular widened minor groove (Fig. 1.13b). Each pocket can accommodate one molecule through hydrogen bonding interaction of the GA mismatch and π-stacking of the adenine base with a reversed Hoogsteen GG mismatch.

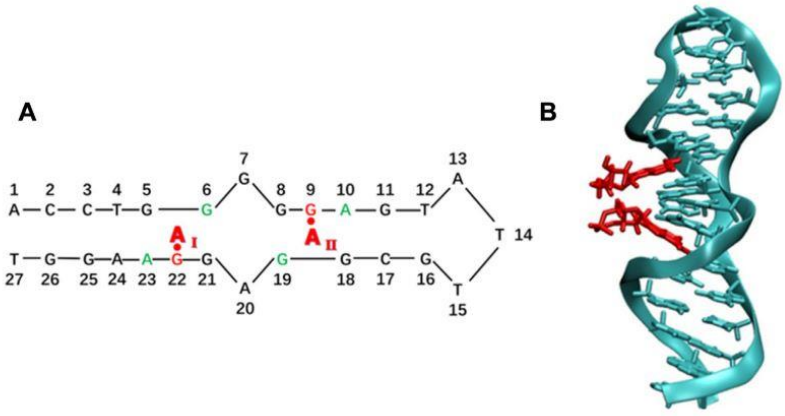

Figure 1.13. (a) The nucleic acid sequence of the aptamer-AMP complex. The binding sites of the two bound AMP molecules (A_I and A_{II}) are highlighted in red and green. (b) The proposed tertiary structure of the AMP_2–aptamer complex. Reprinted with permission from ref 82. Copyright 1997 Published by Elsevier Ltd.

The specific and cooperative binding of adenosine derivative to aptamer was demonstrated using isothermal titration calorimetry in recent reports.[83–85] The Johnson group reported the positive cooperative binding for two binding sites with a slightly different affinity for adenosine derivatives.[85] They suggested that cooperativity arises from a population-shift binding mechanism where the two binding sites are linked, and the initial binding event affects the structure or dynamics of the binding sites and the region in between. The second ligand, therefore, binds tighter than it otherwise would. Additionally, as the number of phosphate groups on the adenosine-containing ligands is reduced, the affinity at both binding sites becomes stronger. This can be understood by considering the structure of the aptamer–ligand complex in which the two binding sites are adjacent on the same side of the helical structure. When the adenine stacks into the aptamer's binding site, the phosphate groups, which do not directly participate in binding, are oriented outward and exhibit electrostatic repulsion with the negatively charged DNA. Therefore, adenine nucleotides with fewer phosphate groups would bind more tightly.

1.4.2 ATP-Aptamer Binding Mechanism

The binding-related structural changes of aptamers are proposed to occur via induced-fit and/or conformational selection (Fig. 1.14). The induced-fit model assumes ligands catalytically interact with the non-bound state and directly induces its fit, leading to the formation of a final ligand-bound structure. In contrast, conformational selection describes the binding of ligand on the preexisting bound conformation.[86]

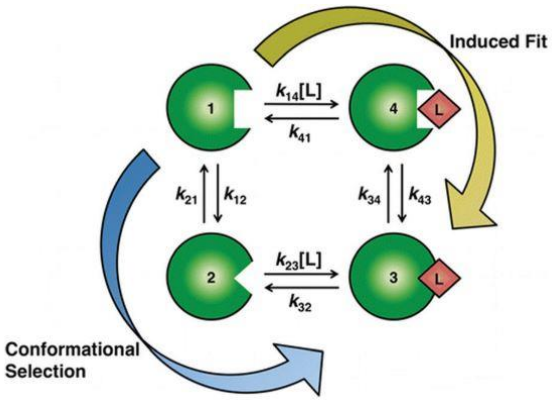

Figure 1.14. Ligand-bound systems through conformational selection and induced-fit pathways. An overview of a thermodynamic cycle for a model protein (in green) binding a ligand (L, in red) is shown, outlining two different pathways. Binding states of non-competent (1), binding competent (2), ligand-bound (3), and induced-fit intermediate (4) are labeled. Reprinted with permission from ref 86. Copyright 2019 Royal Society of Chemistry.

The mechanism of structural changes for the ATP-aptamer binding target has been a subject of debate. The conformational selection for ATP binding-aptamer has been suggested in a recent report.[87,88] Xia *et al.* discovered the dependence of folded duplex-like and unfolded conformations on ionic concentrations using FRET spectroscopy.[87] A single FRET probe shows an existing equilibrium between folded and unfolded conformation at a lower salt concentration (45 mM NaCl) – the aptamer prefers unfolded structures and occasionally changes to the folded conformation for a short time before being unfolded again. Subsequently, the binding of ATP can shift the equilibrium to the folded duplex structure by forming a tertiary structure. This result highly suggests a conformational selection mechanism; however, it could be argued that there is the possibility that ATP binds to the unfolded structure and then shifts the equilibrium to ligand-bound state at a low salt concentration which mimics the induced-fit mechanism.

1.4.3 Aptamer-Based Biosensor or Aptasensors

The use of aptamers in sensing often incorporates a duplex design, in which the aptamer is hybridized with a partial complementary sequence, known as the aptamer-complementary element (ACE) (Fig. 1.15). The ACE competes with the ligand for binding to the aptamer, hence the dehybridization of the ACE–aptamer duplex leads to a detectable signal. This duplexed aptamer motif can be integrated with a wide range of readout methods, including FRET,[89,90] fluorescence,[52] and electrochemistry.[91]

In aptamer-based sensors (aptasensors), the mechanism of target binding again can be either conformational selection or induced-fit, but with some differences because of the initial duplexed aptamer structure. The mechanistic frameworks of the conformational selection and induced-fit pathways mirror the first-order (S_N1) and second-order (S_N2) nucleophilic substitution reaction mechanisms, respectively. In the conformational selection, ACE needs to firstly dehybridize from the duplexed aptamer to yield the free aptamer, followed by the binding of the natively folded aptamer with the ligand (pathway including states 1, 2 and 3 in Fig. 1.15). It is important to note that the dehybridization of the ACE and the aptamer–ligand binding are independent events, implying that the ACE dehybridizes without influence by the ligand. For aptasensors operating with a conformational selection binding mechanism, the kinetics and affinities of the system are governed by the hybridization kinetics of the ACE, which is the limiting step in the pathway. In particular, the more stable the hybridization of ACE and aptamer, the slower the sensor response and the lower the affinity. For example, Porchetta *et al.* developed cocaine-based duplexed aptamers through conformational selection, in which ACE acts as allosteric inhibitors to sequester DNA aptamer into a bound state.[92] By modifying the length of ACE, they can tune the affinity over three orders of magnitude. In practice, the most straightforward parameter to tune is the equilibrium constants, K_{Hyb}, based on the ACE length and G-C content.

Most duplexed aptamers implemented in the literature use ACEs that fall in the range of 9 to 15 nucleotides; oligonucleotides longer than 15 bases favor the hybridized state over the dehybridized state, thus creating a bottleneck in the ligand binding pathway. In contrast, the induced-fit mechanism assumes the target first binds to the duplexed aptamer to form a ternary duplexed ACE-aptamer-target. This initial binding disrupts the duplex, yielding a final aptamer-target complex (this pathway includes states 1, 1' and 3 in Fig. 1.15). Thus, the induced-fit models the ligand as a catalyst that is sensed by the duplexed aptamers; the binding of the ligand promotes the dehybridization of the ACE from the aptamer, leading to a ligand-dependent signal. For aptasensors operating with the induced-fit binding mechanism, the kinetics and affinities of the system depend on ACE position and length, and it has been found that the sensor kinetics vary for different aptamers and different ACEs.

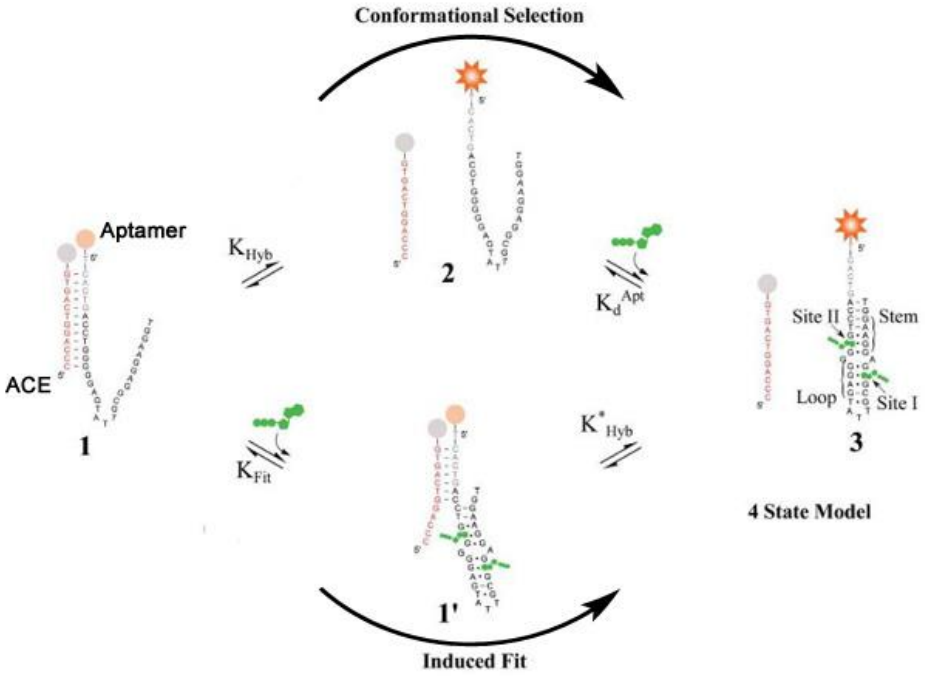

Figure 1.15. Overview of conformational selection and induced-fit models of duplexed aptamer ligand binding. The binding mechanism undergoes either conformational selection (state 1-2-3) or induced-fit (state 1-1'-3) pathways. Reprinted with permission from ref 93. Copyright 2017 Royal Society of Chemistry.

ACE is a key factor affecting not only the affinity and kinetics, but also the binding mechanism. By changing the location of ACE on the aptamer, Juncker and co-worker[93] observed either conformational selection or induced-fit ligand binding using solution-based fluorescent assays. They also discovered that ACE can promote the induced-fit mechanism depending on the degree of hybridization of the ACE to the ligand-binding pocket of the aptamer; generally, an induced-fit mechanism can be promoted by short 7- to 12-nucleotides hybridization bases pairs of ACE and aptamer.[94] The induced-fit ligand-binding mechanism was exploited for colorimetric sensing of adenosine using plasmonic nanoparticles.[52] Initial aggregates of the colloidal particles were constructed through the hybridization of the aptamers with ACEs functionalized on gold nanoparticles. The aptamer underwent a structural change upon adenosine binding, leading to the disruption of aptamer-ACE hybridization and the disassembly of aggregated NPs. In this sensing design, the binding event mimics the induced-fit mechanism, in which duplexed aptamer binds the target to form a ternary adenosine-aptamer-ACE and promotes duplexed dehybridization to yield adenosine-aptamer complex. This sensing platform was referred to as a structure-switching signaling aptamer.[95] The works carried out in this Ph.D. thesis utilized the structure-switching concept to develop chip-based sensing for ATP, down to the single-cell level, based on discrete coupled plasmonic assemblies.

1.5 Single cell analysis

Cells are highly heterogeneous, resulting from various genetic, epigenetic and environmental factors, as reflected by their differences in morphology, physiology and pathology.[96] Conventional cell-based assays mainly measure the average response from a population of cells, and thus the information regarding cellular individuality is often missing.

Single-cell analyses can provide the distribution of genomic, transcriptomic, proteomic and metabolomic levels in individual cells and enable the investigation of cell-to-cell variations. Advances in bioanalytical technologies have enabled the study of transcripts, proteins, and metabolites in single cells, thus facilitating the study of cellular heterogeneity. Although analyses of the transcriptome and the proteome offer genetic insights, the metabolome can provide information on biological processes, cell response and cell phenotype.[97]

The metabolome can be defined as small-molecule metabolites (with molecular weights of less than ~2 kD) found in cells or organs, such as amino acids, sugars, and lipids, which constitute precursors, intermediates and products in cellular processes. Single-cell metabolomics poses enormous challenges: (i) it has to deal with minimal quantities of analytes and limited sample volume that requires detection sensitivity in the femtomole or even in the attomole range.[98] (ii) rapid turnover rates of the cellular metabolome impacts quantification. Common technologies for single-cell metabolomics include fluorescence-based biosensors, electrochemical detection, and mass spectrometry.

Mass spectrometry (MS) is label-free, highly sensitive, and high throughput and thus is becoming one of the most widely used methods for detecting many metabolites at the single-cell level. The workflow during MS measurements includes several steps: the analytes are transferred into the gas phase, ionized, separated and analyzed by their mass-to-charge ratio and finally detected. The cellular metabolites can be extracted directly from single cells, then ionized and analyzed. Zhang *et al.* [99] presented a method of liquid extraction integrating droplet-based microextraction with electrospray ionization (ESI) mass spectrometry. A capillary's tip contacted single cells and extracted a microdroplet (about 2 nL) of the cellular compounds. The droplet was then extracted for selectivity and subsequently was evaporated and redissolved with solvent to

facilitate ionization and MS detection. With this method, adenosine triphosphate (ATP), adenosine diphosphate (ADP), AMP were detected and identified from single human breast cancer cells (MCF-7). Another approach for single-cell analysis is using nanospray desorption electrospray ionization. A continuously flowing liquid bridge was formed between two capillaries – one capillary supplies solvent to create and maintain the bridge while the second capillary transports the dissolved analyte from the bridge to the mass spectrometer. By placing the liquid bridge in contact with a single cell, the entire cell contents are desorbed into the liquid and analyzed by the mass spectrometer. Hence over 40 metabolites in human cells were identified.[100] Furthermore, capillary electrophoresis (CE) can combine with electrospray ionization (ESI) MS for single-cell metabolomics.[101] The CE separation step reduced the chemical complexity of the neuron samples prior to MS detection. Thereby, over 300 different metabolites were identified in individual neurons. In the same approach of CE and MS, Amantonico *et al.*[102] showed the detection of metabolites including UDP, ADP, GDP, UTP, ATP, GTP, acetyl-CoA, and butyryl/isobutyryl-CoA at the single yeast cell level.

Fluorescence-based detection is another common method to monitor metabolites at the single-cell level. The advantage of fluorescence is that the method is sensitive, nondestructive and high-throughput. These assays usually use fluorescent tags attached to molecules of interest and a readout with fluorescence microscopy or flow cytometry. Nevertheless, the fluorescence-based method can only detect a few metabolites directly in single cells due to labelling difficulty, hence limiting the application capability. Moreover, the labelling technique is too invasive for single-cell metabolomics and may alter the metabolites' activities. Hence methods that provide fluorescent readout without labelling target interest are preferable. Biosensors based on Förster resonance energy transfer (FRET) have been explored for single-cell analysis, for example, fluorescent

proteins (FPs). A pair of FPs comprises a donor and an acceptor. The binding of metabolites to FPs induces the conformational change, generating the fluorescence signal. Numerous fluorescence-based FRET methods have been developed to detect ATP. For example, the ε subunit of the bacterial F_oF_1-ATP synthase comprising one N-terminal β-barrel domain and two C-terminal α-helices undergoes a large conformational change into a folded form upon ATP binding; the bundling of the two α-helices generates a fluorescent detection signal.[103] Other examples used nanoflares comprising gold nanoparticles functionalized with ATP-aptamer as fluorescent transducers.[104,105] A short internal complementary strand containing a terminal fluorophore is hybridized onto the aptamers. The fluorescence is quenched when bound in close proximity to gold nanoparticles. In the presence of ATP and upon its binding, the ATP aptamer changes its conformation, which displaces the short flare strands and results in a "turn-on" fluorescence signal proportional to the concentration of targets. Nanoflares can resist enzymatic degradation by nucleases and enter living cells to quantify ATP and other metabolites such as mRNA expression without the significant disruption of cellular homeostasis.

Electrochemical detection shows a high sensitivity making it capable of single-cell analysis. It can be used as label-free detection of metabolites intracellular and extracellular environment.[106] However, only electroactive species can be analyzed, making the electrochemical methods applicable only to limited metabolites in single cells. The micro- and nanoscale electrode methods can be used to detect various metabolites such as neurotransmitters,[107] catecholamines[108] and intracellular ATP.[109]

Single-cell metabolomics can offer opportunities for studying cell heterogeneity but also have challenges due to the limited sample volume, low analyte amounts, and rapid turnover rates of the cellular metabolome. Overcoming the limitations is the main challenge for highly sensitive and

quantifiable single-cell metabolomics assays. MS is a powerful method for single-cell metabolomics and profiling, but it is a destructive assay. Fluorescence-based biosensors are highly sensitive and non-destructive, but photobleaching and blinking are to be considered. It has been shown that microfluidics and capillary electrophoresis as separation techniques combined with detection methods such as fluorescence or mass spectrometry analysis are promising techniques for single-cell metabolome studies. However, most single-cell investigations are time-consuming, highly complex and require expensive instruments. We developed the stick-and-peel sensing patch using core-satellite nanostructure for rapid single-cell analysis without the need for sophisticated instruments (see Chapter 3).

1.6 Outline of Thesis

This PhD thesis presents the development of biosensors using plasmonic nanoparticles. Four peer-reviewed publications are presented in Chapters 2-5. The outline of each chapter is listed below.

Chapter 2 demonstrates the detection of ATP using a plasmonic core-satellite structure. The complex nanostructure leads to the enhancement of scattered light intensity due to plasmon coupling. Using ATP aptamer as linkers, the sensing platform can be achieved via the disassembly of the nanostructure through target-induced dehybridization of DNA linkers. We demonstrated a rapid and simple detection platform by monitoring the light scattering of NPs using darkfield images. We also showed the tunable detection range by controlling the number of satellite NPs; the increasing number of satellite NPs can enhance the detection signal and lead to increased sensitivity. Additionally, the sensing performances such as selectivity, and specificity were examined.

Building on chapter 2, chapter 3 demonstrates the detection of ATP at the single-cell level using discrete core-satellite nanostructures. Sensing platforms based on a single plasmonic nanostructure can offer a rapid and simple methodology for the biomolecular analysis of single cells and microenvironments. The detection can be achieved via a stick-and-peel plasmonic sensing platform which eliminates labeling, purification, and separation steps. We developed a method of quantitative analysis based on the scattering intensity from each nanostructure. Changes in the light scattering intensity of thousands of discrete nanoparticle assemblies were extrapolated concomitantly to yield the mapping of local target concentrations. We quantified the intracellular ATP levels for two ovarian cancer cell lines to elucidate the differences and cellular distribution and demonstrated the potential for mapping the microenvironment of a 2D heterogeneous surface.

An important aspect in the development of optical biosensors is tunable optical properties that enable expanded detection range, enhanced sensitivity and multiplexing. Chapter 4 reports the tunable optical properties of core-satellite nanostructure using gold nanoshells. We studied experimentally and theoretically the optical properties of nanostructure comprising Au solid core and Au shell satellites. We observed the enhancement of scattering intensity as well as the color change to a longer wavelength compared to the structure of Au solid core with Au solid satellites. The scattered color of the nanostructure was analyzed based on the hue value from the color analysis of hue, saturation and intensity (HSI analysis). The sensing of ATP was achieved based on a decrease of scattering intensity through the disassembly of nanoparticle assemblies, and the potential to color-code plasmonic nanostructures through morphological composition was demonstrated.

Multiplexing, or the ability to detect multiple targets simultaneously in one sample, is desirable and sensors based on individual nanostructure are ideal candidates for optical

multiplexing. In chapter 5, we present a duplexed assay using discrete nanostructures. Two types of assemblies using DNA linkers that target different molecules – ATP and miRNA were fabricated in the common area via the layer-by-layer process. To fabricate these nanostructures, the challenge of cross-hybridization between DNA linkers was addressed and overcome by engineering DNA capping sequences. Multiplexed detection was demonstrated by the selective disassembly of different targeting nanostructures. Additionally, we also explored the tunable optical properties of nanoparticle assemblies for multiplexing. By using different nanoparticle morphologies where two types of nanostructures (e.g. Au solid core and Au solid satellite, and Au solid core and Au shell satellite) were fabricated in the common area using different DNA linkers, we showed the duplexed detection of ATP and a microRNA based on the change in the scattering intensity and the color read-out.

1.7 References

(1) Masson, J.-F. Portable and Field-Deployed Surface Plasmon Resonance and Plasmonic Sensors. *Analyst* **2020**, *145*, 3776–3800.

(2) Kelly, K. L.; Coronado, E.; Zhao, L. L.; Schatz, G. C. The Optical Properties of Metal Nanoparticles: The Influence of Size, Shape, and Dielectric Environment. *J. Phys. Chem. B* **2003**, *107*, 668–677.

(3) Jain, P. K.; Huang, X.; El-Sayed, I. H.; El-Sayed, M. A. Noble Metals on the Nanoscale: Optical and Photothermal Properties and Some Applications in Imaging, Sensing, Biology, and Medicine. *Acc. Chem. Res.* **2008**, *41*, 1578–1586.

(4) Haes, A. J.; Van Duyne, R. P. A Nanoscale Optical Biosensor: Sensitivity and Selectivity of an Approach Based on the Localized Surface Plasmon Resonance Spectroscopy of Triangular Silver Nanoparticles. *J. Am. Chem. Soc.* **2002**, *124*, 10596–10604.

(5) Mie, G. Beiträge Zur Optik Trüber Medien, Speziell Kolloidaler Metallösungen. *Ann. Phys.* **1908**, *330*, 377–445.

(6) Jain, P. K.; El-Sayed, M. A. Surface Plasmon Resonance Sensitivity of Metal Nanostructures: Physical Basis and Universal Scaling in Metal Nanoshells. *J. Phys. Chem. C* **2007**, *111*, 17451–17454.

(7) Jain, P. K.; El-Sayed, M. A. Plasmonic Coupling in Noble Metal Nanostructures. *Chem. Phys. Lett.* **2010**, *487*, 153–164.

(8) Petryayeva, E.; Krull, U. J. Localized Surface Plasmon Resonance: Nanostructures, Bioassays and Biosensing-A Review. *Anal. Chim. Acta* **2011**, *706*, 8–24.

(9) P. B. Johnson and R. W. Christy. Optical Constant of the Nobel Metals. *Phys. Rev. B* **1972**, *6*, 4370–4379.

(10) Mayer, K. M.; Hafner, J. H.; Antigen, A. À. Localized Surface Plasmon Resonance Sensors. *Chem. Rev.* **2011**, *111*, 3828–3857.

(11) Raschke, G.; Kowarik, S.; Franzl, T.; Sönnichsen, C.; Klar, T. A.; Feldmann, J.; Nichtl, A.; Kürzinger, K. Biomolecular Recognition Based on Single Gold Nanoparticle Light Scattering. *Nano Lett.* **2003**, *3*, 935–938.

(12) Haes, A. J.; Chang, L.; Klein, W. L.; Duyne, R. P. Van; Van Duyne, R. P. Detection of a Biomarker for Alzheimer ' s Disease from Synthetic and Clinical Samples Using a Nanoscale Optical Biosensor. *J. Am. Chem. Soc.* **2005**, *127*, 2264–2271.

(13) Willets, K. A.; Van Duyne, R. P. Localized Surface Plasmon Resonance Spectroscopy and Sensing. *Annu. Rev. Phys. Chem* **2007**, *58*, 267–297.

(14) Jensen, T. R.; Duval, M. L.; Lance Kelly, K.; Lazarides, A. A.; Schatz, G. C.; Van Duyne, R. P. Nanosphere Lithography: Effect of the External Dielectric Medium on the Surface Plasmon Resonance Spectrum of a Periodic Array of Silver Nanoparticles. *J. Phys. Chem. B* **1999**, *103*, 9846–9853.

(15) Unser, S.; Bruzas, I.; He, J.; Sagle, L. Localized Surface Plasmon Resonance Biosensing: Current Challenges and Approaches. *Sensors* **2015**, *15*, 15684–15716.

(16) Sagle, L. B.; Ruvuna, L. K.; Ruemmele, J. A.; Van Duyne, R. P. Advances in Localized Surface Plasmon Resonance Spectroscopy Biosensing. *Nanomedicine* **2011**, *6*, 1447–1462.

(17) Lee, K. S.; El-Sayed, M. A. Gold and Silver Nanoparticles in Sensing and Imaging: Sensitivity of Plasmon Response to Size, Shape, and Metal Composition. *J. Phys. Chem. B* **2006**, *110*, 19220–19225.

(18) Mock, J. J.; Smith, D. R.; Schultz, S. Local Refractive Index Dependence of Plasmon Resonance Spectra from Individual Nanoparticles. *Nano Lett.* **2003**, *3*, 485–491.

(19) Miller, M. M.; Lazarides, A. A. Sensitivity of Metal Nanoparticle Plasmon Resonance Band Position to the Dielectric Environment as Observed in Scattering. *J. Opt. A Pure Appl. Opt.* **2006**, *8*, 21556–21565.

(20) Lee, S. W.; Lee, K. S.; Ahn, J.; Lee, J. J.; Kim, M. G.; Shin, Y. B. Highly Sensitive Biosensing Using Arrays of Plasmonic Au Nanodisks Realized by Nanoimprint Lithography. *ACS Nano* **2011**, *5*, 897–904.

(21) Hall, W. P.; Ngatia, S. N.; Van Duyne, R. P. LSPR Biosensor Signal Enhancement Using Nanoparticle-Antibody Conjugates. *J. Phys. Chem. C* **2011**, *115*, 1410–1414.

(22) Ruemmele, J. A.; Hall, W. P.; Ruvuna, L. K.; Van Duyne, R. P. A Localized Surface Plasmon Resonance Imaging Instrument for Multiplexed Biosensing. *Anal. Chem.* **2013**, *85*, 4560–4566.

(23) Chen, P.; Chung, M. T.; McHugh, W.; Nidetz, R.; Li, Y.; Fu, J.; Cornell, T. T.; Shanley, T. P.; Kurabayashi, K. Multiplex Serum Cytokine Immunoassay Using Nanoplasmonic Biosensor Microarrays. *ACS Nano* **2015**, *9*, 4173–4181.

(24) Prodan, E.; Nordlander, P. Plasmon Hybridization in Spherical Nanoparticles. *J. Chem. Phys.* **2004**, *120*, 5444–5454.

(25) Mandl, F.; Graham, S. *Quantum Field Theory*; 2nd ed.; Wiley, 2010.

(26) Prodan, E.; Radloff, C.; Halas, N. J.; Nordlander, P. A Hybridization Model for the Plasmon Response of Complex Nanostructures. *Science* **2003**, *302*, 419–422.

(27) Nordlander, P.; Oubre, C.; Prodan, E.; Li, K.; Stockman, M. I. Plasmon Hybridization in Nanoparticle Dimers. *Nano Lett.* **2004**, *4*, 899–903.

(28) Jain, P. K.; Huang, W.; El-Sayed, M. A. On the Universal Scaling Behavior of the Distance Decay of Plasmon Coupling in Metal Nanoparticle Pairs: A Plasmon Ruler Equation. *Nano Lett.* **2007**, *7*, 2080–2088.

(29) Rechberger, W.; Hohenau, a.; Leitner, a.; Krenn, J. R.; Lamprecht, B.; Aussenegg, F. R. Optical Properties of Two Interacting Gold Nanoparticles. *Opt. Commun.* **2003**, *220*, 137–141.

(30) Sheikholeslami, S.; Jun, Y. W.; Jain, P. K.; Alivisatos, A. P. Coupling of Optical

Resonances in a Compositionally Asymmetric Plasmonic Nanoparticle Dimer. *Nano Lett.* **2010**, *10*, 2655–2660.

(31) Deng, T. S.; Parker, J.; Yifat, Y.; Shepherd, N.; Scherer, N. F. Dark Plasmon Modes in Symmetric Gold Nanoparticle Dimers Illuminated by Focused Cylindrical Vector Beams. *J. Phys. Chem. C* **2018**, *122*, 27662–27672.

(32) Hoeing, D.; Schulz, F.; Mueller, N. S.; Reich, S.; Lange, H. Dark Plasmon Modes for Efficient Hot Electron Generation in Multilayers of Gold Nanoparticles. *J. Chem. Phys.* **2020**, *152*, 064710.

(33) Langer, J.; de Aberasturi, D. J.; Aizpurua, J.; Alvarez-Puebla, R. A.; Auguié, B.; Baumberg, J. J.; Bazan, G. C.; Bell, S. E. J.; Boisen, A.; Brolo, A. G.; *et al.* Present and Future of Surface-Enhanced Raman Scattering. *ACS Nano* **2020**, *14*, 28–117.

(34) Barrow, S. J.; Rossouw, D.; Funston, A. M.; Botton, G. A.; Mulvaney, P. Mapping Bright and Dark Modes in Gold Nanoparticle Chains Using Electron Energy Loss Spectroscopy. *Nano Lett.* **2014**, *14*, 3799–3808.

(35) Ghosh, S. K.; Pal, T. Interparticle Coupling Effect on the Surface Plasmon Resonance of Gold Nanoparticles : From Theory to Applications. *Chem. Rev.* **2007**, *107*, 4797–4862.

(36) Brown, L. V.; Sobhani, H.; Lassiter, J. B.; Nordlander, P.; Halas, N. J. Heterodimers: Plasmonic Properties of Mismatched Nanoparticle Pairs. *ACS Nano* **2010**, *4*, 819–832.

(37) Wang, H.; Halas, N. J. Plasmonic Nanoparticle Heterodimers in a Semiembedded Geometry Fabricated by Stepwise Upright Assembly. *Nano Lett.* **2006**, *6*, 2945–2948.

(38) Höller, R. P. M.; Jahn, I. J.; Cialla-May, D.; Chanana, M.; Popp, J.; Fery, A.; Kuttner, C. Biomacromolecular-Assembled Nanoclusters: Key Aspects for Robust Colloidal SERS Sensing. *ACS Appl. Mater. Interfaces* **2020**, *12*, 57302–57313.

(39) Prasad, J.; Zins, I.; Branscheid, R.; Becker, J.; Koch, A. H. R.; Fytas, G.; Kolb, U.; Sönnichsen, C. Plasmonic Core-Satellite Assemblies as Highly Sensitive Refractive Index Sensors. *J. Phys. Chem. C* **2015**, *119*, 5577–5582.

(40) Waldeisen, J. R. R.; Wang, T.; Ross, B. M. M.; Lee, L. P. P. Disassembly of a Core–Satellite Nanoassembled Substrate for Colorimetric Biomolecular Detection. *ACS Nano* **2011**, *5*, 5383–5389.

(41) Höller, R. P. M.; Dulle, M.; Thomä, S.; Mayer, M.; Steiner, A. M.; Förster, S.; Fery, A.; Kuttner, C.; Chanana, M. Protein-Assisted Assembly of Modular 3D Plasmonic Raspberry-like Core/Satellite Nanoclusters: Correlation of Structure and Optical Properties. *ACS Nano* **2016**, *10*, 5740–5750.

(42) Kuttner, C.; Höller, R. P. M.; Quintanilla, M.; Schnepf, M. J.; Dulle, M.; Fery, A.; Liz-Marzán, L. M. SERS and Plasmonic Heating Efficiency from Anisotropic Core/Satellite Superstructures. *Nanoscale* **2019**, *11*, 17655–17663.

(43) Yoon, J. H.; Yoon, S. Probing Interfacial Interactions Using Core-Satellite Plasmon Rulers. *Langmuir* **2013**, *29*, 14772–14778.

(44) Yoon, J. H.; Yoon, S. Effects of the Number of Satellites on Surface Plasmon Coupling of Core-Satellite Nanoassemblies. *Bull. Korean Chem. Soc.* **2013**, *34*, 33–34.

(45) Ross, B. M.; Waldeisen, J. R.; Wang, T.; Lee, L. P. Strategies for Nanoplasmonic Core-Satellite Biomolecular Sensors: Theory-Based Design. *Appl. Phys. Lett.* **2009**, *95*, 193112.

(46) Yoon, J. H.; Zhou, Y.; Blaber, M. G.; Schatz, G. C.; Yoon, S. Surface Plasmon Coupling of Compositionally Heterogeneous Core-Satellite Nanoassemblies. *J. Phys. Chem. Lett.* **2013**, *4*, 1371–1378.

(47) Yoon, J. H.; Lim, J.; Yoon, S. Controlled Assembly and Plasmonic Properties of Asymmetric Core-Satellite Nanoassemblies. *ACS Nano* **2012**, *6*, 7199–7208.

(48) Oldenburg, S. J.; Averitt, R. D.; Westcott, S. L.; Halas, N. J. Nanoengineering of Optical Resonances. *Chem. Phys. Lett.* **1998**, *288*, 243–247.

(49) Jackson, J. B.; Halas, N. J. Silver Nanoshells: Variations in Morphologies and Optical Properties. *J. Phys. Chem. B* **2001**, *105*, 2743–2746.

(50) Wang, H.; Brandl, D. W.; Nordlander, P.; Halas, N. J. Plasmonic Nanostructures: Artificial Molecules. *Acc. Chem. Res.* **2007**, *40*, 53–62.

(51) Elghanian, R., James J. Storhoff, Robert C. Mucic, Robert L. Letsinger, C. A. M. Selective Colorimetric Detection of Polynucleotides Based on the Distance-Dependent Optical Properties of Gold Nanoparticles. *Science* **1997**, *277*, 1078–1081.

(52) Liu, J.; Lu, Y. Fast Colorimetric Sensing of Adenosine and Cocaine Based on a General Sensor Design Involving Aptamers and Nanoparticles. *Angew. Chemie Int. Ed.* **2006**, *45*, 90–94.

(53) Mulvaney, P. Surface Plasmon Spectroscopy of Nanosized Metal Particles. *Langmuir* **1996**, *12*, 788–800.

(54) Sonntag, M. D.; Klingsporn, J. M.; Zrimsek, A. B.; Sharma, B.; Ruvuna, L. K.; Van Duyne, R. P. Molecular Plasmonics for Nanoscale Spectroscopy. *Chem. Soc. Rev.* **2014**, *43*, 1230–1247.

(55) Truong, P. L.; Cao, C.; Park, S.; Kim, M.; Sim, S. J. A New Method for Non-Labeling Attomolar Detection of Diseases Based on an Individual Gold Nanorod Immunosensor. *Lab Chip* **2011**, *11*, 2591–2597.

(56) Ament, I.; Prasad, J.; Henkel, A.; Schmachtel, S.; Sönnichsen, C. Single Unlabeled Protein Detection on Individual Plasmonic Nanoparticles. *Nano Lett.* **2012**, *12*, 1092–1095.

(57) Jain, P. K.; Huang, X.; El-Sayed, I. H.; El-Sayed, M. A. Review of Some Interesting Surface Plasmon Resonance-Enhanced Properties of Noble Metal Nanoparticles and Their Applications to Biosystems. *Plasmonics* **2007**, *2*, 107–118.

(58) Cathcart, N.; Chen, J. I. L. Sensing Biomarkers with Plasmonics. *Anal. Chem.* **2020**, *92*, 7373–7381.

(59) Lubert, S. Flourescence Energy Transfer As a Spectrocopic Ruler. *Annu. Rev. Biochem.*

1978, 819–846.

(60) Ray, P. C.; Fan, Z.; Crouch, R. A.; Sinha, S. S.; Pramanik, A.; Fan, Z. Chem Soc Rev Nanoscopic Optical Rulers beyond the FRET Distance Limit : Fundamentals and Applications. *Chem. Soc. Rev.* **2014**, *43*, 6370–6404.

(61) Sönnichsen, C.; Reinhard, B. M.; Liphardt, J.; Alivisatos, A. P.; Sonnichsen, C.; Reinhard, B. M.; Liphard, J.; Alivisatos, A. P. A Molecular Ruler Based on Plasmon Coupling of Single Gold and Silver Nanoparticles. *Nat. Biotechnol.* **2005**, *23*, 741–745.

(62) Liphardt, J.; Reinhard, B. M.; Siu, M.; Agarwal, H.; Alivisatos, A. P.; Liphardt, J.; Reinhard, B. M.; Siu, M.; Agarwal, H.; Alivisatos, A. P.; *et al.* Calibration of Dynamic Molecular Rulers Based on Plasmon Coupling between Gold Nanoparticles. *Nano Lett.* **2005**, *5*, 2246–2252.

(63) Liu, N.; Hentschel, M.; Weiss, T.; Alivisatos, A. P.; Giessen, H. Three-Dimensional Plasmon Rulers. *Science (80-.).* **2011**, *332*, 1407–1410.

(64) Waldeisen, J. R.; Wang, T.; Ross, B. M.; Lee, L. P. Disassembly of a Core-Satellite Nanoassembled Substrate for Colorimetric Biomolecular Detection. In *ACS Nano*; 2011.

(65) Jun, Y.; Sheikholeslami, S.; Hostetter, D. R.; Tajon, C.; Craik, C. S.; Alivisatos, A. P. Continuous Imaging of Plasmon Rulers in Live Cells Reveals Early-Stage Caspase-3 Activation at the Single-Molecule Level. *Proc. Natl. Acad. Sci. U. S. A.* **2009**, *106*, 17735–17740.

(66) Chen, J. I. L.; Chen, Y.; Ginger, D. S. Plasmonic Nanoparticle Dimers for Optical Sensing of DNA in Complex Media. *J. Am. Chem. Soc.* **2010**, *132*, 9600–9601.

(67) Wang, G.; Guo, Y.; Liu, Y.; Zhou, W.; Wang, G. Algorithm-Assisted Detection and Imaging of MicroRNAs in Living Cancer Cells via the Disassembly of Plasmonic Core-Satellite Probes Coupled with Strand Displacement Amplification. *ACS Sensors* **2021**, *6*, 958–966.

(68) Hwu, S.; Blickenstorfer, Y.; Raphael F., T.; Gonnelli, C.; Schmidheini, L.; Lüchtefeld, I.; Hoogenberg, B.-J.; Gisiger, A.; Vörös, J. Dark-Field Microwells for High-Throughput Direct MiRNA Sensing with Gold Nanoparticles. *ACS Sensors* **2019**, *4*, 1950–1956.

(69) Zhang, T.; Li, H.; Hou, S.; Dong, Y.; Pang, G.; Zhang, Y. Construction of Plasmonic Core-Satellite Nanostructures on Substrates Based on DNA-Directed Self-Assembly as a Sensitive and Reproducible Biosensor. *ACS Appl. Mater. Interfaces* **2015**, *7*, 1–5.

(70) Storhoff, J. J.; Lazarides, A. A.; Mucic, R. C.; Mirkin, C. A.; Letsinger, R. L.; Schatz, G. C. What Controls the Optical Properties of DNA-Linked Gold Nanoparticle Assemblies ? *J. Am. Chem. Soc.* **2000**, *122*, 4640–4650.

(71) Love, J. C.; Estroff, L. A.; Kriebel, J. K.; Nuzzo, R. G.; Whitesides, G. M. *Self-Assembled Monolayers of Thiolates on Metals as a Form of Nanotechnology*; 2005; Vol. 105.

(72) Liu, B.; Liu, J. Methods for Preparing DNA-Functionalized Gold Nanoparticles, a Key Reagent of Bioanalytical Chemistry. *Anal. Methods* **2017**, *9*, 2633–2643.

(73) Storhoff, J. J.; Elghanian, R.; Mucic, R. C.; Mirkin, C. A.; Letsinger, R. L. One-Pot Colorimetric Differentiation of Polynucleotides with Single Base Imperfections Using Gold Nanoparticle Probes. *J. Am. Chem. Soc.* **1998**, *120*, 1959–1964.

(74) Tajon, C. A.; Seo, D.; Asmussen, J.; Shah, N.; Jun, Y. W.; Craik, C. S. Sensitive and Selective Plasmon Ruler Nanosensors for Monitoring the Apoptotic Drug Response in Leukemia. *ACS Nano* **2014**, *8*, 9199–9208.

(75) El-Sayed, I. H.; Huang, X.; El-Sayed, M. A. Surface Plasmon Resonance Scattering and Absorption of Anti-EGFR Antibody Conjugated Gold Nanoparticles in Cancer Diagnostics: Applications in Oral Cancer. *Nano Lett.* **2005**, *5*, 829–834.

(76) Song, K. M.; Lee, S.; Ban, C. Aptamers and Their Biological Applications. *Sensors* **2012**, *12*, 612–631.

(77) Tuerk, C.; Gold, L. Systematic Evolution of Ligands by Exponential Enrichment: RNA Ligands to Bacteriophage T4 DNA Polymerase. *Science* **1990**, *249*, 505–510.

(78) Ellington, A. ; Szostak, J. In Vitro Selection of RNA Molecules That Bind Specific Ligands. *Nature* **1990**, *346*, 818–822.

(79) Keefe, A. D.; Pai, S.; Ellington, A. Aptamers as Therapeutics. *Nat. Rev. Drug Discov.* **2010**, *9*, 537–550.

(80) Zhou, W.; Jimmy Huang, P.-J.; Ding, J.; Liu, J. Aptamer-Based Biosensors for Biomedical Diagnostics. *Analyst* **2014**, *139*, 2627.

(81) Huizenga, D. E.; Szostak, J. W. A DNA Aptamer That Binds Adenosine and ATP. *Biochemistry* **1995**, *34*, 656–665.

(82) Lin, C. H.; Patel, D. J. Structural Basis of DNA Folding and Recognition in an AMP-DNA Aptamer Complex: Distinct Architectures but Common Recognition Motifs for DNA and RNA Aptamers Complexed to AMP. *Chem. Biol.* **1997**, *4*, 817–832.

(83) Zhang, Z.; Oni, O.; Liu, J. New Insights into a Classic Aptamer: Binding Sites, Cooperativity and More Sensitive Adenosine Detection. *Nucleic Acids Res.* **2017**, *4567*, 2–10.

(84) Xie, Y. C.; Eriksson, L. A.; Zhang, R. B. Molecular Dynamics Study of the Recognition of ATP by Nucleic Acid Aptamers. *Nucleic Acids Res.* **2020**, *48*, 6471–6480.

(85) Slavkovic, S.; Zhu, Y.; Churcher, Z. R.; Shoara, A. A.; Johnson, A. E.; Johnson, P. E. Thermodynamic Analysis of Cooperative Ligand Binding by the ATP-Binding DNA Aptamer Indicates a Population-Shift Binding Mechanism. *Sci. Rep.* **2020**, *10*, 1–10.

(86) Munzar, J. D.; Ng, A.; Juncker, D. Duplexed Aptamers: History, Design, Theory, and Application to Biosensing. *Chem. Soc. Rev.* **2019**, *48*, 1390–1419.

(87) Xia, T.; Yuan, J.; Fang, X. Conformational Dynamics of an ATP-Binding DNA Aptamer: A Single-Molecule Study. *J. Phys. Chem. B* **2013**, *117*, 14994–15003.

(88) Arnaut, V.; Langecker, M.; Simmel, F. C. Nanopore Force Spectroscopy of Aptamer-Ligand Complexes. *Biophys. J.* **2013**, *105*, 1199–1207.

(89) Seferos, D. S.; Giljohann, D. A.; Hill, H. D.; Prigodich, A. E.; Mirkin, C. A. Nano-Flares: Probes for Transfection and MRNA Detection in Living Cells. *J. Am. Chem. Soc.* **2007**, *129*, 15477–15479.

(90) Yaginuma, H.; Kawai, S.; Tabata, K. V.; Tomiyama, K.; Kakizuka, A.; Komatsuzaki, T.; Noji, H.; Imamura, H. Diversity in ATP Concentrations in a Single Bacterial Cell Population Revealed by Quantitative Single-Cell Imaging. *Sci. Rep.* **2014**, *4*, 6522.

(91) Jia, J.; Feng, J.; Chen, H. G.; Luo, H. Q.; Li, N. B. A Simple Electrochemical Method for the Detection of ATP Using Target-Induced Conformational Change of Dual-Hairpin DNA Structure. *Sensors Actuators, B Chem.* **2016**, *222*, 1090–1095.

(92) Porchetta, A.; Vallée-Bélisle, A.; Plaxco, K. W.; Ricci, F. Using Distal-Site Mutations and Allosteric Inhibition to Tune, Extend, and Narrow the Useful Dynamic Range of Aptamer-Based Sensors. *J. Am. Chem. Soc.* **2012**, *134*, 20601–20604.

(93) Munzar, J. D.; Ng, A.; Corrado, M.; Juncker, D. Complementary Oligonucleotides Regulate Induced Fit Ligand Binding in Duplexed Aptamers. *Chem. Sci.* **2017**, *8*, 2251–2256.

(94) Munzar, J. D.; Ng, A.; Juncker, D. Comprehensive Profiling of the Ligand Binding Landscapes of Duplexed Aptamer Families Reveals Widespread Induced Fit. *Nat. Commun.* **2018**, *9*, 1–15.

(95) Nutiu, R.; Li, Y. Structure-Switching Signaling Aptamers. *J. Am. Chem. Soc.* **2003**, *125*, 4771–4778.

(96) Altschuler, S. J.; Wu, L. F. Cellular Heterogeneity : Do Differences Make a Difference ? *Cell* **2010**, *141*, 559–563.

(97) Rubakhin, S. S.; Romanova, E. V.; Nemes, P.; Sweedler, J. V. Profiling Metabolites and Peptides in Single Cells. *Nat. Methods* **2011**, *8*, S20–S29.

(98) Heinemann, M.; Zenobi, R. Single Cell Metabolomics. *Curr. Opin. Biotechnol.* **2011**, *22*, 26–31.

(99) Zhang, X. C.; Wei, Z. W.; Gong, X. Y.; Si, X. Y.; Zhao, Y. Y.; Yang, C. D.; Zhang, S. C.; Zhang, X. R. Integrated Droplet-Based Microextraction with ESI-MS for Removal of Matrix Interference in Single-Cell Analysis. *Sci. Rep.* **2016**, *6*, 1–9.

(100) Bergman, H. M.; Lanekoff, I. Profiling and Quantifying Endogenous Molecules in Single Cells Using Nano-DESI MS. *Analyst* **2017**, *142*, 3639–3647.

(101) Nemes, P.; Knolho, A. M.; Rubakhin, S. S.; Sweedler, J. V. Metabolic Differentiation of Neuronal Phenotypes by Single-Cell Capillary Electrophoresis — Electrospray Ionization-Mass Spectrometry. *Anal. Chem.* **2011**, *83*, 6810–6817.

(102) Amantonico, A.; Oh, J. Y.; Sobek, J.; Heinemann, M.; Zenobi, R. Mass Spectrometric Method for Analyzing Metabolites in Yeast with Single Cell Sensitivity. *Angew. Chemie - Int. Ed.* **2008**, *47*, 5382–5385.

(103) Imamura, H.; Huynh Nhat, K. P.; Togawa, H.; Saito, K.; Iino, R.; Kato-Yamada, Y.;

Nagai, T.; Noji, H. Visualization of ATP Levels inside Single Living Cells with Fluorescence Resonance Energy Transfer-Based Genetically Encoded Indicators. *Proc. Natl. Acad. Sci. U. S. A.* **2009**, *106*, 15651–15656.

(104) Zheng, D.; Seferos, D. S.; Giljohann, D. A.; Patel, P. C.; Mirkin, C. A. Aptamer Nano-Flares for Molecular Detection in Living Cells. *Nano Lett.* **2009**, *9*, 3258–3261.

(105) Randeria, P. S.; Briley, W. E.; Chinen, A. B.; Guan, C. M.; Petrosko, S. H.; Mirkin, C. A. Nanoflares as Probes for Cancer Diagnostics. In *Nanotechnology-Based Precision Tools for the Detection and Treatment of Cancer*; Mirkin, C. A.; Meade, T. J.; Petrosko, S. H.; Stegh, A. H., Eds.; Springer International Publishing: Cham, 2015; pp. 1–22.

(106) Cannon, D. M.; Winograd, N.; Ewing, A. G. Quantitative Chemical Analysis of Single Cells. *Annu. Rev. Biophys. Biomol. Struct* **2000**, *29*, 239–263.

(107) Chien, J. B.; Wallingford, R. A.; Ewing, A. G. Estimation of Free Dopamine in the Cytoplasm of the Giant Dopamine Cell of Planorbis Corneus by Voltammetry and Capillary Electrophoresis. *J. Neurochem.* **1990**, *54*, 633–638.

(108) Finnegan, J. M.; Pihel, K.; Cahill, P. S.; Huang, L.; Zerby, S. E.; Ewing, A. G.; Kennedy, R. T.; Wightman, R. M. Vesicular Quantal Size Measured by Amperometry at Chromaffin, Mast, Pheochromocytoma, and Pancreatic β-Cells. *J. Neurochem.* **1996**, *66*, 1914–1923.

(109) Ruan, Y. F.; Wang, H. Y.; Shi, X. M.; Xu, Y. T.; Yu, X. D.; Zhao, W. W.; Chen, H. Y.; Xu, J. J. Target-Triggered Assembly in a Nanopipette for Electrochemical Single-Cell Analysis. *Anal. Chem.* **2021**, *93*, 1200–1208.

Chapter 2 – Tuning the Sensing Performance of Multilayer Plasmonic Core-satellite Assemblies for Rapid Detection of Targets from Lysed Cells

(This chapter is partly reproduced with permission from Le, N. H.; Nguyen, B. K.; Ye, G.; Peng, C.; Chen, J. I. L. *ACS Sens.* **2017**, *2*, 1578–1583. Copyright 2017 American Chemical Society. Preliminary development of the fabrication method and characterizations were carried out in M.Sc. All sensing work was finalized in Ph.D.)

(Cells were cultured by Gang Ye. All experiments presented in this chapter were carried out by Nguyen Le)

2.1 Abstract

Optical sensors based on discrete plasmonic nanostructures are invaluable for probing biomolecular interactions when applied as plasmonic rulers or reconfigurable multi-nanoparticle assemblies. However, their adaptation as a versatile sensing platform is limited by the research-grade instrumentation required for single-nanostructure imaging and/or spectroscopy and complex data fitting and analysis. Additionally, the dynamic range is often too narrow for the quantitative analysis of targets of interest in bio-diagnostics, food safety or environmental monitoring. In this chapter, we present plasmonic assembly comprising a core nanoparticle surrounded by multiple layers of satellite nanoparticles through aptamer linkers for sensing applications. The layer-by-layer assembly of the satellite nanoparticles yields uniform discrete nanoparticle clusters on a substrate with enhanced optical properties. Binding of the model target (adenosine 5'-triphosphate, ATP) induces disassembly and leads to a dramatic decrease in the scattering intensity that can be analyzed readily from dark-field images. We demonstrate that the sensing performance, such as detection limit, dynamic range, and sensitivity, can be tuned by controlling the size of the

assembly. The substrate-anchored nanoparticle assemblies are selective to only ATP, and not to other adenine-containing compounds. By adapting the methodology to a flexible support, cellular ATP can be directly detected by lysing adherent cells in close contact with the plasmonic assemblies – a process that does not require any sample preparation or purification. Enhancing the optical detection signal via designing and engineering nanoparticle assemblies could enable their use with low-cost portable imaging systems and broaden their applicability beyond the study of biomolecular interaction.

2.2 Introduction

Sensors based on plasmonic nanostructures are explored for rapid, highly sensitive and specific detection of targets. Noble metal nanoparticles (e.g. Au and Ag) exhibit localized surface plasmon resonance (LSPR) that gives rise to strong light absorption and scattering, which does not suffer from photoblinking or photobleaching.[1,2] Combined with their low toxicity, biocompatibility, and ease of surface functionalization, plasmonic metal nanoparticles have been explored as better visual labels in biosensing systems. They have been established for colloidal-based or substrate-based sensing. Detection with colloidal solutions relies on the aggregation of nanoparticles (or dissociation of aggregates) upon binding of targets, which leads to striking color change.[3–9] Although the colorimetric detection is observable by the naked eye, colloidal-based sensors suffer from several drawbacks including moderately low detection limits, and susceptibility to false positive readouts due to aggregation of nanoparticles caused by changes in pH, temperature, or salt concentration. Hence, detection strategies employing nanostructures immobilized on substrates can serve as alternative miniaturized sensing platforms, in particular for integration with on-chip separation or purification schemes such as those employed in microfluidics.

Discrete multi-nanoparticle plasmonic assemblies, including dimers[10–15] and core-satellite structures of gold nanoparticles (AuNPs), have been explored as chip-based sensors and plasmonic rulers for detecting single-molecule binding events.[16–18] These coupled structures exploit the phenomenon of distance-dependent plasmon hybridization,[19,20] in which the energy and strength of the hybridized plasmon modes can be altered upon the binding of the target to the reconfigurable biomolecular linker[21] to yield shifts in the LSPR peak or changes in the scattering intensity. Of the different plasmonic structures, core-satellite assemblies are advantageous because the controlled fabrication process can yield multiple design capabilities that give rise to high scattering intensity. The plasmonic properties can be tuned by altering parameters such as the sizes of the core and satellite nanoparticles and the number of satellite nanoparticles.[22,23] The multi-nanoparticle assemblies – up to a monolayer of satellite nanoparticles around a single core nanoparticle – have been studied experimentally and theoretically.[16,22] For example, the combination of 50-nm core AuNP with 30-nm satellite AuNPs has been shown to exhibit a large change in LSPR upon assembly. These structures have been applied to sensing biomolecular interaction by employing peptide or oligonucleotide linkers that can be cleaved by enzymes such as caspase-3,[18] protease,[16] or telomerase.[17] The disassembly of the clusters leads to a ~60-70 nm shift in the LSPR peak and two to 44-fold decrease in intensity depending on the particle size. However, single-nanostructure spectroscopy[24,25] and imaging usually require advanced instrumentations such as sensitive charge-coupled detector camera (e.g. electron-multiplying or liquid nitrogen cooled CCD), tunable filters,[26] spectrometers or spectrographs, and high-intensity light source;[27] the analysis can also be complex with the need of mathematical algorithms for fitting. The infrastructure required for working with single-nanostructure plasmonic sensors may not be readily accessible to others and hence most works demonstrate proof-of-concept study of biomolecular interactions. Given that

plasmon coupling can be extended by incorporating more nanoparticles, there exists an opportunity to enhance the signal-to-noise ratio and ease of imaging process through chip design rather than instrumentation improvement. In this chapter, we investigate the fabrication and sensing performance of multilayer core-satellite structures. Enhancing the detection signal would be attractive for quantitative analysis and may facilitate the practical integration of these sensors with portable and consumer-grade instruments.[28] Moreover, we demonstrate the use of a structural-switching aptamer[29] (and in general oligonucleotides) as linkers for the disassembly-based detection scheme. The methodology can be readily adapted for different targets and presents a significant development of a chip-based nanoparticle sensing platform towards broader applications.

2.3 Results and Discussion

2.3.1 Fabrication of Multilayer Core-Satellite Assemblies and Detection via Disassembly Process

Scheme 2.1a illustrates a layer-by-layer assembly process to fabricate the multilayer core-satellite structures. First, core AuNPs of 60 nm were immobilized on a (3-aminopropyl) triethoxysilane (APTMS)-silanized glass substrate and functionalized with thiolated DNA Seq 1. The substrate was then passivated with methoxy (polyethylene)glycol succinimidyl valerate (mPEG-SVA) prior to the layer buildup process to minimize the non-specific binding of satellite AuNPs. The colloidal 30-nm satellite AuNPs functionalized with sequence 2, and subsequently AuNPs functionalized with Seq 1, were incubated alternatively with the substrate sample to form layers of satellite nanoparticles on top of the core. This process is repeated up to 5 times. For proof-of-concept, we employed ATP-aptamer[30] as Seq 2 and a short partial complement (9 bases) as Seq 1. Detection is based on the disassembly of the nanoparticles that results from the structural changes of the aptamer upon binding to ATP (Scheme 2.1b). Initially there are nine base pairs

hybridized between the ATP-aptamer (seq. 2) and the partially complementary Seq 1. In the presence of ATP, the aptamer undergoes a conformational change and folds to yield only four complementary base pairs between Seq 1 and Seq 2.[7] The shortened complementary duplex is unstable at low salt concentration, and therefore the DNA linkers dehybridize leading to the disassembly of the nanoparticle aggregates.

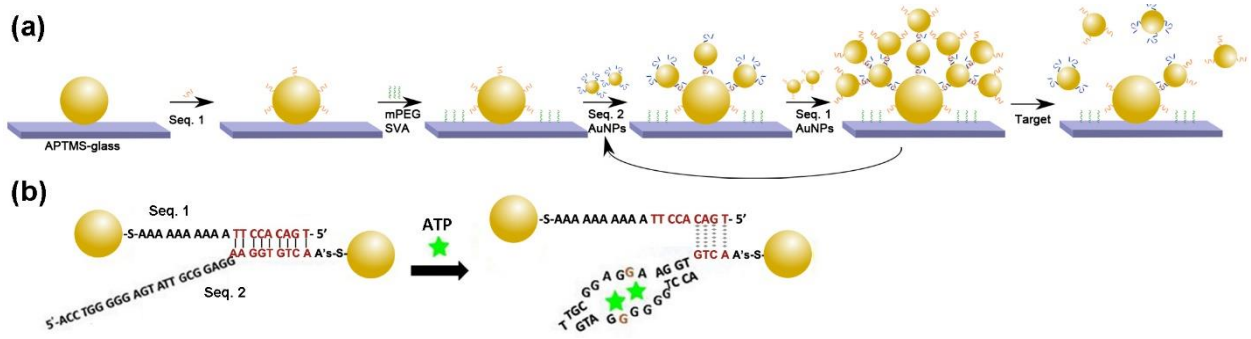

Scheme 2.1. Layer-by-layer assembly process of core-satellite nanostructures and the disassembly upon target binding (a); DNA sequences employed to obtain disassembly from the structural-switching ATP-aptamer (b).

2.3.2 Darkfield Images and Spectroscopy

We monitored the assembly process by darkfield imaging and spectroscopy. Figure 2.1a shows the darkfield scattering spectra of an individual assembly during layer buildup: the LSPR peak red shifts from ~562 nm to ~605 nm and increases in intensity exponentially upon assembling up to 5 layers of satellite particles. The darkfield images (Fig. 2.1c) evolved from dimly green scattering single-core AuNPs (60 nm) to bright yellow scatterers upon layer buildup. We measured 10 assemblies spectroscopically and in parallel obtained their scattering intensity by analyzing the grayscale darkfield images. The darkfield images show intensity increases by factors of 1.8, 6.9, 12, 29 and 39 for 1, 2, 3, 4 and 5 layers of satellite nanoparticles, respectively, in comparison with the core AuNP. Figure 2.1b shows the qualitative agreement between spectral and image analyses. The ability to quantitatively analyze the scattering intensity via images allows us to simultaneously

analyze hundreds and thousands of assemblies all in one field of view, thereby significantly reducing the time and labor required for data acquisition and analysis. Figure 2.1d shows the distribution of the scattering intensity of 239 assemblies with increasing layers of satellite nanoparticles. Variations in the sizes, shapes and numbers of satellite nanoparticles lead to

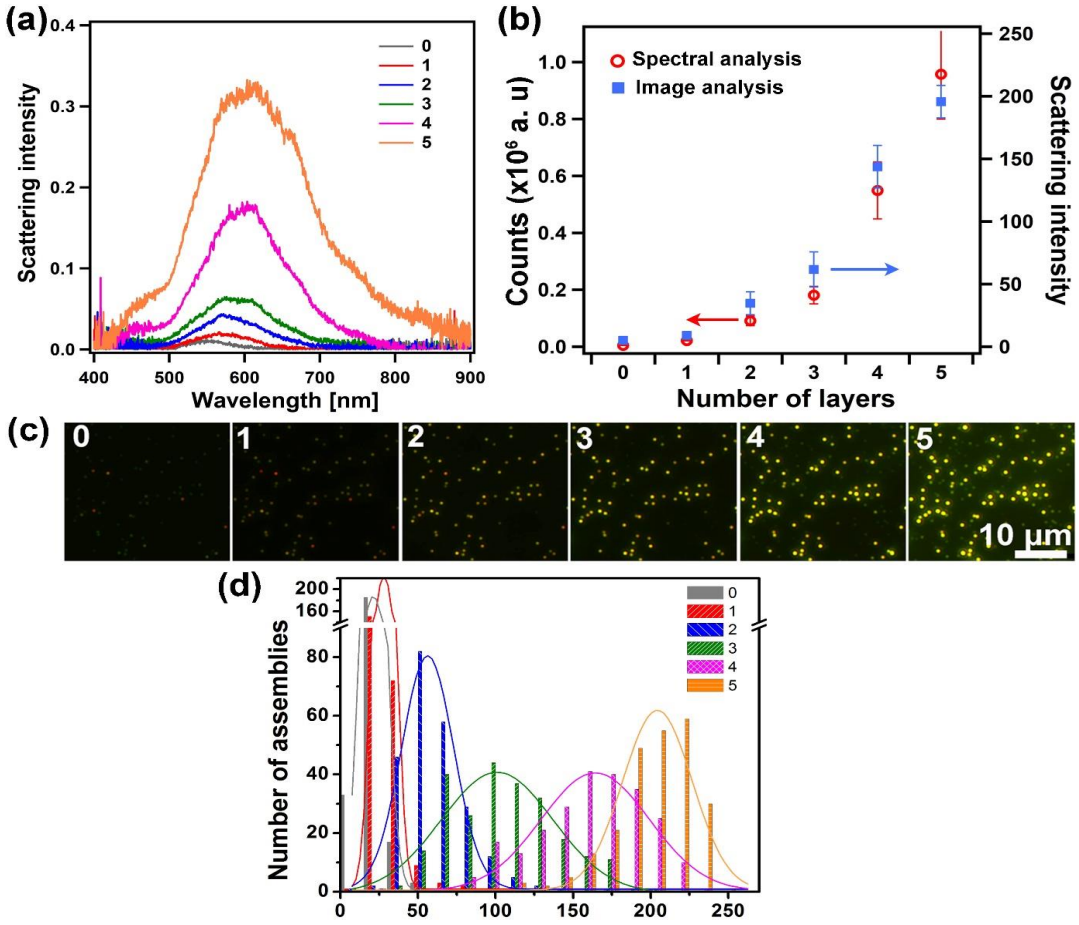

Figure 2.1. Optical characterization of the core-satellite structures during assembly process by darkfield imaging and single-nanostructure spectroscopy. (a) Scattering spectra of a single assembly with increasing number of layers of satellite nanoparticles: grey – 0 (60-nm core AuNP), red – 1, blue – 2, green – 3, magenta – 4 and orange – 5. (b) Scattering intensity of 10 assemblies obtained by integrating the area under the scattering spectra vs averaging the intensity of pixels in darkfield images. Error bars are two times standard deviations for the ten assemblies. (c) Darkfield images of the assembly process with 0, 1, 2, 3, 4 and 5 layers of satellite nanoparticles and (d) the distribution of the scattering intensity of 239 assemblies analyzed from the images.

differences in plasmon coupling and a normal distribution of scattering intensity for each assembly step.

We characterized the morphology of the structures by correlated imaging between electron and darkfield microscopy (Fig. 2.2a and b) for 208 assemblies. Figure 2.2c-k show representative SEM images of the structures with 1, 2 and 3 layers of satellite nanoparticles; the number of satellite nanoparticles increases from 6±1, to 18±3 and 34±7 with each assembly process. The

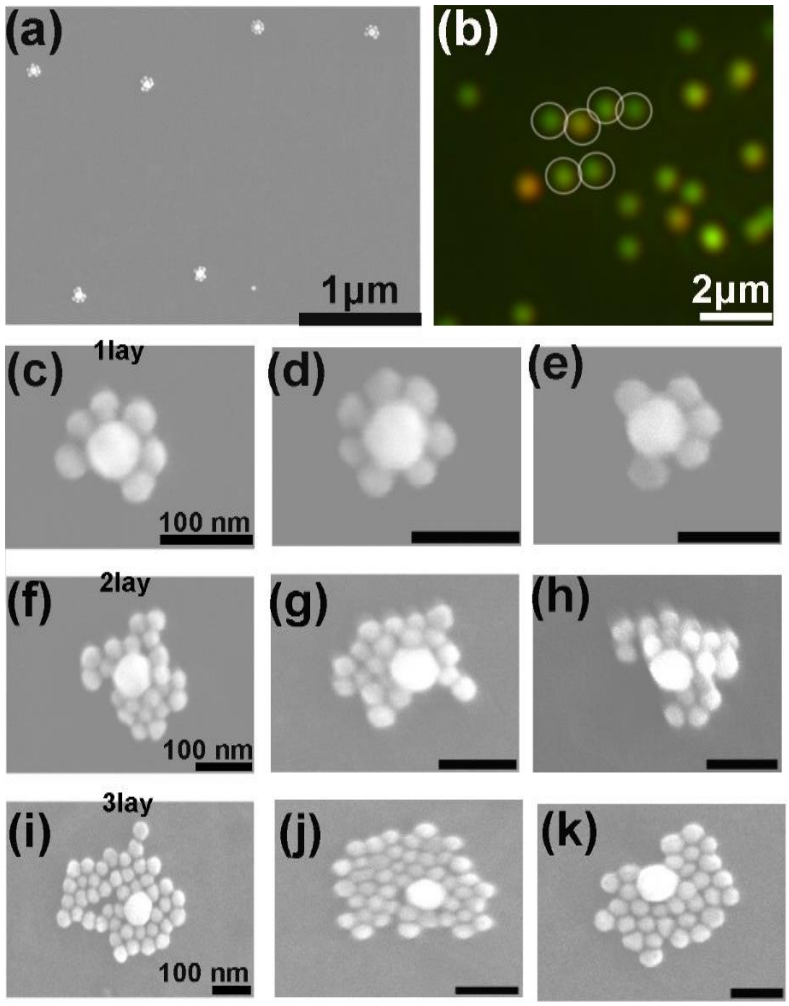

Figure 2.2. Scanning electron microscopy (a) and darkfield (b) correlated imaging of an area of interest. The assemblies circled in (b) are shown in (a). Representative SEM images of assemblies with 1 (c,d,e), 2 (f,g,h) and 3 (i,j,k) layers of satellite nanoparticles.

structures in SEM images appear two-dimensional and collapsed on the substrate because of the capillary force and drying effect during sample preparation.[31–34]

Figure 2.3a shows the scattering intensity of the discrete clusters with respect to the number of satellite nanoparticles. A linear trend is observed, which is further supported by finite-difference time-domain (FDTD) simulation. Figure 2.3b shows the simulated scattering spectra of core-satellite assemblies with incremental numbers of particles randomly placed around the core. The evolution of the experimental scattering spectra is reproduced in simulations by setting the interparticle distance (of any closest neighboring particles) to be 10 nm – the approximate length of the DNA linker. The agreement suggests that the structure of the assembly obtained experimentally has similar three-dimensional arrangement as those employed in the simulation where variations in the position of the particles do not yield changes to the spectra; note that simulated spectra for the flattened two-dimensional structures observed in SEM do not agree well

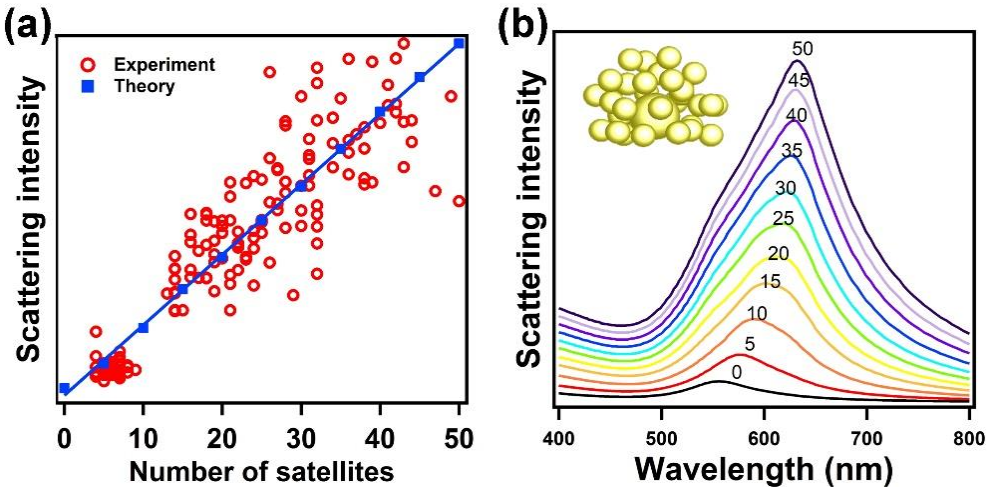

Figure 2.3. (a) Correlation of the scattering intensity of 208 assemblies to the number of satellite nanoparticles as determined by SEM. (b) FDTD simulated scattering spectra of assemblies with 0 to 50 satellite nanoparticles. The inset shows the core-satellite structure with 30 satellite nanoparticles used in the simulation.

with experiment due to less plasmon coupling of core and satellite NPs. The direct correlation between scattering intensity and the number of particles facilitates quantitative analysis for sensing applications.

2.3.3 Sensing ATP via Disassembly

Next we examined the detection of the model target ATP. The disassembly occurs rapidly upon exposure to ATP and reaches equilibrium within 20 seconds (Fig. 2.4). Figure 2.5a shows the darkfield images of 5-layer core-satellite assemblies with increasing concentrations of ATP. We established the calibration curves for samples with the different number of layers of satellite nanoparticles (Fig. 2.5b). Larger assemblies enhance the initial scattering signal from 59±2 counts for 1 layer to 159±8 counts for 5 layers of satellite nanoparticles. On the other hand, the scattering intensity at the final equilibrium concentration of 50 mM ATP also increases with increasing layers of satellite nanoparticles. As the assemblies become large (i.e. with tens of satellite nanoparticles coupled to the core), interactions with the substrate inevitably lead to some non-specific attachment of particles that prevents complete dissociation. We find that passivation of the

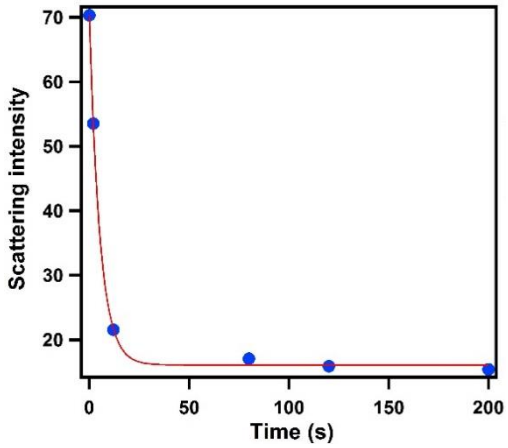

Figure 2.4. Monitoring the temporal scattering intensity of 3-layer core-satellite assemblies upon the addition of 2 mM of ATP.

substrate, functionalization of the nanoparticles with Bis(p-sulfonatophenyl)phenyl phosphine, and elimination of capillary forces during the assembly process are critical for achieving effective disassembly. We fitted the dose-dependence curves to the Langmuir model, which assumes: (i) the two binding sites on the aptamer are equal; (ii) each site can bind to only one solute molecule; (iii) there is no interaction between solutes to alter their adsorption behavior; (iv) binding of the target is a dynamically reversible process; and (v) the disassembly process occurs through

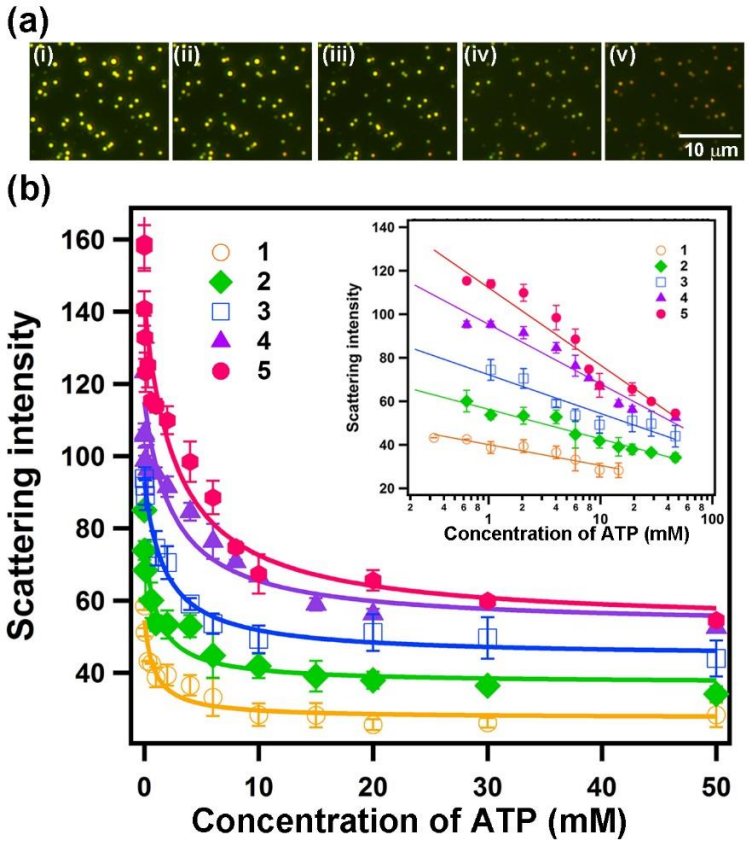

Figure 2.5. Monitoring the disassembly process by darkfield microscopy for sensing ATP. (a) Darkfield images of 5-layer core-satellite assemblies in: (i) 0, (ii) 0.01 mM, (iii) 0.3 mM, (iv) 10 mM and (v) 50 mM of ATP in buffer. (b) Calibration curves for assemblies of 1, 2, 3, 4 and 5 layers of satellite nanoparticles with varying concentrations of ATP. Error bars are standard deviations of independent experiments and Langmuir fits are shown in solid lines. Inset shows the logarithmic plot of the concentration-dependence curves in the working range.

sequential layers of satellite NPs. The fits yielded apparent dissociation constants (K_d) where the K_d increases from 0.88 mM to 1.02, 1.75, 2.55 and 2.83 mM with an increasing number of layers of satellite nanoparticles (Table 2.1). The apparent K_d increases because larger assemblies have more strands of DNA aptamer and would require more binding events to lead to disassembly. The finding demonstrates the tunability of the sensing performance by controlling the cluster size rather than tuning the biological linker. While the ATP aptamer has been found to contain two binding sites,[30,36] the dehybridization of the DNA duplex linker arises from the conformational change that likely occurs only after both ATP molecules bind. Hence a pseudo single-binding Langmuir model was employed. The K_d obtained from the core-satellite assemblies is higher than the free single-stranded aptamer (~10-16 μM), but is in line with previous reports based on fluorescent molecular-beacon designs,[29,37] nanoflares[38] and colloidal gold nanoparticles utilizing the structural-switching aptamer.[7] The lower affinity may arise from the duplex design in which partial hybridization between the sequences may hinder ATP binding to the aptamer.

Because the noise, or standard deviation of the signal, remains relatively the same while the initial scattering intensity is enhanced for larger assemblies, we achieved a lower limit of detection for assemblies with 4-5 layers of satellite nanoparticles compared to that with 1 layer

Table 2.1. Fitted parameters of calibration curves in Fig. 4 to equation $= y_0 + a\frac{k_a x}{(1+k_a x)}$. The detection limit is calculated based on the signal of I_0 - 3s where s is the standard deviation of the image intensity between replicates of experiments, and the calibration fits.

Layers of satellite NP	Fitted parameters			Experimental error in signal intensity (s)	Detection limit (mM)
	K_a	y_0	a		
1	1.14 ± 0.42	54.4 ± 2.3	-27.0 ± 2.5	2.2	0.33
2	0.98 ± 0.36	77.2 ± 2.9	-40.0 ± 3.4	3.5	0.36
3	0.56 ± 0.095	92.9 ± 1.4	-48.4 ± 1.9	3.9	0.32
4	0.39 ± 0.19	115.0 ± 3.9	-62.2 ± 7.1	2.2	0.12
5	0.35 ± 0.13	141.5 ± 4.2	-88.41 ± 7.8	3.9	0.16

(~0.15 mM vs 0.33 mM, respectively. See Table 2.1). Larger assemblies also extend the range of detection to >10 mM, where the signal for 1-layer core-satellite structure already plateaus. When the dose-dependence curve in the dynamic range is approximated by an exponential relation, Fig. 2.5 inset qualitatively shows that the sensitivity (i.e. magnitude of the slope of scattering intensity vs logarithmic concentration) increases with increasing layers of satellite nanoparticles. For practical applications, assemblies with 3-4 layers of satellite nanoparticles provide a balance between enhanced sensing performance, effective disassembly and facile sensor fabrication.

2.3.4 Selectivity and Sensing in Complex Media

The selectivity of the aptamer towards ATP is retained in the nanoparticle assemblies. Figure 2.6a shows that exposure to guanosine 5'-triphosphate (GTP) and cytidine 5'-triphosphate (CTP) yields no disassembly and negligible change to the scattering intensity. Unexpectedly, the nanoparticle assemblies show negligible detection signal for adenosine monophosphate (AMP)

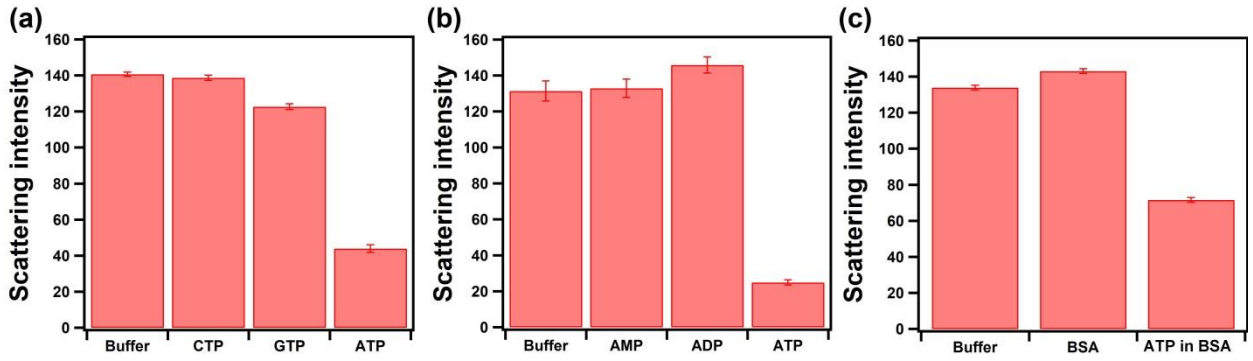

Figure 2.6. The selectivity of 3-layer core-satellite assemblies to ATP vs CTP and GTP (a) and ATP vs AMP and ADP (b). Scattering intensity of nanoclusters changed negligibly upon on addition of 2 mM of CTP and GTP, but significantly decreased upon on the addition of 2 mM of ATP (a). Likewise no decrease in scattering intensity was observed upon exposure to AMP and ADP (up to 50 mM); the assemblies subsequently disassembled completely upon exposure to 15 mM ATP (b). Detection of ATP in Bovine serum albumin (c). Sample was incubated with 10 mg/mL BSA solution and then with 10 mM ATP in 10 mg/mL BSA in sensing buffer; a significant decrease in scattering intensity was observed for ATP in BSA solution.

and adenosine diphosphate (ADP) (Fig. 2.6b) even though the free aptamer binds to all adenine-containing compounds. This selectivity is exclusive for substrate-anchored assemblies. We hypothesized that the selectivity may arise from the high negative charge of ATP that further destabilizes the duplex DNA linker upon structural-switching of the aptamer. The sensing motif based on the disassembly of nanoparticles on the substrate is additionally advantageous for detection in complex media. Sensors based on spectral shifts from refractive index changes are often challenged by false positives due to non-specific binding, which either masks or reduces the signal from target binding. [12,13] In contrast, non-specific binding of proteins or molecules to the substrate-anchored multi-nanoparticle assembly produces negligible change to the scattering intensity (<10%); competing signals from the interferences are almost eliminated. We tested the core-satellite assemblies for the detection of ATP in protein solution (10 mg/mL of bovine serum albumin (BSA)). Figure 2.6c shows the scattering intensity of 3-layer core-satellite assemblies exposed to BSA solution with and without ATP. The presence of ATP in the protein media still results in a large detection signal, however, the magnitude of the decrease in the scattering intensity in BSA is smaller than in buffer (62 vs 96 counts). The difference could arise from the binding of ATP to BSA[39] that effectively lowered the concentration of the target.

2.3.5 Sensing ATP Directly from Lysed Cells

We adapted the layer-by-layer assembly fabrication method to an elastomeric substrate (PDMS) to test the feasibility of detecting ATP from lysed ovarian cancer cells (HEY). The elastomeric substrate allows us to place the nanoparticle assemblies in close proximity, if not in direct contact, with cultured cells adhered to a coverslip in a minimized volume (10 μL) of lysis buffer. Figure 2.7a shows the sandwich approach that involves no purification, separation, or extraction of the target. The cells are lysed upon 30-minute of incubation with 0.02% Triton X-

100. Figure 2.7b and c show the darkfield images of ATP-aptamer linked vs non-targeting DNA-linked (control) nanoparticle assemblies before and after incubation with cells in the lysis buffer. The control sample shows negligible change while the ATP-aptamer linked clusters undergo significant disassembly that results in a decrease in scattering intensity. Replicates of the experiment confirm that other cellular species do not affect the stability of the nanoparticle assemblies (Fig. 2.7d) and that the ATP from the lysed cells can be effectively detected with the supported-nanoparticle assemblies in this simple and fast assay (Fig. 2.7e). The nanoparticle assemblies can be readily adapted to target other species (e.g. nucleic acids, proteins, small

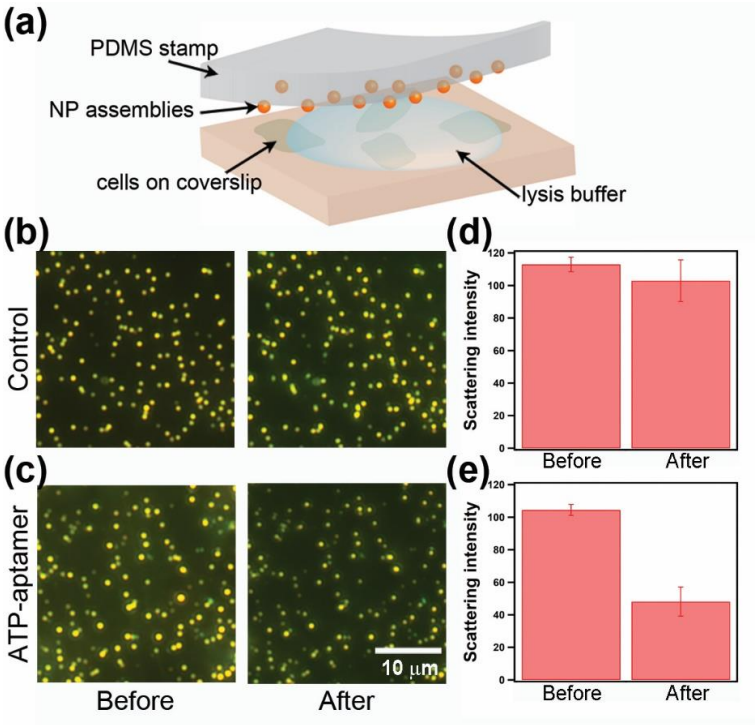

Figure 2.7. Direct detection of ATP from cell lysate. (a) Schematic of the sandwich experimental setup. Darkfield images of control (b) and ATP-aptamer linked assemblies (c) before and after exposure to lysed cells. Scattering intensity from triplicate samples of the control (d) and ATP-aptamer linked (e) assemblies before and after exposure to lysed cells. Non-ATP-targeting assemblies show negligible change in comparison to ATP-aptamer linked assemblies that show a decrease in scattering intensity upon incubating with cells in lysis buffer for 30 minutes.

molecules) by changing the DNA linker, and further optimization of the conditions in the sandwich approach may enable the detection and mapping of concentrations in microenvironments, such as targets secreted or expunged from individual cells. Notably, there are three distinct differences in our approach compared to previous work: (i) the fabrication of the assemblies requires no purification; (ii) the substrates or surfaces containing specimens of interest are prepared separately; (iii) enhanced optical signal facilitates image acquisition, reduces signal-to-noise ratio and enables quantitative analysis. These advantages augment the versatility and adaptability of single-nanostructure-based sensors for applications beyond research in biomolecular interaction. By reducing the instrumentation required, such that portable smartphone cameras may be used, combined with image analysis that may be performed remotely as in cloud-enabled microscopy,[40,41] our work presents new opportunities for the development of portable chip-based plasmonic sensors and app-based on-site field sensing technology.[42]

2.4 Conclusion

In summary, we developed multilayer plasmonic core-satellite assemblies for tunable quantitative sensing. Through an iterative hybridization process of DNA-functionalized nanoparticles, the assemblies on the substrate can be tuned to contain a few to tens of satellite nanoparticles, thereby controlling plasmon hybridization. Enhanced light scattering of the multi-nanoparticle assemblies enables the analysis of hundreds of structures in parallel using darkfield imaging. The proof-of-concept detection of ATP based on changes in the scattering intensity upon disassembly show the ability to perform in complex media and with minimal sample volume. This sensing platform may be adapted for a variety of targets, facilitate high-density chip-based multiplexing, and be of value not only in biomedical research, but in areas such as food safety, environmental monitoring, and point-of-care diagnostics.

2.5 Methods

Reagents and Materials

Colloidal gold nanoparticle solutions were purchased from BBI Solutions. Glass coverslips (25 mm x 25 mm) were purchased from VWR. Illustra NAP-5 columns were purchased from GE Healthcare Life Sciences, and SecureSeal hybridization chambers (8-9 mm in diameter x 0.9 mm depth) were purchased from Grace Bio-Labs. Anhydrous ethanol and 2-propanol were purchased from Commercial Alcohol, and water used for all experiments were purified using a Millipore system. Methoxy poly(ethyleneglycol)succinimidyl valerate (mPEG-SVA, M_W = 5000 g/mol) was obtained from Layson Bio Inc. Triton X-100 was obtained from BioShop Canada Inc. Polydimethylsiloxane (PDMS – Sylgard 184) was purchased from Dow Corning Corporation. All other chemicals were purchased from Sigma Aldrich. Oligonucleotides were obtained from Integrated DNA Technologies. Thiolated DNA sequences were purified by HPLC.

DNA sequences

ATP-targeting assemblies:

Seq 1: 5'- T GAC ACC TTA_{10}-$(CH_2)_3$- SH- 3'

Seq 2: 5'- ACC TGG GGG AGT ATT GCG GAG GAA GGT GTC ACA A_{10}-$(CH_2)_3$- SH- 3'

Control assemblies:

Seq 3: 5'-SH-$(CH_2)_6$-TCT CAA CTC GTA CGC ATG ATT GTT TTC AAT CAT GCG CGA AAG ATC CTG AAT GCG -3'

Seq 4: 5'-SH-$(CH_2)_6$-A_{10} CG CAT TCA GGAT -3'

Preparation of DNA-Functionalized Colloidal Gold Nanoparticles

A stock solution of 30 nm gold nanoparticles was first ligand-exchanged with Bis(p-sulfonatophenyl)phenyl phosphine (BSPP) before DNA functionalization. A volume of 2 mL of

30nm gold nanoparticles was stirred with 2mg of BSPP for 8 hours. The solution was then washed twice with water by centrifugation at 5000 rpm for 15 minutes, re-suspended in 5 nM of BSPP and stored at 4ºC.

The thiolated DNA sequences were first treated with Tris(2-carboxyethyl)phosphine hydrochloride (TCEP, 100 mM, 50x excess) in acetate buffer (50 mM, pH=4.7) for 1 hour to reduce the disulfide bonds. The solution was then purified by NAP-5 column. A volume of 10-20 μL of purified oligonucleotides (with ~ 1 OD at 260 nm) was mixed with 300 μL of BSPP-capped AuNP at room temperature for 16 h. The solution was then adjusted to contain 0.01 M phosphate buffer (1x PB, pH=7.4) and 0.01 % SDS followed by the standard salt aging procedure.[43] The concentration of NaCl was raised to 0.3 M with increments of 0.05 M NaCl while 0.01 M PB and 0.01% SDS were kept constant. After each addition, the solution was vortexed and sonicated for a few seconds, and incubated for ~1 hour in a 30 ºC water bath. The solution was incubated overnight and then washed by centrifuging at 12,000 rpm for 10 minutes and re-dispersing in 300 μL of 0.01% SDS three times. The DNA-functionalized gold nanoparticles were stored in a buffer containing 0.01 M PB, 0.05 M NaCl, 0.01% SDS and 0.01% azide at 4ºC.

Fabrication of Assemblies on Substrate

Silanized glass coverslips were prepared by plasma cleaning (Harrick's PDC-32G) the substrates for 20 minutes, followed by immersing in 50 mL of 1.0 % (3-aminopropyl) triethoxysilane (APTMS) in anhydrous ethanol for 2 hours. The APTMS-silanized coverslips were rinsed with 2-propanol, dried, and heated on a hot plate at ~80ºC for a few hours under the flow of nitrogen and overnight without nitrogen. A volume of 10 μL of 60-nm gold nanoparticle solution was placed on the substrate for 2 minutes. The substrate with core AuNPs was then washed with Milli-Q water and dried.

Volumes of 10 μL of 0.01 M PB, 1 M NaCl , 0.1% SDS buffer and 10 μL of 10 μM Seq 1 were added to the substrate containing core AuNPs. The solution was mixed gently using a pipette tip. The substrate was then placed in a water-saturated container for 2 hours to allow the thiolated DNA to attach to the core AuNPs. The sample was rinsed with MilliQ-water and dried with nitrogen. The excess amino groups on the glass substrate were passivated with 5 mM of mPEG-SVA in 0.1 M bicarbonate buffer (pH = 8.2). After passivation for at least 2.5 hours, the sample was washed with MilliQ-water and dried with nitrogen. The substrate containing Seq 1-functionalized core AuNPs was incubated in a phosphate buffer of 0.01 M and 0.3M NaCl in a SecureSeal chamber until layer assembly.

To assemble the first layer of satellite AuNPs on the core, a volume of 20 μL of ATP-aptamer (Seq 2) functionalized AuNPs (30 nm, in 0.01 M PB, 0.3 M NaCl and 0.01 % SDS) was incubated with core AuNPs on the substrate for 1 hour. The solution was then removed and the sample was washed at least 3 times with 0.01 M PB, 0.3 M NaCl solution. To assemble the second layer of satellite particles, Seq 1 DNA-functionalized AuNP was added to the existing core-satellite (1 layer) sample on the substrate for 1 hour. The solution was removed and the substrate was washed with buffer. The procedure was repeated with alternating DNA-functionalized AuNPs to build up the multilayer core-satellite structures. Each step of the assembly was monitored by dark-field microscopy. The clusters were incubated in the buffer of 0.01 M PB, 0.3 M NaCl for sensing experiments.

The aforementioned procedure was adapted to a polydimethylsiloxane stamp (Sylgard 184). The as-cured PDMS stamp was silanized using 2.0% ATPMs in 50 mL of anhydrous ethanol followed by the nanoparticle assembly process.

Sensing Experiments

Sensing experiments (unless otherwise noted) were carried out in a buffer of 0.01 M PB and 0.15 M NaCl. All samples were incubated at room temperature for at least one hour before the addition of analytes. Various volumes of a stock solution of 200 mM ATP in the sensing buffer was added to the sample to reach the specified concentration. Samples were incubated for a few minutes before dark-field images were collected. The same procedure was applied to solutions containing BSA, or GTP and CTP.

Cell Culture and Lysis Experiments

HEY cells (obtained from Dr. Theodore Brown, Mount Sinai Hospital, Toronto, ON, Canada) were cultured in Dulbecco's Modified Eagle Medium (DMEM) (GE HyClone, Logan, UT, USA) containing 10% fetal bovine serum. Cells were regularly tested to be free of mycoplasma contamination. Before the experiment, the cells were trypsinized and re-seeded on the tissue culture coverslips (Sarstedt, Newton, NC, USA). The cells were grown until the density reached ~75% confluence. A volume of 10 μL lysing buffer containing 0.01 M PB, 0.15 M NaCl and 0.02% Triton X-100 was placed on the PDMS substrate containing the nanoparticle assemblies. The coverslip with cells was rinsed with 1x PB, dried and immediately placed gently on the PDMS substrate. After 30 minutes of incubation, the coverslip was removed and the PDMS substrate was washed with buffer (1x PB, 0.15 M NaCl). The darkfield images of nanoparticle assemblies were captured before and after the sandwich assay.

Darkfield Imaging, Spectroscopy and Analysis

Nanostructures in the sample area (100 x 100 μm^2) were visualized under darkfield using a Nikon TE-2000U inverted microscope fitted with a darkfield condenser at 60x objective magnification with an optional 1.5x lens. The microscope was connected to a CCD camera (Jenoptik) and a portable spectrometer (USB2000, Ocean Optics) via an optical fiber (diameter

100 μm). Darkfield images were captured at 60x magnification with an integration time of 200 ms and scattering spectra were measured at 90x magnification using custom Labview software and a PInano positioning stage (P-545, Physik Instrumente).

The darkfield images were overlaid and converted to 8-bit JPEG grayscale that expresses the intensity on a scale from 0 to 255. The scattering intensities are extrapolated using Igor script files. For SEM-darkfield correlated analysis and scattering intensity distribution analysis, the coordinates of the center of the assemblies were identified manually or by using Localizer toolkit in Igor. The intensity of the surrounding 81 pixels for each assembly was then averaged. For sensing experiments, pixels beyond a threshold value (e.g. 50) of the initial assembly were identified; the intensity of these pixels were averaged for each image in the series and corrected by the background intensity. This method of image analysis was more rapid and required less computing power than the analysis of individual scatterers. The intensity has an arbitrary unit.

Morphological Characterization

The assemblies of 1, 2 and 3 layers of satellite nanoparticles were fabricated on indium tin oxide coated (ITO) substrate. The clusters were imaged by Quanta 3D electron microscope in the standard mode at 20.0 kV.

2.6 References

(1) Willets, K. A.; Van Duyne, R. P.; Duyne, R. P. Van. Localized Surface Plasmon Resonance Spectroscopy and Sensing. *Annu. Rev. Phys. Chem* **2007**, *58*, 267–297.

(2) Anker, J. N.; Hall, W. P.; Lyandres, O.; Shah, N. C.; Zhao, J.; Duyne, R. P. Van. Biosensing with Plasmonic Nanosensors. **2008**, *7*, 8–10.

(3) Mirkin, C. A.; Letsinger, R. L.; Mucic, R. C.; Storhoff, J. J. A DNA-Based Method for Rationally Assembling Nanoparticles into Macroscopic Materials. *Nature* **1996**, *382*, 607–609.

(4) Storhoff, J. J.; Elghanian, R.; Mucic, R. C.; Mirkin, C. A.; Letsinger, R. L. One-Pot Colorimetric Differentiation of Polynucleotides with Single Base Imperfections Using Gold Nanoparticle Probes. *J. Am. Chem. Soc.* **1998**, *120*, 1959–1964.

(5) Lee, J. S. S.; Han, M. S. S.; Mirkin, C. A. A. Colorimetric Detection of Mercuric Ion (Hg2+) in Aqueous Media Using DNA-Functionalized Gold Nanoparticles. *Angew. Chemie - Int. Ed.* **2007**, *46*, 4093–4096.

(6) Elghanian, R., James J. Storhoff, Robert C. Mucic, Robert L. Letsinger, C. A. M. Selective Colorimetric Detection of Polynucleotides Based on the Distance-Dependent Optical Properties of Gold Nanoparticles. *Science* **1997**, *277*, 1078–1081.

(7) Liu, J.; Lu, Y. Fast Colorimetric Sensing of Adenosine and Cocaine Based on a General Sensor Design Involving Aptamers and Nanoparticles. *Angew. Chemie Int. Ed.* **2006**, *45*, 90–94.

(8) Li, H.; Rothberg, L. Colorimetric Detection of DNA Sequences Based on Electrostatic Interactions with Unmodified Gold Nanoparticles. *Proc. Natl. Acad. Sci. U. S. A.* **2004**, *101*, 14036–14039.

(9) Xiao, R. P.; Wang, D. F.; Lin, Z. Y.; Qiu, B.; Liu, M. H.; Guo, L. H.; Chen, G. N. Disassembly of Gold Nanoparticle Dimers for Colorimetric Detection of Ochratoxin A. *Anal. Methods* **2015**, *7*, 842–845.

(10) Sonnichsen, C.; Reinhard, B. M.; Liphardt, J.; Alivisatos, A. P. A Molecular Ruler Based on Plasmon Coupling of Single Gold and Silver Nanoparticles. *Nat. Biotechnol.* **2005**, *23*, 1–14.

(11) Rajendran, P.; Kaufmann, S.; Vörös, J.; Zenobi-wong, M.; Demkó, L. Colloids and Surfaces B : Biointerfaces Femtomolar Oligonucleotide Detection by a One-Step Gold Nanoparticle-Based Assay. *Colloids Surfaces B Biointerfaces* **2015**, *135*, 193–200.

(12) Wang, Y.; MacLachlan, E.; Nguyen, B. K.; Fu, G.; Peng, C.; Chen, J. I. L. Direct Detection of MicroRNA Based on Plasmon Hybridization of Nanoparticle Dimers. *Analyst* **2015**, *140*, 1140–1148.

(13) Chen, J. I. L.; Chen, Y.; Ginger, D. S. Plasmonic Nanoparticle Dimers for Optical Sensing of DNA in Complex Media. *J. Am. Chem. Soc.* **2010**, *132*, 9600–9601.

(14) Lee, S. E.; Chen, Q.; Bhat, R.; Petkiewicz, S.; Smith, J. M.; Ferry, V. E.; Correia, A. L.; Alivisatos, A. P.; Bissell, M. J. Reversible Aptamer-Au Plasmon Rulers for Secreted Single Molecules. *Nano Lett.* **2015**, *15*, 4564–4570.

(15) Rong, G.; Wang, H.; Reinhard, B. M. Insights from a Nanoparticle Minuet: Two-Dimensional Membrane Profiling through Silver Plasmon Ruler Tracking. *Nano Lett.* **2010**, *10*, 230–238.

(16) Waldeisen, J. R. R.; Wang, T.; Ross, B. M. M.; Lee, L. P. P. Disassembly of a Core–Satellite Nanoassembled Substrate for Colorimetric Biomolecular Detection. *ACS Nano* **2011**, *5*, 5383–5389.

(17) Wang, K.; Shangguan, L.; Liu, Y.; Jiang, L.; Zhang, F.; Wei, Y.; Zhang, Y.; Qi, Z.; Wang,

K.; Liu, S. In Situ Detection and Imaging of Telomerase Activity in Cancer Cell Lines via Disassembly of Plasmonic Core–Satellites Nanostructured Probe. *Anal. Chem.* **2017**, *89*, 7262–7268.

(18) Jun, Y.; Sheikholeslami, S.; Hostetter, D. R.; Tajon, C.; Craik, C. S.; Alivisatos, A. P. Continuous Imaging of Plasmon Rulers in Live Cells Reveals Early-Stage Caspase-3 Activation at the Single-Molecule Level. *Proc. Natl. Acad. Sci. U. S. A.* **2009**, *106*, 17735–17740.

(19) Nordlander, P.; Oubre, C.; Prodan, E.; Li, K.; Stockman, M. I. Plasmon Hybridization in Nanoparticle Dimers. *Nano Lett.* **2004**, *4*, 899–903.

(20) Jain, P. K.; Huang, W.; El-sayed, M. a. On the Universal Scaling Behavior of the Distance Decay of Plasmon Coupling in Metal Nanoparticle Pairs : A Plasmon Ruler Equation. *Nano Lett.* **2007**, *7*, 2080–2088.

(21) Sebba, D. S.; Mock, J. J.; Smith, D. R.; LaBean, T. H.; Lazarides, A. A. Reconfigurable Core-Satellite Nanoassemblies as Molecularly-Driven Plasmonic Switches. *Nano Lett.* **2008**, *8*, 1803–1808.

(22) Ross, B. M.; Waldeisen, J. R.; Wang, T.; Lee, L. P. Strategies for Nanoplasmonic Core-Satellite Biomolecular Sensors: Theory-Based Design. *Appl. Phys. Lett.* **2009**, *95*, 193112.

(23) Sebba, D. S.; Labean, T. H.; Lazarides, A. A. Plasmon Coupling in Binary Metal Core-Satellite Assemblies. *Appl. Phys. B Lasers Opt.* **2008**, *93*, 69–78.

(24) Ringe, E.; Sharma, B.; Henry, A.-I.; Marks, L. D.; Van Duyne, R. P. Single Nanoparticle Plasmonics. *Phys. Chem. Chem. Phys.* **2013**, *15*, 4110–4129.

(25) Zijlstra, P.; Orrit, M. Single Metal Nanoparticles: Optical Detection, Spectroscopy and Applications. *Reports Prog. Phys.* **2011**, *74*, 106401.

(26) Bingham, J. M.; Willets, K. A.; Shah, N. C.; Andrews, D. Q.; Van Duyne, R. P. Localized Surface Plasmon Resonance Imaging: Simultaneous Single Nanoparticle Spectroscopy and Diffusional Dynamics. *J. Phys. Chem. C* **2009**, *113*, 16839–16842.

(27) Beuwer, M. A.; Prins, M. W. J.; Zijlstra, P. Stochastic Protein Interactions Monitored by Hundreds of Single-Molecule Plasmonic Biosensors. *Nano Lett.* **2015**, *15*, 3507–3511.

(28) Ludwig, S. K. J.; Zhu, H.; Phillips, S.; Shiledar, A.; Feng, S.; Tseng, D.; Van Ginkel, L. A.; Nielen, M. W. F.; Ozcan, A. Cellphone-Based Detection Platform for RbST Biomarker Analysis in Milk Extracts Using a Microsphere Fluorescence Immunoassay. *Anal. Bioanal. Chem.* **2014**, *406*, 6857–6866.

(29) Nutiu, R.; Li, Y. Structure-Switching Signaling Aptamers. *J. Am. Chem. Soc.* **2003**, *125*, 4771–4778.

(30) Huizenga, D. E.; Szostak, J. W. A DNA Aptamer That Binds Adenosine and ATP.

Biochemistry **1995**, *34*, 656–665.

(31) Liddle, J. A.; Cui, Y.; Alivisatos, P. Lithographically Directed Self-Assembly of Nanostructures. *J. Vac. Sci. Technol. B Microelectron. Nanom. Struct.* **2004**, *22*, 3409.

(32) Mastroianni, A. J.; Claridge, S. A.; Paul Alivisatos, A. Pyramidal and Chiral Groupings of Gold Nanocrystals Assembled Using DNA Scaffolds. *J. Am. Chem. Soc.* **2009**, *131*, 8455–8459.

(33) Gandra, N.; Abbas, A.; Tian, L.; Singamaneni, S. Plasmonic Planet-Satellite Analogues: Hierarchical Self-Assembly of Gold Nanostructures. *Nano Lett.* **2012**, *12*, 2645–2651.

(34) Fan, J. a; Wu, C.; Bao, K.; Bao, J.; Bardhan, R.; Halas, N. J.; Manoharan, V. N.; Nordlander, P.; Shvets, G.; Capasso, F. Self-Assembled Plasmonic Nanoparticle Clusters. *Science* **2010**, *328*, 1135–1138.

(35) Zhang, Z.; Oni, O.; Liu, J. New Insights into a Classic Aptamer: Binding Sites, Cooperativity and More Sensitive Adenosine Detection. *Nucleic Acids Res.* **2017**, *4567*, 2–10.

(36) Nutiu, R.; Li, Y. Structure-Switching Signaling Aptamers: Transducing Molecular Recognition into Fluorescence Signaling. *Chem. - A Eur. J.* **2004**, *10*, 1868–1876.

(37) Zheng, D.; Seferos, D. S.; Giljohann, D. A.; Patel, P. C.; Mirkin, C. A. Aptamer Nano-Flares for Molecular Detection in Living Cells. *Nano Lett.* **2009**, *9*, 3258–3261.

(38) Bauer, M.; Baumann, J.; Trommer, W. E. ATP Binding to Bovine Serum Albumin. *FEBS* **1992**, *313*, 288–290.

(39) Coskun, A. F.; Ozcan, A. Computational Imaging, Sensing and Diagnostics for Global Health Applications. *Curr. Opin. Biotechnol.* **2014**, *25*, 8–16.

(40) Bednarz, T.; Wang, D.; Arzhaeva, Y.; Lagerstrom, R.; Vallotton, P.; Burdett, N.; Khassapov, A.; Szul, P.; Chen, S.; Sun, C.; Domanski, L.; Thompson, D.; Gureyev, T.; Taylor, J. A. Cloud Based Toolbox for Image Analysis, Processing and Reconstruction Tasks. In *Signal and Image Analysis for Biomedical and Life Sciences*; Sun, C., Bednarz, T., Pham, T. D., Vallotton, P., Wang, D., Eds.; Springer International Publishing: Cham, 2015; pp 191–205.

(41) Yang, K.; Peretz-Soroka, H.; Liu, Y.; Lin, F. Novel Developments in Mobile Sensing Based on the Integration of Microfluidic Devices and Smartphones. *Lab Chip* **2016**, *16*, 943–958.

(42) Hurst, S. J.; Lytton-Jean, A. K. R.; Mirkin, C. A. Maximizing DNA Loading on a Range of Gold Nanoparticle Sizes. *Anal. Chem.* **2006**, *78*, 8313–8318.

(43) Meakin, P.; Ramanlal, P.; Sander, L. M.; Ball, R. C. Ballistic Deposition on Surfaces. *Phys. Rev. A* **1986**, *34*, 5091–5103.

Chapter 3 - Metabolic Mapping with Plasmonic Nanoparticle Assemblies

(This chapter is partly reproduced with permission from Le, N. H.; Ye, G.; Peng, C.; Chen, J. I. L. *Analyst*, **2020**, *145*, 2586-2594)

Cells were cultured by Gang Ye. All experiments presented in this chapter were carried out by Nguyen Le.

3.1 Abstract

Building on chapter 2, this chapter presents a rapid and simple methodology for the biomolecular analysis of single cells and microenvironment via the stick-and-peel plasmonic sensing platform. Substrate-bound assemblies of plasmonic gold nanoparticles linked by reconfigurable oligonucleotides undergo disassembly upon target binding. Changes in the light scattering intensity of thousands of discrete nanoparticle assemblies are extrapolated concomitantly to yield the mapping of local target concentrations. The methodology is completely free of labeling, purification and separation steps. We quantified the intracellular ATP levels for two ovarian cancer cell lines to elucidate the differences and cellular distribution, and demonstrate the potential of the stick-and-peel platform for mapping the microenvironment of 2D heterogeneous surfaces. The portable and economical analytical platform may broaden the affordability and applicability of single-cell based analyses and enable new opportunities in clinical care such as on-site molecular pathology.

3.2 Introduction

Molecular analyses on the single-cell level provides insight on cellular heterogeneity. These analyses elucidate the distribution of genomic, transcriptomic, proteomic and metabolomics levels in individual cells and enable the investigation of cell-to-cell variations that are unattainable

using common biochemical ensemble assays. The ability to probe cellular heterogeneity may lead to better disease diagnosis, prognosis, and treatment[1-5] by enabling the differentiation of subpopulation of disease-causing cells, the discovery of biochemical pathways and mechanisms, and the monitoring of the efficacy of the therapeutic intervention. Technologies for performing molecular and chemical analyses on the single-cell level include fluorescent- or mass-spectrometry-based techniques[6-11] coupled with flow cytometry[12-14] capillary electrophoresis[15-17] or optical microscopy,[18-20] in which the biomolecules of interest are labelled. They require complex instruments, centralized laboratory and personnel with expertise, and are often costly and time-consuming. Developing economical and portable analytical platforms for the rapid detection of biomolecules in single cells and microenvironments may broaden the affordability of such analyses and bridge the gap of fundamental biomedical research and clinical applications.

Sensing platforms based on single plasmonic nanostructures can detect targets near the vicinity of the particles, and thus have the potential to provide quantitative analysis of volume-limited samples such as single cells. Detection is achieved via a spectral shift or a change in the intensity of the scattered light, arisen from the reconfiguration of multi-nanoparticle assemblies.[21-26] Plasmonic nanostructures such as dimers[21,23,24,27-29] and clusters[30-33] have been developed for monitoring biomolecular interactions, including enzymatic activities[32,33] and binding of nucleic acids[34,35]; however, the direct quantification of intracellular biomolecules from individual cells has not been achieved.

Chapter 2 demonstrates the detection of metabolites such as ATP using aptamer-linked core-satellite gold nanoparticle (AuNP) assemblies.[22] ATP is the energy molecule and plays an important role in various processes that occur in living cells, such as muscle contraction, phosphorylation and active transport of ions, glucose, and amino acids. The level of ATP infers

the state of cellular metabolism, and is explored as an indicator for heightened chemoresistance of cancer cells[36] and tumorigenesis.[37-39] ATP is conventionally detected via chemiluminescence of the luciferase enzyme[40,41] - an ensemble assay that is affected by pH, oxygen, and the concentrations of the enzyme, cations, and the luciferin substrate. The analysis of ATP on the single-cell level has been achieved via a FRET technique using engineered proteins, such as donor (mseCFP) and acceptor (mVenus) fluorescent proteins linked by ATP-binding peptide subunit[42] or specially designed single fluorescence protein quencher.[43] The challenges with quantitation, protease sensitivity and photobleaching, combined with the need for protein engineering make the methodologies inaccessible to researchers in the broad scientific community.

In chapter 2, we established the core-satellite AuNP assemblies for the selective detection of ATP over ADP and AMP.[22] As with most other chip-based sensors, we detected the target in a bulk sample such as the lysate of an ensemble of cells. In this chapter, we derived the methodology for detecting at ultra-low volume down to a single cell and for mapping the molecular distribution in the microenvironment. We optimized the conditions for localizing the lysate of individual cells near the assemblies and established the method of extrapolating the local concentration based on the signal change of discrete nanoparticle sensors. We analysed the distribution of ATP levels of two ovarian cancer cell lines and showed that the average results corroborate with bulk measurements. In contrast to most single-cell technologies that aim to produce big data and complete "omics", our work presents alternative opportunities to enable cost-effective, user-friendly and rapid validation of biomolecules of interest with a high spatial resolution.

3.3 Results and Discussion

3.3.1 Principle of Detection at the Single-cell Level

The plasmonic nanostructures were fabricated via a layer-by-layer process, DNA-directed self-assembly of satellite AuNPs around core AuNPs, as described in chapter 2. We employed an ATP-aptamer and a partial complement as the linkers. The aptamer undergoes structural changes upon binding of ATP,[44-46] leading to the dehybridization of the linkers, the disassembly of the structure and the decrease in the scattering intensity (Scheme 3.1a). To investigate the concentration of ATP in cells, we sandwiched the nanoparticle sensors, which were anchored on an elastomeric substrate, with cells cultured on an adherent coverslip in the presence of microlitres of lysis buffer (Scheme 3.1b).

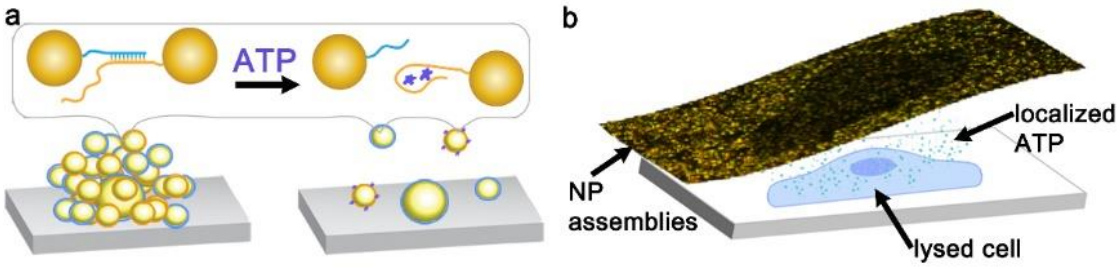

Scheme 3.1. (a) Gold nanoparticle assemblies supported on a flexible substrate disassemble in the presence of ATP due to conformational changes in the DNA-aptamer linker. (b) Stick-and-peel approach for the detection of ATP from a single cell achieved by localizing the expunged cell content near nanoparticle assemblies.

Initial work showed the entire sensing area decreased in intensity as the expunged ATP bind to the nanoparticle assemblies throughout the substrate. In the analysis of two ovarian cancer cell lines, SKOV3.ip1[47] and HEY,[48] the scattering intensity decreased more significantly for SKOV3.ip1 (Figure 3.1a vs b) than HEY (Figure 3.1c vs d) cells; however, no local intensity change corresponding to lysates from individual cells was achieved. Next we incorporated glycerol and optimized its concentration in the lysis buffer (Fig. 3.2) to increase the viscosity and decrease

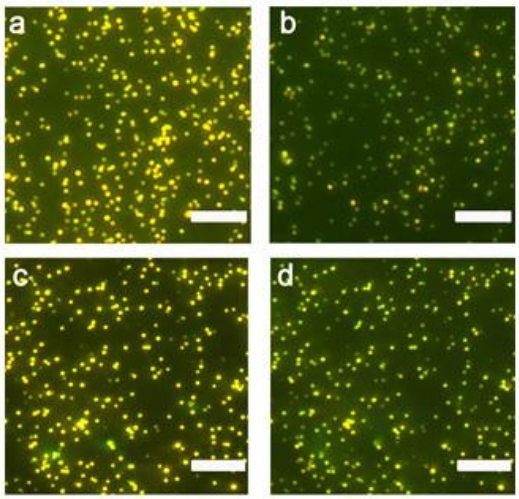

Figure 3.1. Darkfield images of AuNP assemblies for sensing ATP: before (a) and after (b) exposure to SKOV3.ip1 cells lysed without the addition of glycerol; before (c) and after (d) exposure to HEY cells lysed without the addition of glycerol. Samples were placed in contact with cells for 30 min. Scale bar: 10 μm.

the diffusion of biomolecules while maintaining the ability to disassemble the clusters. Figure 3.2e and f show the darkfield images of the nanoparticle assemblies before and after lysing using a buffer containing 20% glycerol. We observed an overlap of locations between the cell and of

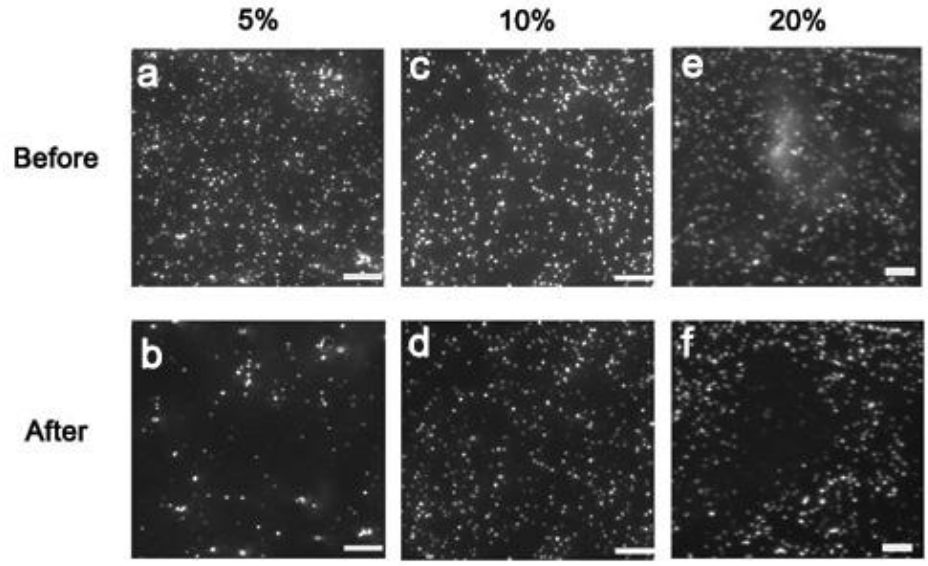

Figure 3.2. Gray-scale darkfield images of assemblies before (top) and after (bottom) sandwiching with cancer cells in lysis buffer containing various amounts of glycerol (5% , 10% and 20%). Scale bar: 10 μm.

decreased scattering intensity in the darkfield image. It suggests that the diffusion of small molecules, such as ATP, can in fact be confined to the vicinity of the cell and detected by nanoparticle assemblies within minutes.

3.3.2 Morphology of Nanoparticle Assemblies

We characterized the morphology of the nanostructures at locations overlapping and away from the cells. Figure 3.3a shows a low-magnification darkfield image and Figure 3.3b and c show representative SEM images of the nanostructures found at locations away from the cells and directly in contact with the cells, respectively. Figure 3.4 shows the correlated images between SEM and DF microscopy of nanostructures in a sensing area after contact with cells. The

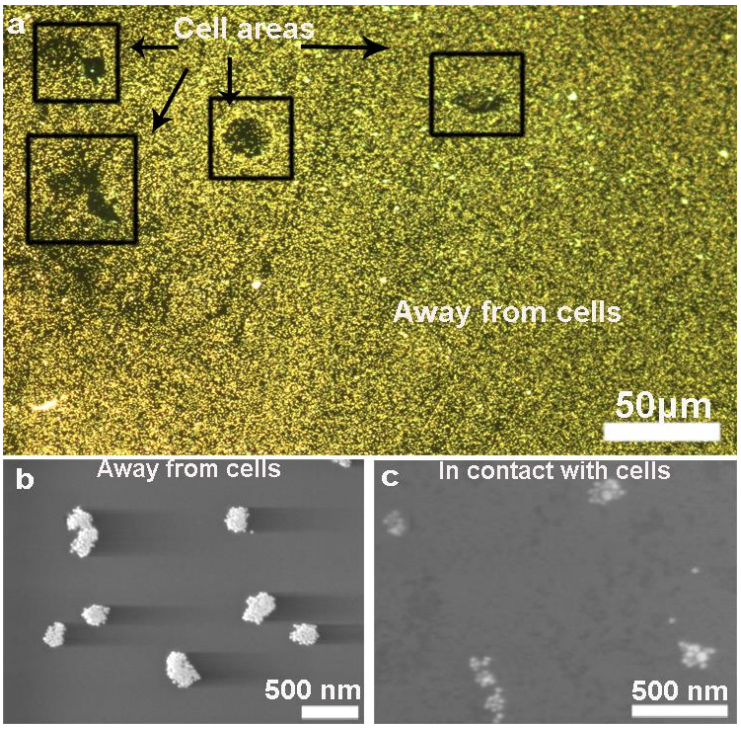

Figure 3.3. Characterization of assemblies after single-cell assay. (a) Darkfield image of assemblies with the locations overlapping cells outlined in black boxes. SEM images of nanostructures away from cells (b) vs directly in contact with cells (c).

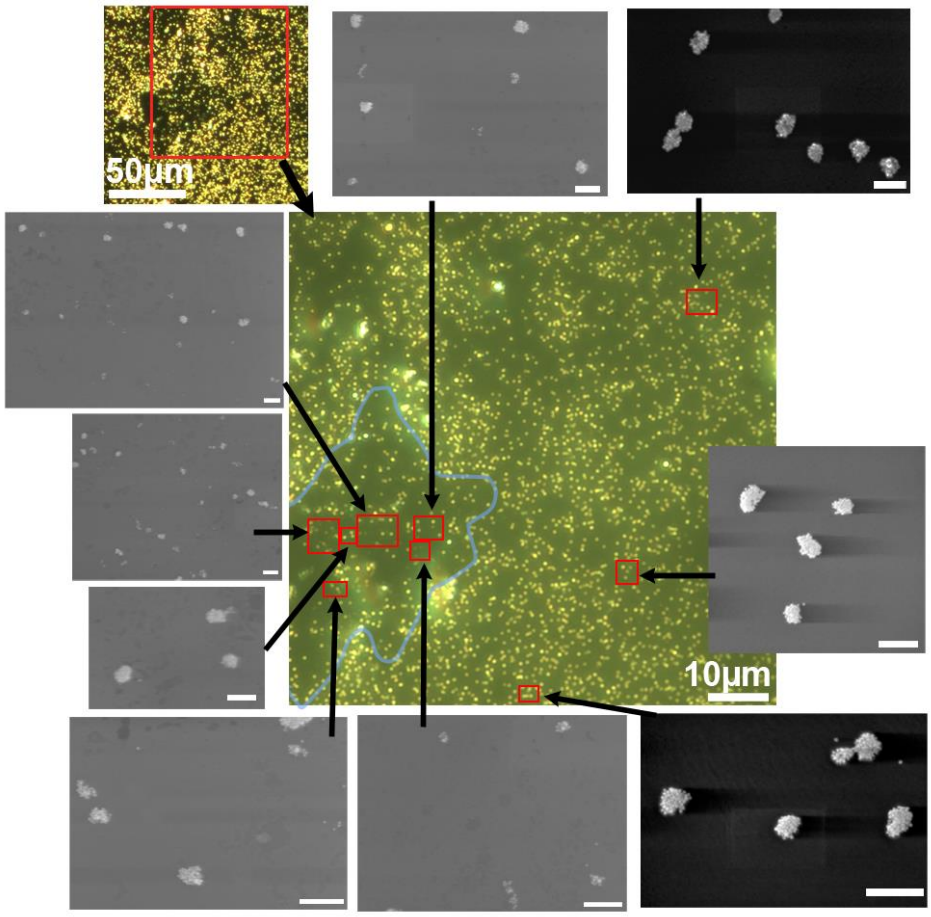

Figure 3.4. SEM-darkfield correlated imaging of sensing area in contact with a cell (outlined in blue). For correlation purpose, larger aggregates distinguishable in darkfield microscopy were selected. Correlated imaging of structures away from the cell are shown on the right. Scale bar for SEM images: 500 nm.

assemblies that are far away from the cells remain large with >40 particles in the core-satellite structure (Figure 3.3b). In contrast, the assemblies in contact with the cells show variations in size and structure (Figure 3.3c and 3.4). The disassembled structures exhibit a low number of satellite nanoparticles (ca. 6 to 20) while some dispersed single AuNP and a few larger aggregates were also observed in the cell area.

3.3.3 Detection Based on Individual Nanostructures

We exploited the scattering intensity from individual nanostructures for the quantification and mapping of ATP levels. As established in chapter 2, the scattering intensity obtained from the darkfield image was found to correlate with the intensity measured spectroscopically.[22] We can thus extrapolate the detection signal of hundreds of assemblies all in the field of view rapidly based on image processing and obtain the local concentration of ATP using a concentration-dependent

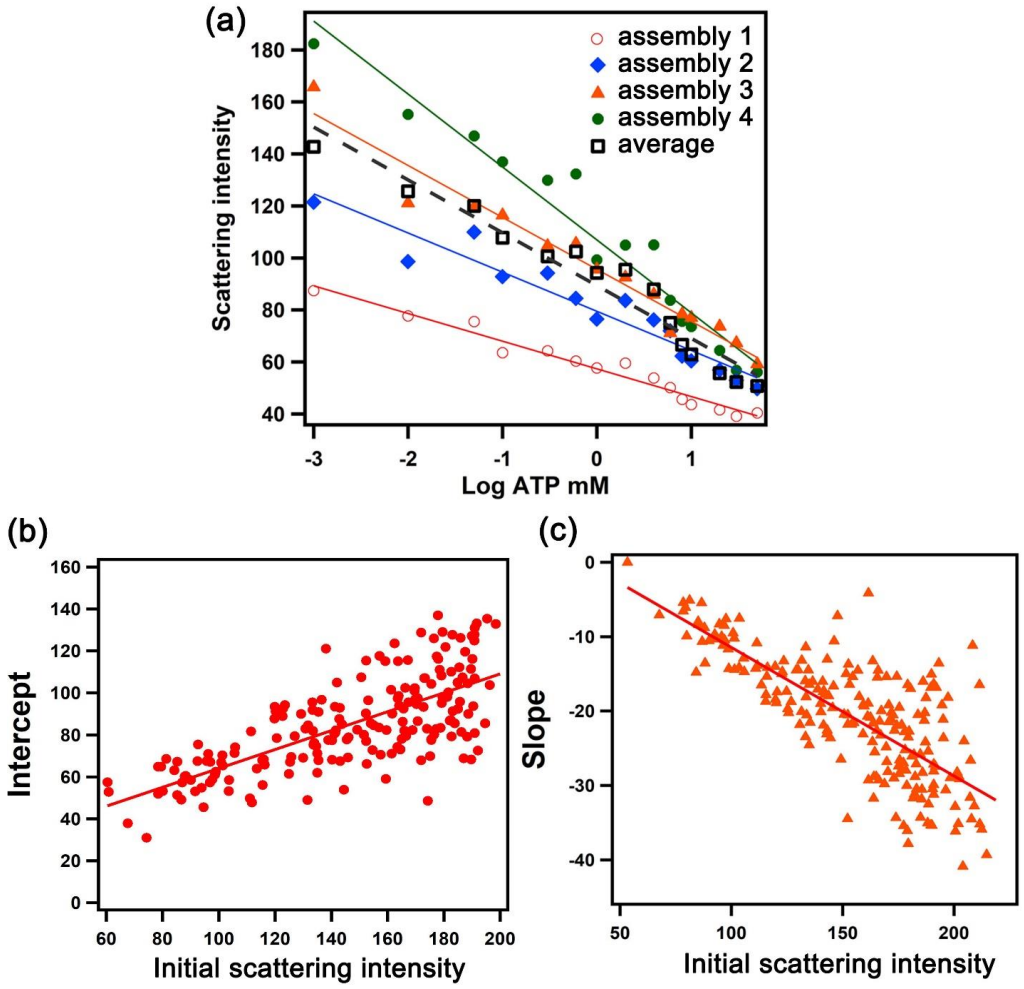

Figure 3.5. Deriving the calibration parameters for individual assembly. (a) The dependence of scattering intensity on the logarithmic concentration of ATP for selected 4 assemblies (red, blue, orange and green) and the average of 268 assemblies (black). The values of y-intercept (b) and slope (c) of calibration curves for 268 assemblies with respect to the initial scattering intensity, showing the linear dependency.

calibration curve. However, in single-nanostructure analysis, differences in the morphology of the nanoparticles yield variations in the optical properties. A darkfield microscopy image therefore consists of thousands of assemblies that are variable in scattering intensity which does not follow a universal calibration curve. Figure 3.5a shows the dependence of the scattering intensity on the logarithmic concentration of ATP for selected 4 assemblies, overlaid with the average values obtained from all of the assemblies captured in the entire image. A plasmonic AuNP assembly with a high initial scattering intensity shows a steeper dose-response compared to that with a low initial scattering intensity. The calibration curve has the general form I= mC+b where I is the scattering intensity, C is the log concentration of ATP in mM, m is the slope, and b is the y-intercept. Upon examining >200 assemblies, we found that the slope and y-intercept of the calibration curve in the working range linearly depend on the initial scattering intensity, as shown in Figure 3.5b and c. These parameters can be calculated based on the fits in Figure 3.5b and c, where $m = -0.18\ I_o + 6.82$ and $b = 0.50\ I_o + 13.7$. As a result, the calibration curve for each nanoparticle assembly can be determined based on its initial scattering intensity. The concentration-dependent relationships show that the sensing performance varies depending on the

Table 3.1. Fitted parameters of calibration curves ($I = mC + b$) of assemblies grouped by the initial scattering intensity. The detection limit and limit of quantification are calculated based on the signal of I_0 - 3s and I_0 - 10s where s is the standard deviation of the scattering intensity.

Initial scattering intensity	Fitted parameters		3s	LOD (mM)	LOQ (mM)
	m	b			
90-110	-10.8	63.0	4.6	0.054	0.06
110-130	-16.6	75.2	5.8	0.091	0.34
130-150	-17.9	79.2	5.2	0.135	1.25
150-170	-21.5	91.6	5.6	0.163	2.37
170-190	-26.2	103.5	6.3	0.189	3.88
190-210	-27.1	121.1	6.3	0.201	4.74

size of the aggregate, with detection limits of 0.05 - 0.20 mM for assemblies with scattering intensities ranging from 90 to 210 counts (Table 3.1). Moreover, the sensitivity of larger assemblies is greater than two-fold of the smaller assemblies, as indicated by the slope of the calibration response.

3.3.4 Quantification and Distribution of ATP Levels

We examined over a hundred cells using the nanoparticle assembly sensing platform. Figure 3.6 shows the darkfield microscopy images of a single SKOV3.ip1 and HEY cell on top of the nanoparticle assemblies (Fig. 3.6a and b), and gray-scale images of the sensors before (Fig. 3.6c and d) and after (Fig. 3.6e and f) being in contact with the corresponding lysed cells. The local decrease in the scattering intensity of the assemblies nearby the cells is significantly more

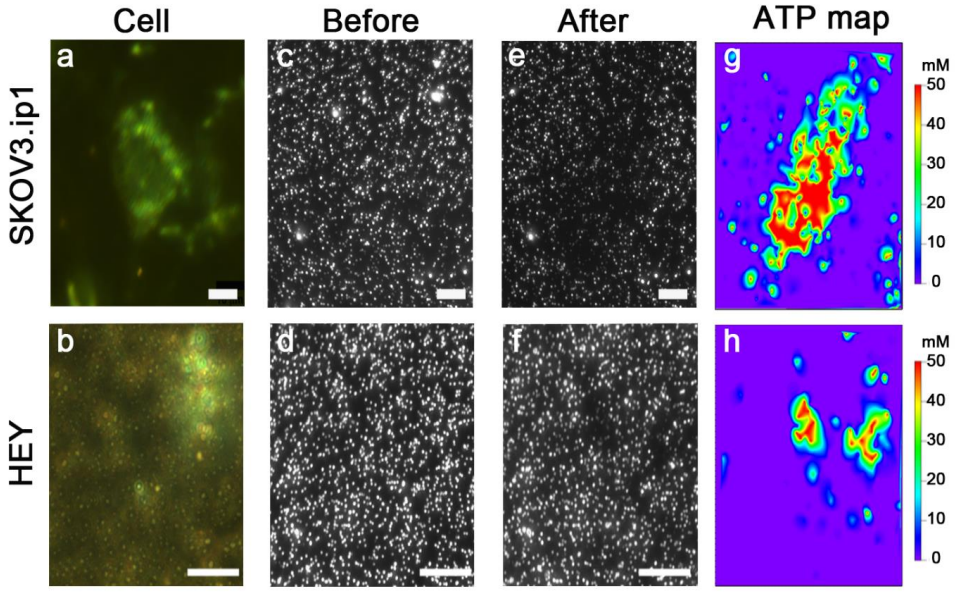

Figure 3.6. Detection of ATP from a single cell based on the scattering intensity of discrete AuNP assemblies. Darkfield images of single SKOV3.ip1 cell (a) and HEY cell (b) sandwiched on top of the nanoparticle assemblies. Grayscale darkfield images of the assemblies before (c, d) and after (e,f) in contact with the lysed cells for 30 min. Local concentration maps of ATP from single SKOV3.ip1 (g) and HEY (h) cell based on changes in the scattering intensity and calibration curve of individual assembly. Scale bar: 10 μm.

prominent for SKOV3.ip1 (Fig. 3.6e) in comparison to HEY (Fig. 3.6f). We analysed the changes in the scattering intensity of individual nanostructures and applied their respective calibration equation to obtain the concentration of ATP localized at each assembly. We then used an image interpolation method to map out the concentration of ATP between the nanostructures which were anchored a few micrometers apart. Figure 3.6g and h show the concentration maps of ATP from a single SKOV3.ip1 and HEY cell corresponding to Figure 3.6a and 3.6b, respectively. The concentration of expunged ATP reaches as high as 50 mM locally for the SKOV3.ip1 cell whereas it is lower for the HEY cell. The intracellular ATP levels of bacterial *E. coli* and human HeLa cells have been reported to be few millimolar using FRET-related techniques.[42,49-51] The high concentration we obtained could be due to the evaporation of the small volume of lysis buffer, which concentrated the cell contents. It is also possible that the fluorescence-based studies reached a saturation of signal at a concentration of ~10 mM.

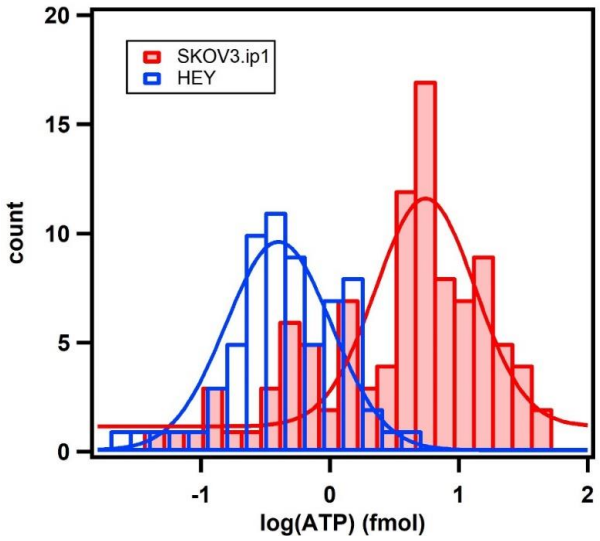

Figure 3.7. Distributions of the expunged intracellular ATP content for SKOV3.ip1 cells (red) and HEY cells (blue) from the analysis of 110 and 60 cells, respectively. The fits are Gaussian distributions.

To obtain the total amount of ATP per cell, we integrated the concentration map over the sensing volume, which was estimated to be 500 nm in height over the area of interest. The distributions of the intracellular ATP content for SKOV3.ip1 and HEY cells from the analyses of 110 and 60 cells, respectively, are shown in Figure 3.7. When fitted to Gaussian distributions, the intracellular ATP of SKOV3.ip1 cells is centred at 5.53 fmole compared to 0.40 fmole for HEY cells, resulting in a 13.8-fold difference. On the other hand, the average value of ATP for SKOV3.ip1 is 11.6-fold higher than HEY cells.

We performed comparative ensemble measurements to determine the ATP levels of the two cell lines. Similar numbers of SKOV3.ip1 and HEY cells were seeded separately; after 16 hours, the number of cells was counted again and HEY cells were observed to grow 2.7 times faster than SKOV3.ip1. The cell lysates were analysed using two bulk methods - the Luciferase assay and the nanoparticle assemblies without the addition of glycerol (as in Figure 3.1a - d). We obtained a 3.0-fold difference in the ATP levels between the two cell lines based on the analysis

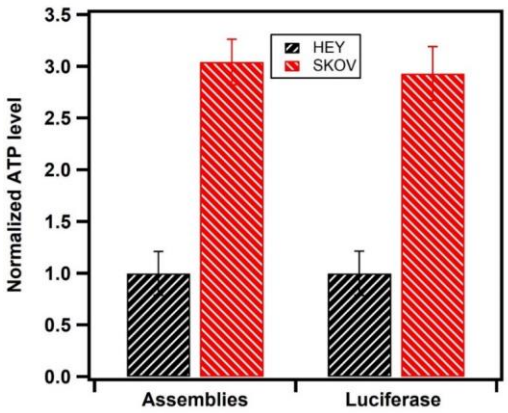

Figure 3.8. The ensemble ATP levels of two ovarian cell lines (SKVO3.ip1 and HEY) measured using nanoparticle (without glycerol) and luminescence luciferase assay. Error bars represent the standard deviation of triplicate samples.

of the entire darkfield image containing the nanoparticle assemblies,[22] in line with the 2.9-fold difference determined from the Luciferase assay (Fig. 3.8). When the faster growth rate and the greater number of HEY than SKOV3.ip1 cells in the ensemble measurements are taken into account, the difference of ATP levels between SKOV3.ip1 and HEY is ~8.7-fold, in agreement with the single-cell analysis.

3.3.5 Control Experiments

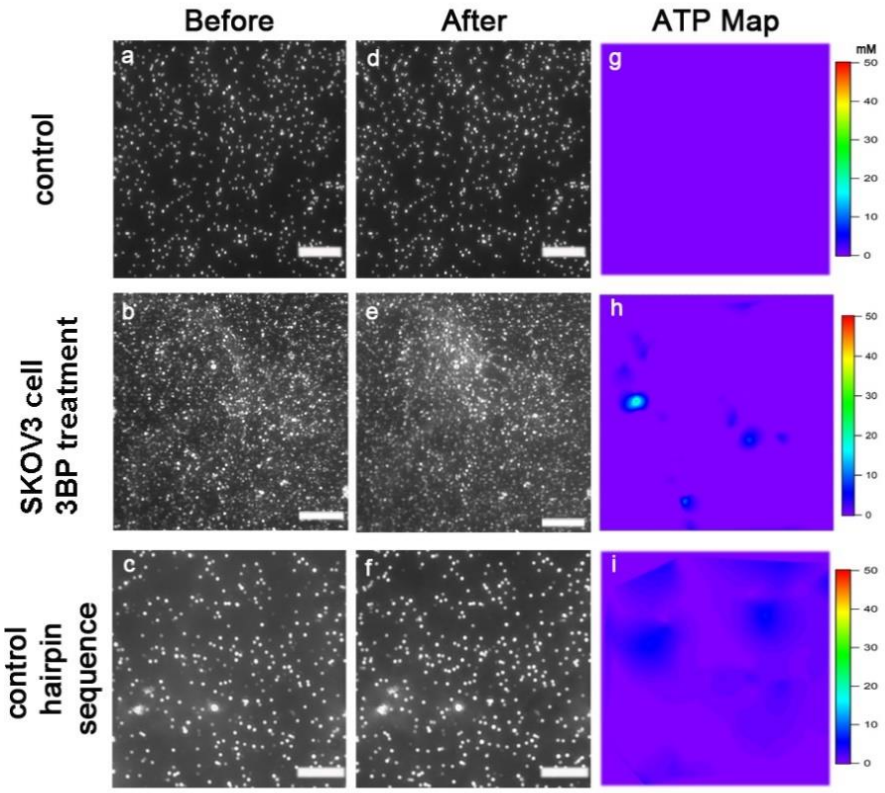

Figure 3.9. Darkfield images of control experiments of ATP-aptamer linked AuNP assemblies: before and after exposure to the lysis buffer without cells (a without cells and d); to cells treated with 3-bromopyruvate (b and e). Darkfield images of a control sample comprising assemblies linked by non-ATP-targeting DNA sequences (Seq. 3 and 4) before (c) and after (f) in contact with lysed cells. The interpolated ATP concentration maps are shown in (g), (h) and (i) correspondingly. Scale bar: 10 μm.

We carried out control experiments in which the ATP-aptamer linked nanoparticle assemblies were exposed to the lysis buffer alone and the non-targeting assemblies were exposed to lysed cells. Figure 3.9a and d show the gray-scale images of the ATP-linked nanoparticle assemblies before and after exposure to the lysis buffer without cells, and the non-targeting assemblies before and after exposure to lysed cells (Fig. 3.9c and f). These control experiments show negligible changes in the scattering intensity of the assemblies, suggesting that neither the lysis buffer nor other cellular species lead to the cleavage of the linker. Additionally, since the sensing substrate was rinsed and imaged separately, there was negligible optical interference from the cell debris. As an additional control, we tested the response of the ATP-aptamer linked nanoparticle assemblies to SKOV3.ip1 cells treated with an ATP-depleting reagent. The alkylating agent, 3-bromopyruvate (3BP), is a potent inhibitor of GAPDH enzyme in the glycolysis process that can lead to cell death;[36,52] its effect on the ATP production of the cells was confirmed using the luciferase assay (Fig. 3.10). The scattering intensity of the nanoparticle assemblies before and after exposure to the ATP-depleted cells again remains similar (Fig. 3.9b and e). Hence all three

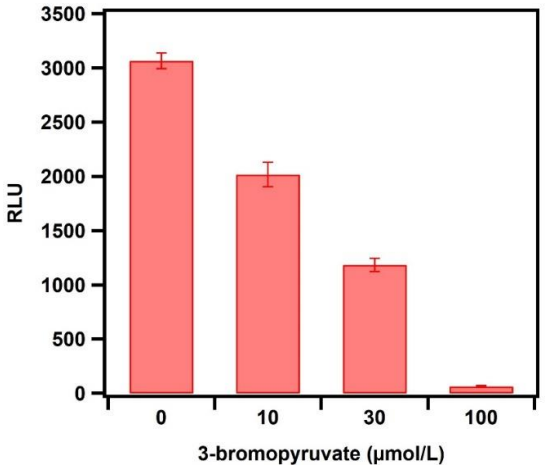

Figure 3.10. ATP levels of SKOV3.ip1 cells treated with 3-bromopyruvate for 16 hours as measured by luciferase luminescent activity.

control experiments yielded indistinguishable concentration maps. The findings support that the disassembly arises from the binding of ATP and there is no interference or false positives from other lysed cellular species.

3.3.6 Sensing of Heterogeneous 2D Surfaces

Lastly, we demonstrate the potential of the sensing platform for mapping out the target in the 2D microenvironment. We patterned a substrate with linear arrays of ATP via microcontact printing.[53] The parallel stripes of ATP are ~1 μm wide and ~13 μm spaced apart as shown in Figure 3.11a inset. Figure 3.11a-b show the darkfield scattering images of the nanoparticle assemblies before and after being in contact with the ATP-patterned substrate under a minimal amount of glycerol-containing buffer. The scattering intensity decreases congruently at locations of ATP, albeit the dissolution and diffusion of the molecules yielded disassembly across a wider area (~6 μm) than the ATP pattern.

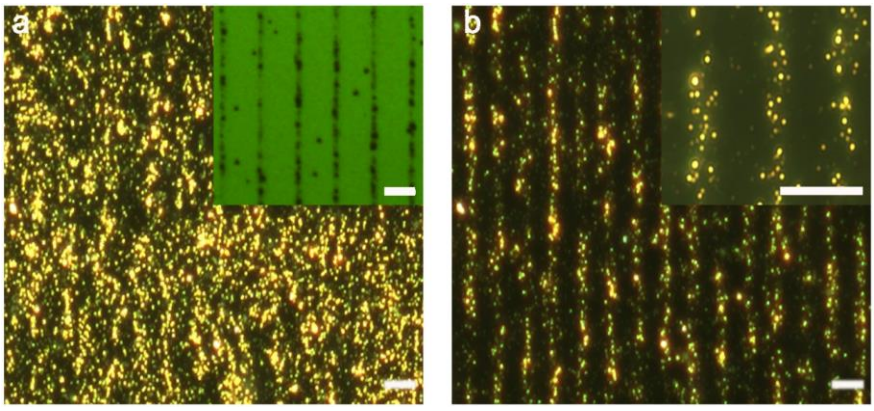

Figure 3.11. Darkfield images of AuNP assemblies before (a) and after (b) in contact with ATP patterned on a substrate for <1 min. The brightfield reflectance image of the microcontact-printed ATP is shown in the inset of (a). Scale bar: 10 μm.

3.4 Conclusions

In summary, we developed both the experimental and data processing methods for quantifying local concentrations of the analyte using discrete plasmonic AuNP assemblies. The label-free methodology is rapid and cost-effective without any separation or purification step. The stick-and-peel approach for analyzing expunged metabolites with nanoparticle sensors fabricated on a separate substrate circumvents the need of transporting nanoparticles inside cells, where the rate and mechanisms of endocytosis can be variable or altered depending on cell biology. The ability to quantify target concentration at micron-scale further paves the way for mapping of local environment and heterogeneity of complex biological samples such as tissue and tumor slices. We envision that this sensing patch can combine with the portable smartphone-based microscope and cloud-based data processing and analysis, which may facilitate on-site molecular pathology without personnel of expertise. By modifying the DNA-linkers in the plasmonic nanoparticle assemblies for various biomarkers, our sensing platform may provide alternative opportunities in biodiagnostics and advances in personalized healthcare.

3.5 Methods

Reagents and materials

Colloidal gold nanoparticle solutions were purchased from BBI Solutions. Anhydrous ethanol and 2-propanol were purchased from Commercial Alcohol, and water used for all experiments was purified using a Millipore system. Methoxy poly(ethyleneglycol)succinimidyl valerate (mPEG-SVA, MW = 5000 g/mol) was obtained from Layson Bio Inc. Triton X-100 was obtained from BioShop Canada Inc. Polydimethylsiloxane (PDMS – Sylgard 184) was purchased from Dow Corning Corporation. 3-aminoproyl trimethoxysilane (APTMS) was purchased from

Sigma Aldrich. Oligonucleotides were obtained from Integrated DNA Technologies. Thiolated DNA sequences were purified by HPLC.

DNA sequences

ATP-targeting assemblies:

Seq 1: 5'- T GAC ACC TTA_{10}-$(CH_2)_3$- SH- 3'

Seq 2: 5'- ACC TGG GGG AGT ATT GCG GAG GAA GGT GTC ACA A_{10}-$(CH_2)_3$- SH- 3'

Control assemblies:

Seq 3: 5'-SH-$(CH_2)_6$-TCT CAA CTC GTA CGC ATG ATT GTT TTC AAT CAT GCG CGA AAG ATC CTG AAT GCG -3'

Seq 4: 5'-SH-$(CH_2)_6$-A_{10} CG CAT TCA GGAT -3'

Fabrication of assemblies on the PDMS stamp

The procedure is referred to Chapter 2. Briefly, the core nanoparticles of 60 nm were anchored on APTMS-functionalized PDMS stamp and then functionalized DNA. The subtracted was then passivated to deactivate excess amino groups. The layer-by-layer build up was achieved by incubating with DNA-functionalized Au satellite NPs.

Cell culture and lysis experiments

SKOV3.ip1 and HEY cells were obtained and cultured as previously reported.[55] Briefly, SKOV3.ip1 cells were maintained in McCoy's (Sigma-Aldrich, Oakville, ON, Canada) culture media, supplemented with 10% fetal bovine serum (Gibco Thermofisher, Burlington, ON, Canada). HEY cells were cultured in Dulbecco's Modified Eagle Medium (DMEM) (GE HyClone, Logan, UT, USA) containing 10% fetal bovine serum. Cells were regularly checked to make sure they were free of mycoplasma contamination. They were re-seeded on the cell culturing coverslips (Sarstedt, Newton, NC, USA) and grown for 16 h. For bulk measurement, similar numbers of cells of SKOV3.ip1 and HEY were seeded; for single-cell experiment, the number of seeded HEY cells

was reduced to obtain a similar confluency (~50 %) for both cell lines after 16 h of growth. For control experiment with ATP-depleting reagent, SKOV3.ip1 cells were incubated with 3-bromopyruvate at the specified concentrations.

A volume of 5 μL lysing buffer containing 0.01 M PB, 0.15 M NaCl, 0.02% Triton X-100 and 20% (v/v) glycerol was placed on the PDMS substrate containing the nanoparticle assemblies. The coverslip with cells was rinsed with 0.01 M PBS, dried and immediately placed gently on the PDMS substrate. After 30 minutes of incubation to ensure completion of cell lysis, the coverslip was removed and the PDMS substrate was washed with buffer (0.01 M PB, 0.15 M NaCl) and placed on a clean coverslip for imaging. The darkfield images of nanoparticle assemblies were captured before and after the sandwich assay in buffer.

Patterning and mapping of ATP on cover slip

An APTMS-functionalized cover slip was used as the substrate for microcontact printing of ATP patterns. A diffraction grating (GR1325-07106, 75 lines/mm, Thorlabs) hydrophobized with trichloro(1H,1H,2H,2H-perfluorooctyl)-silane was used as the master. The PDMS precursor mixture was cast on the grating master, followed by evacuation for 30 minutes. The PDMS replica was then cured in an oven at 60 ^{o}C for 8 hours.

A concentration of 20 mg/mL ATP solution was prepared in ethanol. The ATP solution was then transferred on PDMS stamp using a cotton swab and the stamp was placed on the ATPMS-silanized cover slip under a weight of 5 gram. After 5 minutes, the PDMS stamp was peeled off and the coverslip was used immediately for experiment.

The patterned ATP on coverslip was placed in contact with the AuNP assemblies anchored on PDMS for less than one minute with 2 μL of buffer containing 0.01 M PB, 0.15 M NaCl, and

20% (v/v) glycerol. The darkfield images of nanoparticle assemblies were captured before and after the sandwich assay in buffer.

Darkfield imaging and analysis

Nanostructures in the sample area (100 x 100 μm^2) were visualized using a Nikon TE-2000U inverted microscope fitted with a darkfield condenser and 60x objective. The microscope was connected to a CCD camera (Jenoptik) and darkfield images were captured at an integration time of 200 ms. The darkfield images were overlaid and converted to 8-bit JPEG grayscale that expresses the intensity on a scale from 0 to 255. For the analysis of individual assembly, the coordinates of the center of the assemblies were identified by using the Localizer toolkit in Igor; this can also be achieved using common bio-imaging analysis software such as CellProfiler. The intensity of the surrounding 81 pixels for each assembly was averaged and corrected by the background intensity. Nanoparticle assemblies with average initial intensity between 50 and 200 were used for sensing experiments. The intensity has an arbitrary unit.

The concentration maps were generated using the Voronoi image interpolation function in Igor. Briefly a matrix containing the coordinates of the assemblies and the extrapolated ATP concentrations from the calibration curve was established. A 3D surface representation was then processed via the triangulation of the xyz data using Voronoi interpolation.

ATP luminescent assay

The luminescent ATP detection assay was purchased from ABcam. SKOV3.ip1 and HEY cells were grown in 96-well plates at 37 ^oC for 12 - 16 hours. A volume of 50 µL of detergent was added to the wells and the plate was shaken for 5 minutes to lyse the cells. A volume of 50 µL of

substrate solution was added in the dark. The microplate was shaken for an additional 10 minutes. The luminescence was measured by a microplate reader.

Scanning electron microscopy

A Quanta FEG 250 electron microscope operating at 10.0 kV in low vacuum mode was used. The approximate location of the AuNP assemblies near a lysed SKOV3.ip1 cell was identified by conductive ink markings at the edge of the PDMS. A collage of darkfield optical images was captured for correlating the structures found in the SEM.

3.6 References

(1) Altschuler, S. J.; Wu, L. F. Essay Cellular Heterogeneity : Do Differences Make a Difference ? *Cell* **2010**, *141*, 559–563.

(2) Chattopadhyay, P. K.; Gierahn, T. M.; Roederer, M.; Love, J. C. Single-Cell Technologies for Monitoring Immune Systems. *Nat. Immunol.* **2014**, *15*, 128–135.

(3) Khoo, B. L.; Chaudhuri, P. K.; Ramalingam, N.; Shao, D.; Tan, W.; Lim, C. T.; Warkiani, M. E. Single-Cell Profiling Approaches to Probing Tumor Heterogeneity. *Int. J. Cancer* **2016**, *139*, 243–255.

(4) Kelsey, G.; Stegle, O.; Reik, W. Single-Cell Epigenomics: Recording the Past and Predicting the Future. *Science* **2017**, *358*, 69–75.

(5) Lawson, D. A.; Kessenbrock, K.; Davis, R. T.; Pervolarakis, N.; Werb, Z. Tumour Heterogeneity and Metastasis at Single-Cell Resolution. *Nat. Cell Biol.* **2018**, *20*, 1349–1360.

(6) Zhao, J.; Gao, J.; Xue, W.; Di, Z.; Xing, H.; Lu, Y.; Li, L. Upconversion Luminescence-Activated DNA Nanodevice for ATP Sensing in Living Cells. *J. Am. Chem. Soc.* **2018**, *140*, 578–581.

(7) Zhang, L.; Sevinsky, C. J.; Davis, B. M.; Vertes, A. Single-Cell Mass Spectrometry of Subpopulations Selected by Fluorescence Microscopy. *Anal Chem.* **2018**, *90*, 4626–4634.

(8) Liu, R.; Zhang, G.; Yang, Z. Towards Rapid Prediction of Drug-Resistant Cancer Cell Phenotypes : Single Cell Mass Spectrometry Combined with Machine Learning. *Chem. Commun.* **2019**, *55*, 616–619.

(9) Ajami, B.; Samusik, N.; Wieghofer, P.; Ho, P. P.; Crotti, A.; Bjornson, Z.; Prinz, M.; Fantl, W. J.; Nolan, G. P.; Steinman, L. Single-Cell Mass Cytometry Reveals Distinct Populations of Brain Myeloid Cells in Mouse Neuroinflammation and Neurodegeneration Models. *Nat.*

Neurosci. **2018**, *21*, 541–551.

(10) Zhang, L.; Vertes, A. Single-Cell Mass Spectrometry Approaches to Explore Cellular Heterogeneity. *Angew. Chemie Int. Ed.* **2018**, *57*, 4466–4477.

(11) Taniguchi, Y.; Choi, P. J.; Li, G.; Chen, H.; Babu, M.; Hearn, J.; Emili, A.; Xie, X. S. Quantifying E. Coli Proteome and Transcriptome with Single-Molecule Sensitivity in Single Cells. *Science* **2011**, *329*, 533–538.

(12) Chattopadhyay, P. K.; Price, D. A.; Harper, T. F.; Betts, M. R.; Yu, J.; Gostick, E.; Perfetto, S. P.; Goepfert, P.; Koup, R. A.; Rosa, S. C. De; *et al.* Quantum Dot Semiconductor Nanocrystals for Immunophenotyping by Polychromatic Flow Cytometry. *Nat. Med.* **2006**, *12*, 972–977.

(13) Barlogie, B.; Raber, M. N.; Schumann, J.; Johnson, T. S.; Drewinko, B.; Swartzendruber, D. E.; Göhde, W.; Andreeff, M.; Freireich, E. J. Flow Cytometry in Clinical Cancer Research. *Cancer Res.* **1983**, *43*, 3982–3997.

(14) Newman, J. R. S.; Ghaemmaghami, S.; Ihmels, J.; Breslow, D. K.; Noble, M.; Derisi, J. L.; Weissman, J. S. Single-Cell Proteomic Analysis of S. Cerevisiae Reveals the Architecture of Biological Noise. *Nature* **2006**, *441*, 840–846.

(15) Gilman, S. D.; Ewing, A. G. Analysis of Single Cells by Capillary Electrophoresis with On-Column Derivatization and Laser-Induced Fluorescence Detection. *Anal. Chem.* **1995**, *67*, 58–64.

(16) Onjiko, R. M.; Portero, E. P.; Moody, S. A.; Nemes, P. In Situ Microprobe Single-Cell Capillary Electrophoresis Mass Spectrometry: Metabolic Reorganization in Single Differentiating Cells in the Live Vertebrate (Xenopus Laevis) Embryo. *Anal. Chem.* **2017**, *89*, 7069–7076.

(17) Nemes, P.; Knolho, A. M.; Rubakhin, S. S.; Sweedler, J. V. Metabolic Differentiation of Neuronal Phenotypes by Single-Cell Capillary Electrophoresis — Electrospray Ionization-Mass Spectrometry. *Anal. Chem.* **2011**, *83*, 6810–6817.

(18) Hughey, J. J.; Lee, T. K.; Lipniacki, T.; Quake, S. R.; Covert, M. W. Single-Cell NF- k B Dynamics Reveal Digital Activation and Analogue Information Processing. *Nature* **2010**, *466*, 267–272.

(19) Standke, S. J.; Colby, D. H.; Bensen, R. C.; Burgett, A. W. G.; Yang, Z. Mass Spectrometry Measurement of Single Suspended Cells Using a Combined Cell Manipulation System and a Single-Probe Device. *Anal. Chem.* **2019**, *91*, 1738–1742.

(20) Zhao, J.; Zhang, F.; Guo, Y. Quantitative Analysis of Metabolites at the Single-Cell Level by Hydrogen Flame Desorption Ionization Mass Spectrometry. *Anal Chem.* **2019**, *91*, 2752–2758.

(21) Wang, Y.; MacLachlan, E.; Nguyen, B. K.; Fu, G.; Peng, C.; Chen, J. I. L. Direct Detection of MicroRNA Based on Plasmon Hybridization of Nanoparticle Dimers. *Analyst* **2015**, *140*, 1140–1148.

(22) Le, N. H.; Nguyen, B. K.; Ye, G.; Peng, C.; Chen, J. I. L. Tuning the Sensing Performance

of Multilayer Plasmonic Core-Satellite Assemblies for Rapid Detection of Targets from Lysed Cells. *ACS Sensors* **2017**, *2*, 1578–1583.

(23) Chen, J. I. L.; Durkee, H.; Traxler, B.; Ginger, D. S. Optical Detection of Protein in Complex Media with Plasmonic Nanoparticle Dimers. *Small* **2011**, *7*, 1993–1997.

(24) Chen, J. I. L.; Chen, Y.; Ginger, D. S. Plasmonic Nanoparticle Dimers for Optical Sensing of DNA in Complex Media. *J. Am. Chem. Soc.* **2010**, *132*, 9600–9601.

(25) Guo, L.; Xu, Y.; Ferhan, A. R.; Chen, G.; Kim, D. H. Oriented Gold Nanoparticle Aggregation for Colorimetric Sensors with Surprisingly High Analytical Figures of Merit. *J. Am. Chem. Soc.* **2013**, *135*, 12338–12345.

(26) Li, K.; Qin, W.; Li, F.; Zhao, X.; Jiang, B.; Wang, K.; Deng, S.; Fan, C.; Li, D. Nanoplasmonic Imaging of Latent Fingerprints and Identification of Cocaine. *Angew. Chem. Int. Ed* **2013**, *52*, 11542–11545.

(27) Kreuzer, M. P.; González, M. U.; Quidant, R.; Fotoniques, I. D. C.; Park, M. T. Plasmon Near-Field Coupling in Metal Dimers as a Step toward Single-Molecule Sensing. *ACS Nano* **2009**, *3*, 1231–1237.

(28) Sönnichsen, C.; Reinhard, B. M.; Liphardt, J.; Alivisatos, A. P.; Sonnichsen, C.; Reinhard, B. M.; Liphard, J.; Alivisatos, A. P. A Molecular Ruler Based on Plasmon Coupling of Single Gold and Silver Nanoparticles. *Nat. Biotechnol.* **2005**, *23*, 741–745.

(29) Xiao, R.; Wang, D.; Lin, Z.; Qiu, B.; Liu, M.; Guo, L.; Chen, G. Disassembly of Gold Nanoparticle Dimers for Colorimetric Detection of Ochratoxin A. *Anal. Methods* **2015**, *7*, 842–845.

(30) Mirkin, C. A.; Letsinger, R. L.; Mucic, R. C.; Storhoff, J. J. A DNA-Based Method for Rationally Assembling Nanoparticles into Macroscopic Materials. *Nature* **1996**, *382*, 607–609.

(31) Storhoff, J. J.; Elghanian, R.; Mucic, R. C.; Mirkin, C. A.; Letsinger, R. L. One-Pot Colorimetric Differentiation of Polynucleotides with Single Base Imperfections Using Gold Nanoparticle Probes. *J. Am. Chem. Soc.* **1998**, *120*, 1959–1964.

(32) Jun, Y.; Sheikholeslami, S.; Hostetter, D. R.; Tajon, C.; Craik, C. S.; Alivisatos, A. P. Continuous Imaging of Plasmon Rulers in Live Cells Reveals Early-Stage Caspase-3 Activation at the Single-Molecule Level. *Proc. Natl. Acad. Sci. U. S. A.* **2009**, *106*, 17735–17740.

(33) Waldeisen, J. R. R.; Wang, T.; Ross, B. M. M.; Lee, L. P. P. Disassembly of a Core–Satellite Nanoassembled Substrate for Colorimetric Biomolecular Detection. *ACS Nano* **2011**, *5*, 5383–5389.

(34) Zhang, T.; Li, H.; Hou, S.; Dong, Y.; Pang, G.; Zhang, Y. Construction of Plasmonic Core-Satellite Nanostructures on Substrates Based on DNA-Directed Self-Assembly as a Sensitive and Reproducible Biosensor. *ACS Appl. Mater. Interfaces* **2015**, *7*, 1–5.

(35) Zhao, X.; Xu, L.; Sun, M.; Ma, W.; Wu, X.; Kuang, H.; Wang, L.; Xu, C. Gold-Quantum Dot Core–Satellite Assemblies for Lighting Up MicroRNA In Vitro and In Vivo. *Small*

2016, *12*, 4662–4668.

(36) Zhou, Y.; Tozzi, F.; Chen, J.; Fan, F.; Xia, L.; Wang, J.; Gao, G.; Zhang, A.; Xia, X.; Brasher, H.; *et al.* Intracellular ATP Levels Are a Pivotal Determinant of Chemoresistance in Colon Cancer Cells. *Cancer Res.* **2012**, *72*, 304–314.

(37) Liberti, M. V.; Locasale, J. W. The Warburg Effect: How Does It Benefit Cancer Cells? *Trends Biochem. Sci.* **2016**, *41*, 211–218.

(38) Koppenol, W. H.; Bounds, P. L.; Dang, C. V. Otto Warburg's Contributions to Current Concepts of Cancer Metabolism. *Nat. Rev. Cancer* **2011**, *11*, 325–337.

(39) Gillies, R. J.; Robey, I.; Gatenby, R. A. Causes and Consequences of Increased Glucose Metabolism of Cancers. *J. Nucl. Med.* **2008**, *49*, 24S-42S.

(40) Furuya, K.; Sokabe, M.; Grygorczyk, R. Real-Time Luminescence Imaging of Cellular ATP Release. *Methods* **2014**, *66*, 330–344.

(41) Kim, J.; Ahn, J.; Barone, P. W.; Jin, H.; Zhang, J.; Heller, D. A.; Strano, M. S. A Luciferase / Single-Walled Carbon Nanotube Conjugate for Near- Infrared Fluorescent Detection of Cellular ATP. *Angew. Chem. Int. Ed* **2010**, *49*, 1456–1459.

(42) Imamura, H.; Huynh Nhat, K. P.; Togawa, H.; Saito, K.; Iino, R.; Kato-Yamada, Y.; Nagai, T.; Noji, H. Visualization of ATP Levels inside Single Living Cells with Fluorescence Resonance Energy Transfer-Based Genetically Encoded Indicators. *Proc. Natl. Acad. Sci. U. S. A.* **2009**, *106*, 15651–15656.

(43) Yaginuma, H.; Kawai, S.; Tabata, K. V.; Tomiyama, K.; Kakizuka, A.; Komatsuzaki, T.; Noji, H.; Imamura, H. Diversity in ATP Concentrations in a Single Bacterial Cell Population Revealed by Quantitative Single-Cell Imaging. *Sci. Rep.* **2014**, *4*, 6522.

(45) Nutiu, R.; Li, Y. Structure-Switching Signaling Aptamers. *J. Am. Chem. Soc.* **2003**, *125*, 4771–4778.

(46) Lau, P. S.; Li, Y. Exploration of Structure-Switching in the Design of Aptamer Biosensors. *Adv. Biochem. Eng. Biotechnol.* **2014**, *140*, 69–92.

(47) Nutiu, R.; Li, Y. Structure-Switching Signaling Aptamers: Transducing Molecular Recognition into Fluorescence Signaling. *Chem. - A Eur. J.* **2004**, *10*, 1868–1876.

(48) Yu, D.; Wolf, J. K.; Scanlon, M.; Price, J. E.; Hung, M. Enhanced C-ErbB-2/Neu Expression in Human Ovarian Cancer Cells Correlates with More Severe Malignancy That Can Be Suppressed by E1A. *Cancer Res.* **1993**, *53*, 891–898.

(49) Buick, R.; Pullano, R.; Trent, J. Comparative Properties of Five Human Ovarian Adenocarcinoma Cell Lines. *Cancer Res.* **1985**, *45*, 3668–3676.

(50) Traut, T. W. Physiological Concentrations of Purines and Pyrimidines. *Mol. Cell. Biochem.* **1994**, *140*, 1–22.

(51) Zheng, D.; Seferos, D. S.; Giljohann, D. A.; Patel, P. C.; Mirkin, C. A. Aptamer Nano-Flares for Molecular Detection in Living Cells. *Nano Lett.* **2009**, *9*, 3258–3261.

(52) Özalp, V. C.; Nielsen, L. J.; Olsen, L. F. An Aptamer-Based Nanobiosensor for Real-Time Measurements of ATP Dynamics. *ChemBioChem* **2010**, *11*, 2538–2541.

(53) Xia, Y.; Tien, J.; Qin, D.; Whitesides, M. Non-Photolithographic Methods for Fabrication of Elastomeric for Use Stamps in Microcontact Printing. *Langmuir* **1996**, *12*, 4033–4038.

(54) Hurst, S. J.; Lytton-Jean, A. K. R.; Mirkin, C. A. Maximizing DNA Loading on a Range of Gold Nanoparticle Sizes. *Anal. Chem.* **2006**, *78*, 8313–8318.

(55) Bernaudo, S.; Salem, M.; Qi, X.; Zhou, W.; Zhang, C.; Yang, W.; Rosman, D.; Deng, Z.; Ye, G.; Yang, B.; *et al.* Cyclin G2 Inhibits Epithelial-to-Mesenchymal Transition by Disrupting Wnt/β -Catenin Signaling. *Oncogene* **2016**, *35*, 4816–4827.

Chapter 4 – Core-Satellite Assembly of Gold Nanoshells on Solid Gold Nanoparticle for Color Coding Plasmonic Nanosensor

(This chapter is partly reproduced with permission from Le, N. H.; Cathcart, N.; Kitaev, V.; Chen, J. I. L. *Analyst* **2022**, 147, 155-164. The part of the publication on the nanoshell assembly is presented here.)

The synthesis of gold nanoshell was carried out by Nicole Cathcart. All experiments presented in this chapter were carried out by Nguyen Le.

4.1 Abstract

Chapters 2 and 3 outlined the sensing capabilities of core-satellite nanostructure comprising a solid gold nanoparticle as the core and solid gold nanoparticles as satellites. In this chapter, we present the tuning of the optical properties of the nanostructure by using different building blocks – solid gold nanoparticle as the core and hollow decahedral gold nanoshells as satellites. The core-satellite assemblies were fabricated on a substrate via the layer-by-layer assembly of nanoparticles linked by DNA. We used finite-difference time-domain simulations to help guide the geometrical design and characterized the optical properties and morphology of the solid-shell nanoparticle assemblies using darkfield microscopy, single-nanostructure spectroscopy, and scanning electron microscopy. Plasmon coupling yielded resonant peaks at longer wavelengths in the red to near-infrared range for solid-shell assemblies compared with solid-solid nanoparticle assemblies. We examined sensing with the solid-shell assemblies using adenosine triphosphate (ATP) as a model target and ATP-aptamer as the linker. Binding of ATP induced disassembly and led to a decrease in the scattering intensity and a color change from red to green. Our work expands the capability

of chip-based plasmonic nanoparticle assemblies for the analysis of multiple, different types of biomolecules in small sample sizes including the microenvironment and single cells

4.2 Introduction

Colorimetric sensors based on single or coupled plasmonic nanoparticles (NPs) are explored for sensing and point-of-care diagnostics because of their low cost, rapid optical response, ease of manipulation, photostability, and simple data acquisition and analysis. Plasmonic NPs exhibit unique optical properties arisen from localized surface plasmon resonance (LSPR). Upon interaction with light, the free electrons on the surface of the NP undergo a collective coherent oscillation, leading to an enhancement of the electromagnetic field near the NP surface and strong light scattering and absorption. The LSPR depends on the size, shape, and the refractive index at the metal-dielectric interface. A spectral shift of plasmon resonance driven by refractive index changes underpins the main mechanism employed in many sensing applications.[1,2] Furthermore, extending LSPR-based sensing platforms from bulk colloidal solutions[3,4] and films to discrete individual nanostructures[5,6] yields several advantages, including high sensitivity, low sample volume, and low detection limit.[7–10] Chip-based sensors are also desirable for multiplexing and portability.[11]

In NP assemblies or complex nanostructures, the LSPR of individual building blocks can couple, creating new plasmon modes[12] that yield electromagnetic field hot spots and shifts in the LSPR peak. The plasmonic coupling can be described by the plasmon hybridization model, pioneered by Nordlander and coworkers,[13] where plasmons of individual NPs can hybridize antisymmetrically or symmetrically. The energy of hybridized plasmon depends on the interparticle distance, thereby giving rise to the concept of plasmon ruler[14] for monitoring biomolecular interactions.

In chapter 2, we presented core-satellite assemblies with a tunable number of conventional solid Au nanoparticles (AuNPs) functionalized with reconfigurable DNA linkers.[15] The AuNP assemblies exhibited a red-shifted LSPR (ca. 600 nm) and high scattering intensity due to the coupled plasmon modes[16] and changes in the dielectric environment.[17–19] The LSPR of assemblies depends not only on the interparticle separation distance[20,21] and the number of NPs (i.e. aggregate size), but also on the LSPR energy of the core and satellite constituents. Previous works on compositionally heterogeneous core-satellite assemblies explored silver and gold NPs.[18,21,22] The binary Ag-Au assemblies displayed two distinct plasmon bands due to the off-resonant coupling between the LSPR of AgNP (400 nm) and AuNP (550 nm), in contrast to the broad single resonance observed in Au-Au core-satellite assemblies. The shifts in the second LSPR band (at 560 nm) from the hybridization of the dipolar AgNP and AuNP modes were much less prominent compared with that in the Au-Au system because of the mismatch in LSPR energy.[18] For interparticle separation distance of tens of nm where useful sensing modalities can be derived, plasmon hybridization theory[23] suggests that a lower energy of hybridized plasmon mode (>650 nm) may be achieved by coupling with nanoshells that resonate at a lower energy than solid AuNP.

In this chapter, we investigate a new morphology of NP assemblies comprising building blocks both of gold but with different structures – namely solid AuNP as the core and Au nanoshells as the satellites – to extend the hybridized plasmon mode to deep red and near-infrared (NIR) wavelengths for sensing applications. We examined the optical response of the assemblies theoretically and experimentally and carried out morphological studies. We used reconfigurable DNA-aptamers as linkers to derive sensing performance where binding of the target (ATP) leads to disassembly and changes in the scattered light, which can be readily captured by darkfield microscopy and rapidly analyzed via image processing. In combination with a low-cost portable

imaging device and color identification through machine learning, the development of different types of coupled nanostructures may enable cost-effective sensing of multiple targets in small sample volumes.

4.3 Results and Discussion

4.3.1 Design of Core-Satellite Assemblies with Nanoshells on Solid Core Nanoparticle

To guide the design of solid-shell assembly, we employed finite-difference time-domain (FDTD) modelling. FDTD methods have been extensively applied to study the optical properties of materials. The simulations are based on modeling the behavior of the electromagnetic wave by exploiting the time and position dependence of Maxwell's equations in rectangular 3D cells of

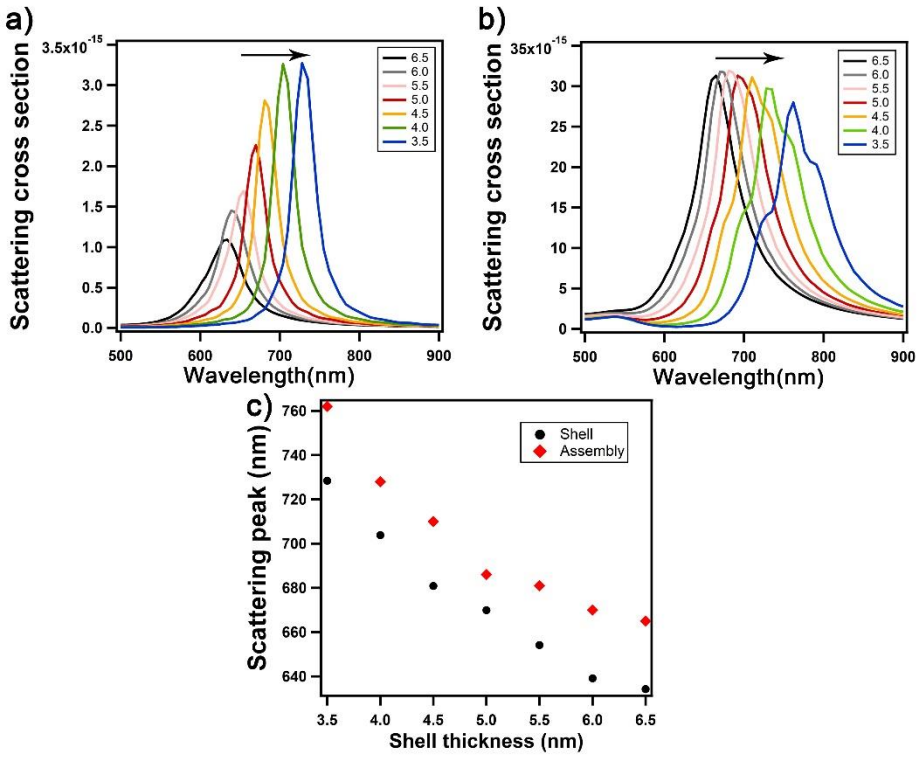

Figure 4.1. FDTD simulated scattering spectra: (a) Single 45-nm Au nanoshell with various thicknesses (3.5 – 6.5 nm), and (b) solid-shell assemblies with 5 satellite particles of the corresponding nanoshells. (c) Comparison of scattering peak wavelengths of nanoshells (black circle) and solid-shell assemblies (red diamond) vs shell thickness.

finite volume (i.e. Yee cells, see Appendix A1).[24] We first examined the optical properties of Au nanoshells intending to achieve an LSPR peak near 700 nm. The LSPR of Au nanoshell can be tuned from visible to IR region by tuning the shell thickness and overall particle size;[25,26] experimentally, nanoshells > 100 nm in size have been studied extensively, but less so for <50 nm size range which is needed for the proposed core-satellite structure. Figure 4.1a shows the simulated scattering spectra of Au nanoshells of 45-nm in diameter with various shell thicknesses; the LSPR peak redshifts as the shell thickness decreases, in agreement with the structural dimension dependence reported previously for Au shells of 120 nm in size.[25] The simulated result suggests a geometry of Au nanoshell with 45 nm in diameter and 4-5 nm in shell thickness as suitable for our goal of obtaining a LSPR peak at ~700 nm to provide a large enough spectral shift from that of conventional AuNP assemblies while staying within the responsivity range of a typical Si-based detector with a near-infrared filter, as well as having the structures be synthetically accessible. Figure 4.2a shows the simulated scattering spectra of solid-shell assemblies with an incremental number of spherical Au nanoshells randomly placed around the Au core; the LSPR peak redshifts and increases in scattering intensity with an increasing number of satellite particles. Figure 4.2b compares the simulated scattering spectra of two types of core-satellite assemblies: both consist of solid 60-nm AuNP as the core but with different types of satellite NPs – solid 30-nm AuNP vs 45-nm Au nanoshells (5-nm thickness). The two types of structures are referred to as solid-solid vs solid-shell assemblies, respectively. The solid-shell assemblies exhibit a 130-nm redshift in the LSPR from that of single solid AuNP; in contrast, conventional solid-solid assemblies exhibit a redshift of 50 nm. Notably, the scattering cross-section of the solid-shell assembly is much higher than the solid-solid assembly because of the high quality factor of plasmon resonance strength of Au at long wavelengths. In Au solid-solid assemblies, the redshift

of the radiant mode of the LSPR results from the plasmon hybridization between core and satellite NPs.[16] Because the LSPR of the Au nanoshell is much lower in energy than solid AuNP, this difference leads to off-resonant coupling, in which the main LSPR energy of the solid-shell assembly is determined by that of the Au nanoshell. The off-resonant coupling with additional small redshifts (Fig. 4.1b,c) is similar to the plasmon hybridization between solid NPs of Ag and Au.[27]

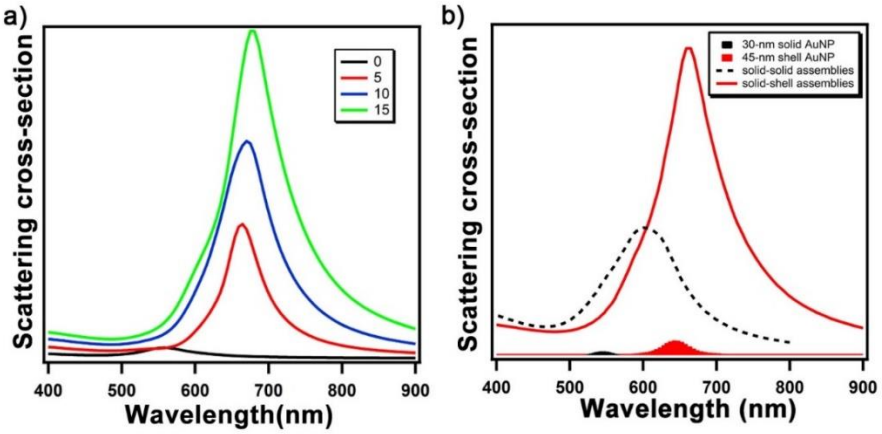

Figure 4.2. FDTD-simulated scattering spectra of AuNP core-satellite assemblies. (a) solid-shell assemblies with 0 to 15 satellite nanoshells. (b) Scattering spectra of conventional solid-solid assembly (dashed black line, 40 satellite AuNPs) vs solid-shell assembly (red line, 15 satellite nanoshells). Scattering spectra of the respective satellite nanoparticles, 30-nm solid AuNP (shaded in black) and 45-nm Au shell with 5.5-nm thickness (shaded in red), are shown for reference.

4.3.2 Synthesis and Characterization of Gold Nanoshells

Next, we synthesized Au nanoshells with desired geometry identified from the FDTD simulation using the conventional Au-seed growth method. At first, we chose Au nanoshell as the building blocks because their plasmon can easily be tuned from the visible to the infrared (IR) regions. The traditional Au nanoshells consisting of a dielectric core SiO_2 coated with a gold shell had been synthesized by the Halas group.[25] Their synthesis of spherical Au nanoshells utilizes silica NPs as templates, on top of which gold seeds would be attached as nucleation sites for the

further reduction of Au^{3+} ions to form an Au layer.[25] By controlling the number of nucleation sites and the amount of reductant used, the thickness of the gold layer can be controlled. Hence, the optical properties can be fine-tuned for the desired plasmon resonance. This conventional method in previous reports yielded Au nanoshells of 80 and 150 nm in diameter and thicknesses of > 10 nm. Although the synthetic methodologies of gold nanoshells are well adapted and reviewed in the literature,[28,29] the desired diameter and thickness of the nanoshells in the current work proved to be challenging to achieve using the Au-seeded method. In particular, for small diameter NPs, there were limited nucleation sites for the growth of the Au layer that yielded rough and incomplete shelling, and the ineffective charge repulsion of small template particles also led to aggregation.[30] Instead, we used decahedral Au nanoshells, which were synthesized by using AgNPs as templates

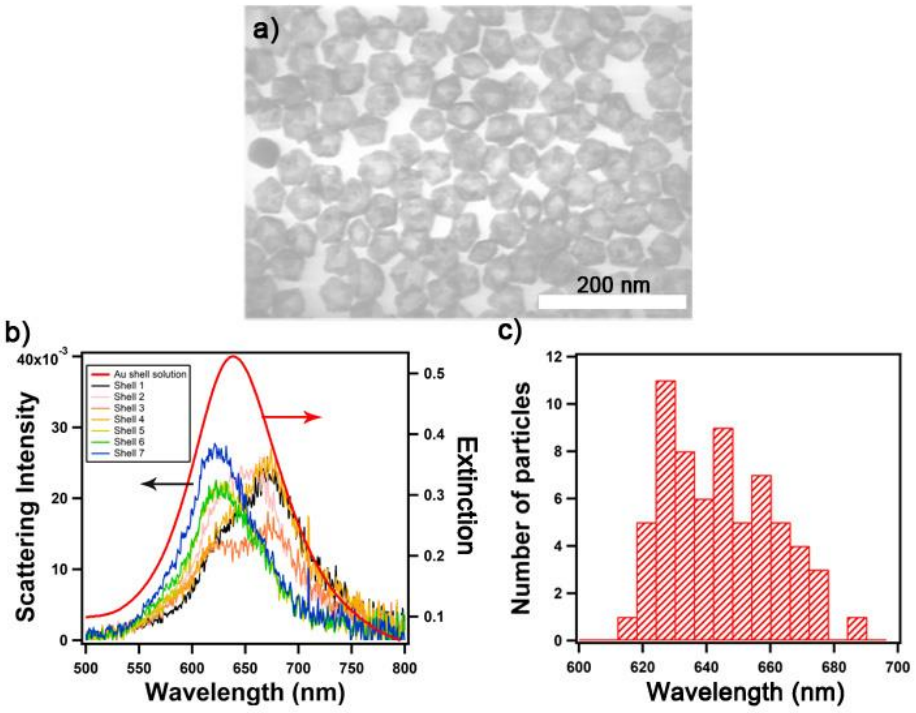

Figure 4.3. Characterization of decahedral Au nanoshells. (a) Representative TEM image of gold nanoshells, (b) scattering spectra of seven individual Au nanoshells (deposited on a substrate measured in water) overlaid with the extinction spectrum of the colloids (red), and (c) distribution of the LSPR peak of Au nanoshells obtained from single-nanostructure spectroscopy (N=60).

that were galvanically replaced by gold to yield the hollow Au nanoshells. Moreover, decahedral AgNPs are preferred over quasi-spherical particles for templating because of the narrow bandwidth of the plasmon absorption peak, high extinction, uniformity, and monodispersity.[31] Figure 4.3a shows representative TEM images of decahedral Au nanoshells; the average diameter is 44 ± 2 nm with a thickness of 6 ± 1 nm. Colloidal decahedral Au nanoshells exhibit absorbance at 637 nm while the LSPR scattering peaks for individual nanoshells vary between 620 – 680 nm (Fig. 4.3b) as measured by single-nanostructure spectroscopy. Figure 4.2c shows the distribution of the scattering peaks, which arises from variations in size, shape, roughness, and partial stellation of the shell structure.[31]

We functionalized two samples of decahedral Au nanoshells with DNA sequences denoted as Seq 1 and Seq 2 using the pH-assisted method.[32] This method promotes the adsorption of thiolated DNA strands, and was followed by salt aging to maximize the DNA loading. We observed a LSPR redshift of ca. 5 nm for Au nanoshells upon functionalization with thiolated DNA, as shown in

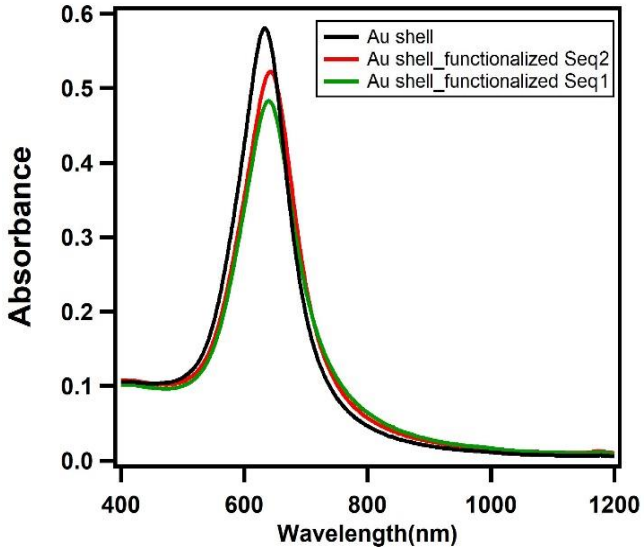

Figure 4.4. Extinction spectra of decahedral Au nanoshells in water (black), and functionalized with Seq 2 (red) and Seq 1 (green).

Table 4.1. Loading of DNA on 30-nm solid AuNP and 45-nm Au nanoshells.

Sample	Concentration of particle (nM)	Concentration of DNA (μM)	Number of strands per particle
Au30_Seq 2	0.66	0.15	234 ± 12
Au30_Seq 1	0.66	0.27	410 ± 11
Aushell45_Seq 2	0.106	0.079	749 ± 25
Aushell45_Seq 1	0.106	0.10	961 ± 13

Figure 4.4, consistent with a change of the refractive index on the plasmonic NP surface.[1,33] We examined the loading of Seq 1 and Seq 2 on Au nanoshells using a fluorescence technique; the immobilized DNA was released from the AuNP surface by dissolving AuNPs with potassium cyanide (KCN) and quantitfied the concentration by using fluorescence dye.[34] At maximum loading, Seq 1 was more densely packed at 961 strands/NP compared to Seq 2 at 749 strands/NP (Table 4.1). The DNA loading on Au nanoshells is much higher than solid 30-nm AuNP (410 Seq 1-strands/NP and 234 Seq 2-strands/NP), more than expected from the difference in size. We hypothesized that Au nanoshells may exhibit a high surface area because of the grains and roughness of the structure and also the accessible internal surface. These DNA-functionalized Au nanoshells were subsequently explored as satellite NPs for the layer-by-layer assembly.

4.3.3 Fabrication of Solid-Shell Assemblies

We fabricated the assemblies via a layer-by-layer process using DNA linkers, as established in chapter 2.[15] Briefly, 60-nm Au solid NP cores were firstly anchored on a substrate, followed by the layer build-up of Au shell satellites through DNA linkers, which have 9 complementary base pairs between Seq 2 (ATP-aptamer) and Seq 1. The process yielded a tunable number of Au nanoshells surrounding the Au solid core NP. Figure 4.5a,b shows the environmental- scanning electron microscopy (E-SEM) images of the assemblies; the 3D core-satellite morphology was evident when imaged under low vacuum. We then performed correlated darkfield optical microscopy and electron microscopy at high magnification. Figure 4.5c shows SEM images of 5

assemblies with two layers of Au satellite nanoshells. To achieve high imaging resolution, we needed to operate SEM at high-vacuum conditions that led to the drying and collapse of the 3D structure, consistent with observations of previous studies.[15,35] The collapse of the structures, serendipitously, facilitated the analysis of the number of satellite nanoshells. The corresponding darkfield scattering spectra of the assemblies are shown in Figure 4.5d. Figure 4.6 shows additional

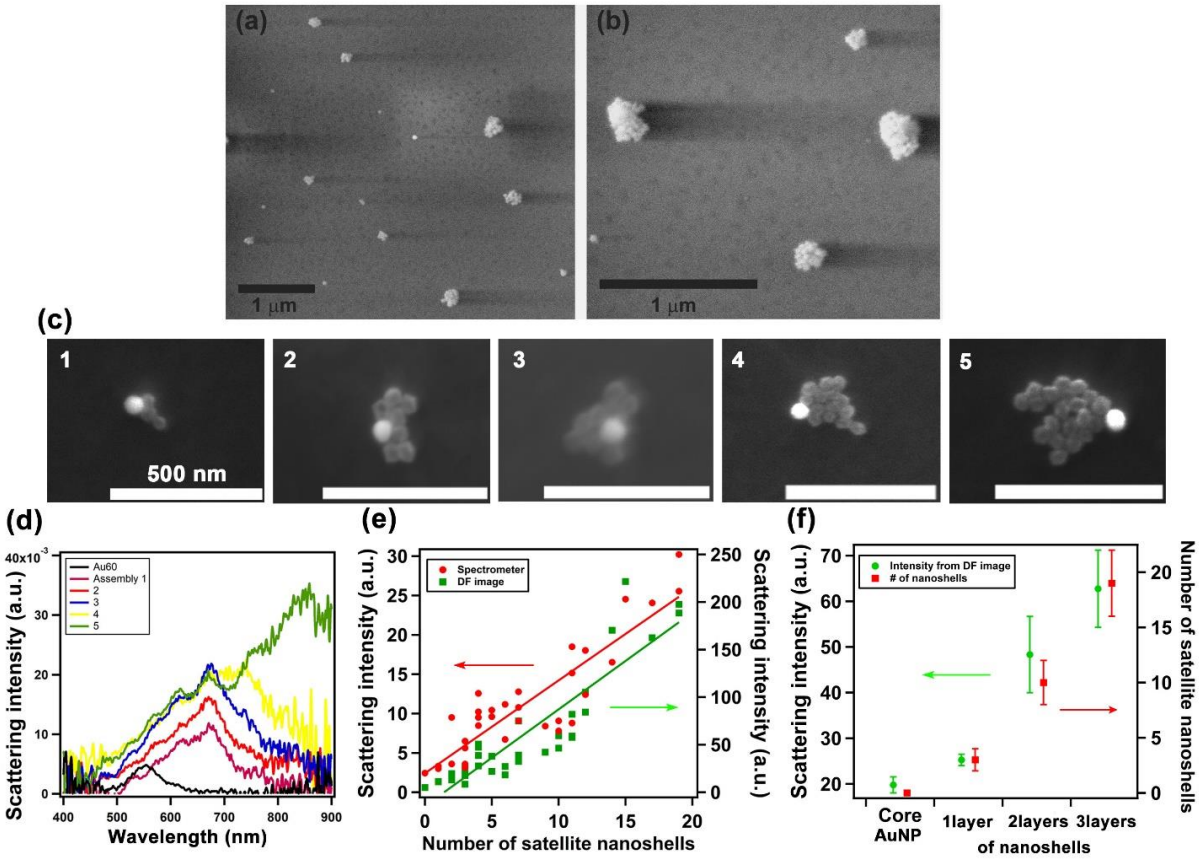

Figure 4.5. Morphological characterization and correlated SEM and single-nanostructure spectroscopy. (a, b) Environmental SEM images (under low vacuum) of assemblies showing the 3D structures; (c) High-magnification SEM images (under high vacuum) of 5 solid-shell assemblies (scale bar: 500 nm) and (d) their respective scattering spectra with that of 60-nm core AuNP shown in black. (e) Linear relationship between the scattering intensity and the number of Au satellite nanoshells for 31 assemblies: data from integrated scattering spectra (400-900 nm) shown in red and that from darkfield image analysis shown in green; (f) summary of average scattering intensity from darkfield images and number of satellite nanoshells with respect to the layer-by-layer assembly process (errors are standard deviations).

data of 30 solid-shell assemblies where the number of satellite nanoshells varied from 3 to 20. The darkfield scattering spectra of the solid-shell assemblies (Fig. 4.5d) shows that the LSPR peak redshifts from 562 nm of a solid Au core to 672 nm – 850 nm upon assembling with 2 layers of satellite nanoshells. This shift is significantly larger in magnitude than that of solid-solid assemblies, which is in agreement with the simulated data;[16,18] however, significantly variable spectral shapes of the LSPR were observed for solid-shell assemblies (Fig. 4.5d and Fig. 4.6). We hypothesized that during DNA hybridization, the unevenly distributed DNA density on the surface of the decahedral shape may affect the cooperativity and repulsion effects, leading to variations in the efficiency of the self-assembly process. The size, shape, clustering, and number of satellite nanoshells lead to differences in plasmon coupling and spectral broadening; notably, the most prominent factor is the uniformity and thickness of the nanoshells. Despite the spectral variations, a linear relationship between the spectral-integrated scattering intensity of the assemblies and the number of satellite nanoshells was observed, as shown in Figure 4.5e; a similar trend is also observed for scattering intensity extracted from darkfield image pixels. Figure 4.5f summarizes the ability to tune the scattered intensity by controlling the assembly size through the layer-by-layer process.

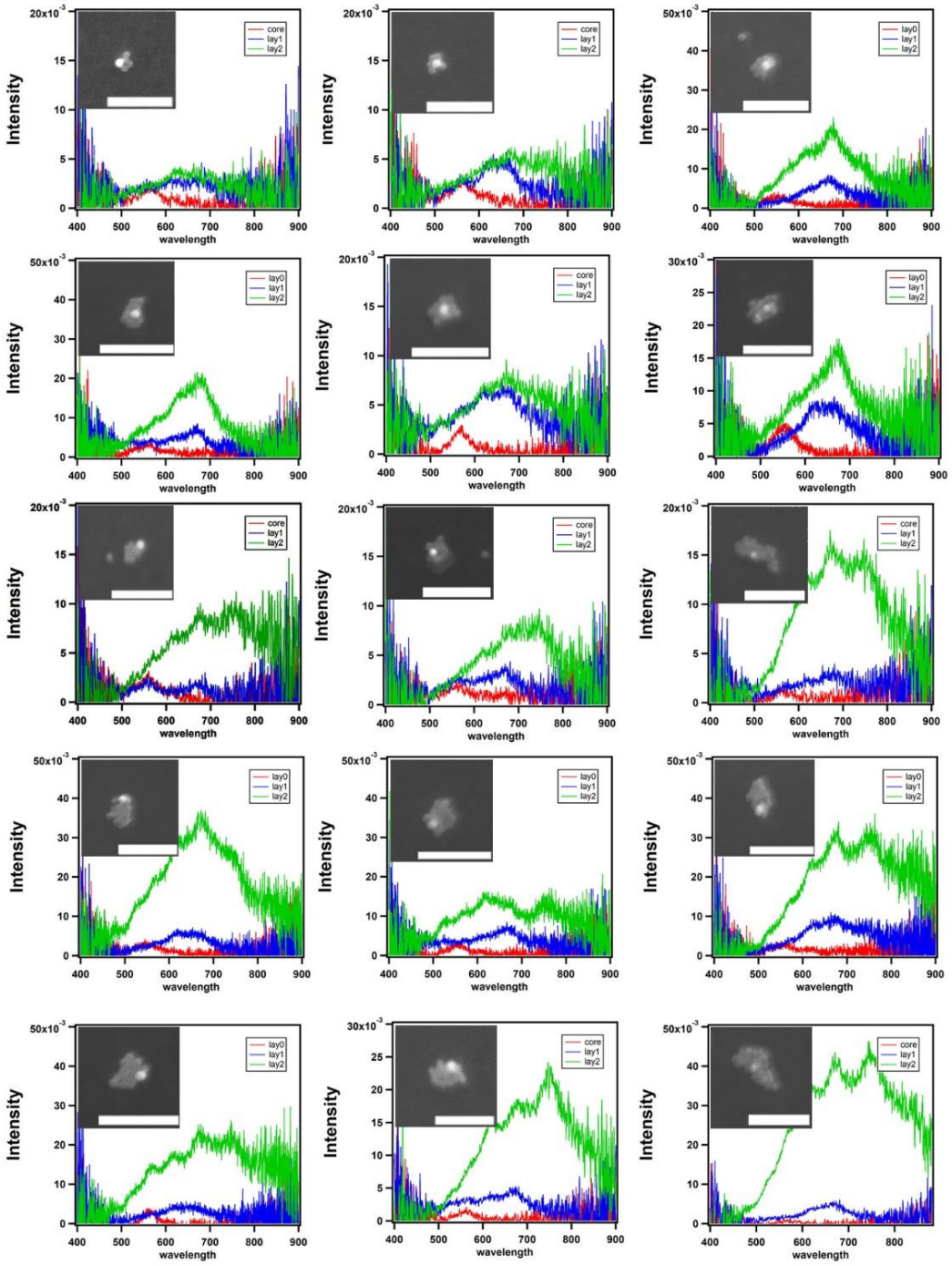

Figure 4.6. Additional correlated scanning electron microscopy (SEM) and single-nanostructure spectroscopy characterization of solid-shell assemblies. Scattering spectra of a single assembly with an increasing number of layers of satellite nanoparticles: red, 0-satellite layer; blue, 1-satellite layer; and green, 2-satellite layers. Inset shows SEM image after 2 layers of assembling. Scale bar: 500 nm.

4.3.4 Darkfield Imaging and Color Analysis

Next, we compare the colorimetric optical response of solid-shell vs solid-solid assemblies in the darkfield images. For solid-solid assemblies, the darkfield images evolve from dimly green scatterers (Figure 4.7a-b), corresponding to single solid core AuNPs (60 nm), to bright yellow scatterers upon the attachment of solid satellite NPs (Fig. 4.7c), consistent with previous reports.[15,35] In contrast, bright reddish scatterers were observed upon hybridizing with Au nanoshells (Figure 4.7d). The assemblies with two layers of Au satellite nanoshells were most distinguishable in darkfield images. We extrapolated the scattering intensity of each assembly from

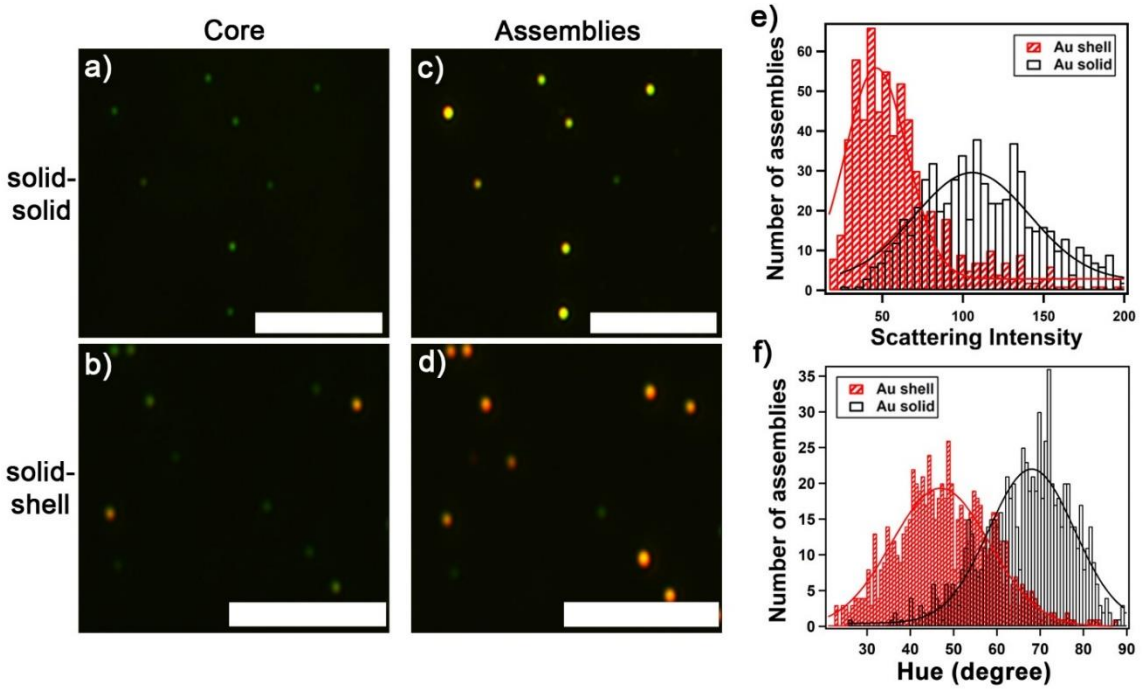

Figure 4.7. Darkfield microscopy characterization of solid-solid vs solid-shell assemblies. Darkfield images of 60-nm core AuNP (a, b) and after three cycles of layer-by-layer assembly with (c) 30-nm solid AuNP, or (d) 45-nm decahedral nanoshells. (e) Distribution of scattering intensity of solid-solid (N=645) vs solid-shell (N=641) assemblies obtained from darkfield image extrapolation. (f) Color distribution, expressed as hue in degrees, of light scattered by solid-solid (N= 750) vs solid-shell (N=735) assemblies. Distributions were obtained from three independent samples and fits are Gaussian distributions. Scale bar: 10 µm.

darkfield images, which enable high-throughput analysis. Figure 4.7e shows the distribution of the scattering intensity of 645 assemblies with solid satellite NPs and 661 assemblies with Au satellite nanoshells. Because of the limited sensitivity of the camera at the long wavelengths, the intensity of the solid-shell assemblies captured was low. We analyzed the scattering light color of single plasmonic assemblies using the HSI (hue, saturation, intensity) model,[36] where the hue value describes the color in the form of an angle ranging from 0 to 360 degrees corresponding to the color wheel that spans from red (0 degrees) to magenta (300 degrees). The distributions of the color, expressed in hue, for 750 solid-solid assemblies and 735 solid-shell assemblies are shown in Figure 4.7f. When fitted to Gaussian distributions, the hue value of the solid-solid assemblies is centered at 68 degrees scattering yellow compared to 46 degrees for the solid-shell assemblies scattering reddish color. With the hue value of the core AuNP centered at 84 degrees, a greater color change, as indicated by a larger magnitude in ΔHue, between the assembled and disassembled (i.e. core AuNP) structures is obtained for the solid-shell assemblies (|ΔHue| = 49 degrees) in comparison with solid-solid assemblies (|ΔHue| = 27 degrees)The difference in the colorimetric response of solid-solid vs solid-shell assemblies opens the opportunity for the development of color-coded multiplexed chip-based sensors.

4.3.5 Sensing ATP via Disassembly

We examined the detection of the model target ATP using the solid-shell assemblies. All sensing data were obtained from darkfield image analysis. Figure 4.8a,b shows the darkfield images of solid-shell assemblies in the buffer and 200 mM of ATP, respectively. The aptamer undergoes a structural change upon ATP binding, leading to the dehybridization of the linkers, the

disassembly of the structure, and a decrease in the scattering intensity.[15,35] Notably, the color of the scattered light changes from red to green for solid-shell assemblies upon disassembly, which is more prominent than solid-solid assemblies (i.e. yellow to green). We examined both the scattering intensity and the hue values of the assemblies at various concentrations of ATP from the pixels of darkfield images to establish the calibration curves in Figure 4.8c. We fitted the calibration curves to a one-site binding hyperbola model, assuming that the two binding sites of the aptamer are equal, to obtain apparent dissociation constants (K_d) of 14 mM and 18 mM for detection based on intensity and hue, respectively (Table 4.2). The apparent dissociation constant of solid-shell assemblies is higher than of solid-solid assemblies (1.9 mM). This difference may

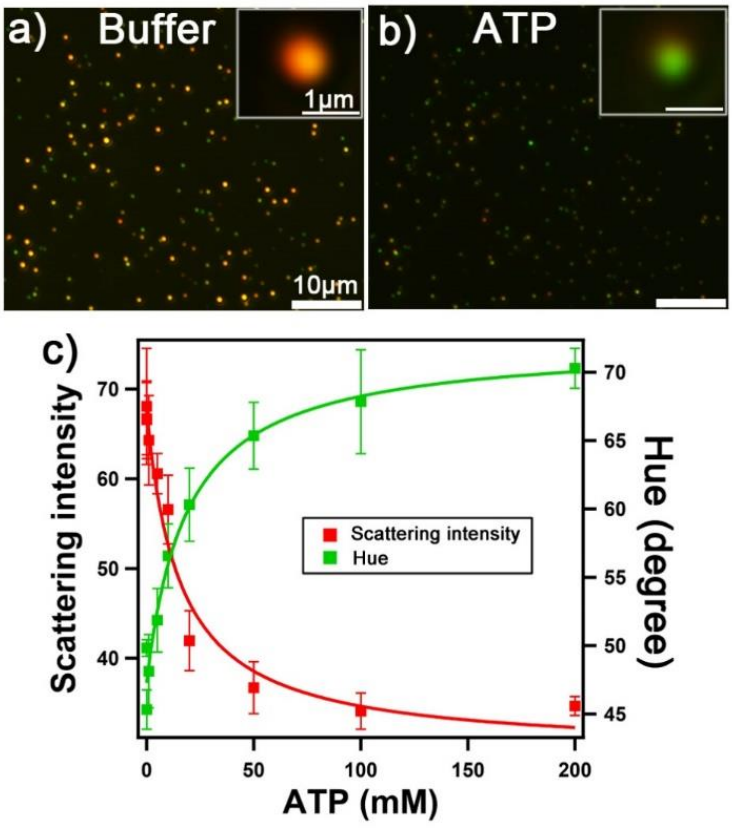

Figure 4.8. Disassembly process for sensing ATP monitored by darkfield microscopy. Darkfield images of solid-shell assemblies in (a) buffer and (b) with 200 mM ATP. (c) Concentration dependence of scattering intensity and hue. Error bars are standard deviations of triplicate samples.

Table 4.2. Fitted parameters of calibration curves in Figure 4.8 to the equation $y = y_0 + a\frac{xK_{[\,]}}{1+xK_{[\,]}}$

NPs	Fitted parameters			Detection limit (mM)**	s of image intensity*
	$K_{[\,]}$	y_o	a		
Solid-solid assembly (int.)	0.53	98.2 ± 1.7	-60.4 ± 2.3	0.23	3.7
Solid-shell assembly (int.)	0.07 ± 0.01	74.0 ± 1.3	-42.3 ± 2.0	0.27	3.3
Solid-shell asembly (Hue)	0.05 ± 0.01	47.3 ± 0.9	24.9 ± 1.6	0.48	3.5

** s is the standard deviation of the image intensity between replicates of experiments*

***LOD was calculated based on the signal of I_o - 3s*

have arisen because of the higher loading of DNA on nanoshells, where we measured a 2.3- and 3.2-fold increase for Seq 1 and Seq 2, respectively (see Table 4.1). The limit of detection (LOD) for solid-shell assemblies, calculated from three times the standard deviation of either the scattering intensity or hue of the blank, is 3.2 mM and 3.7 mM respectively. Analysis based on intensity over hue is preferred because it is faster, has higher sensitivity, and is more straightforward. Additionally, using scattering intensity as the detection signal further eliminates potential redshift effects arising from molecular adsorption (i.e. refractive index changes). The physiological level of ATP of interest is in the range of 0.1 to 3.0 mM,[37] which coincides with the most sensitive part of the calibration curve. Further improvements on the detection limit may be achieved by tuning DNA density,[38] splitting nucleic fragments,[39] or modifying the target binding site.[40]

4.4 Conclusions

We demonstrated tunable optical properties of plasmonic core-satellite NP assemblies by incorporating Au nanoshells as satellites. Plasmon hybridization was tuned by changing the morphology and the number of satellites decorated on a single core, as studied experimentally and theoretically. Plasmon coupling between the Au solid core and Au shell satellites leads to enhanced

scattering intensity and LSPR peak beyond 650 nm. The detection of ATP was achieved through target-induced dehybridization of DNA linkers and by analyzing changes in the scattering intensity or color of the plasmonic structures in darkfield images. We envision that the development of plasmonic sensing chips based on highly scattering single nanostructures, when coupled with the portable imaging system, may enable simple and low-cost bioanalysis. The solid-shell assemblies may also be of interest in other fields that seek to amplify the electromagnetic fields in the red or NIR wavelengths, such as surface-enhanced Raman scattering and solar energy conversion, and for in vivo applications where exploiting the NIR transparent window in biological systems is critical.

4.5 Methods

Materials

Colloidal solid quasi-spherical AuNP solutions were purchased from BBI Solutions. Illustra NAP-5 columns were purchased from GE Healthcare Life Sciences. Water used for all experiments was deionized to >18 MΩ using a Millipore system. Methoxy polyethylene glycols-succinimidyl valerate (mpeg-SVA) was purchased from LaysanBio. Sulfosuccinimidyl acetate was purchased from Thermo Fisher Scientific. 4-(2-hydroxyethyl)-1-piperazineethanesulfonic acid (HEPES), silver nitrate (99%), sodium citrate tribasic dihydrate (99.5%), L-arginine (98%), sodium borohydride (>99%), hydrogen peroxide with the potassium stannate inhibitor 30-32 wt.%, 99.999% trace metal basis, and tetrachloroauric acid (99%) were purchased from Sigma Aldrich. Poly(vinylpyrrolidone) (PVP, Mw = 40,000) was supplied by Caledon Chemicals (Caledon, Canada). Oligonucleotides were purchased from Integrated DNA Technologies. Thiolated DNA sequences were purified by HPLC.

DNA sequences for ATP detection:

Seq 1: 5'- T GAC ACC TTA_{10}-$(CH_2)_3$- SH- 3'

Seq 2: 5'- ACC TGG GGG AGT ATT GCG GAG GAA GGT GTC ACA A_{10}-$(CH_2)_3$- SH- 3'

Preparation of gold decahedral nanoshells

Gold nanoshells were prepared in a three-stage procedure by coating decahedral AgNPs with gold twice, adapted from the previously reported syntheses.[30,41] First, AgNP templates were prepared by combining 1.7 mM tricitrate, 0.05 mM PVP, 0.016 mM arginine, 0.13 mM silver nitrate, and 1.29 mM sodium borohydride in 14 mL of water in a 20 mL borosilicate glass vial under stirring with a magnetic stir bar (12.7 by 3.2 mm). After 1 hour of stirring at 400 rpm, the pale-yellow solution darkened, and 0.2 M hydrogen peroxide was added. Following the hydrogen peroxide addition, the solution bubbled for approximately 10 minutes, the stir bar was removed, the vial was capped, and then exposed to a 450 nm LED for 14 hours. Second, 10 mol. % Au plated AgNPs were prepared by adding 3 mL of a 0.013 mM solution of $HAuCl_4$ to 3 mL of the AgNP solution with a syringe pump at a rate of 0.25 mL/hour, under stirring (400 rpm with 12.7 by 3.2 mm stir bar). A 5-mL syringe attached to Teflon tubing (PTFE #18, AWG, Cole Parmer) with ethylene-vinyl acetate hot glue was used to dispense the gold solution from a KD Scientific pump. Finally, gold nanoshells, 80 mol. % Au relative to Ag in AgNPs, were prepared by adding the remaining 70 mol. % Au (0.09 mM $HAuCl_4$) by syringe under the same conditions as 10 mol.% Au coating

Functionalization of nanoshells with DNA

Seq 1- and Seq 2-functionalized 45-nm decahedral Au nanoshells were prepared from previously established method for ATP detection with modifications.[35] Briefly, a volume of 10-20 µL of purified oligonucleotides (with ~0.1 OD at 260 nm) was mixed with 100 µL of Au nanoshells for 30 min on a thermal shaker (40 °C, 650 rpm). A volume of 2 µL of 500 mM citrate buffer (pH 3) was added to lower the pH for 5 minutes and brought back to neutral by adding 20 µL of 500

mM HEPES (pH 7.4).[31] The NaCl concentration was slowly increased to 0.3 M at 0.1 M interval every 20 min. The sample was incubated for 4 h at 0.3 M NaCl. The DNA-AuNPs were washed three times with 0.01% SDS and stored in a buffer (0.01 M phosphate buffer (PB), 0.05 M NaCl, 0.01% sodium dodecyl sulfate (SDS), and 0.01% sodium azide) at 4°C. Seq 3- and Seq 4-functionalized 30-nm AuNPs were prepared for DNA-210 detection as previously established.[42]

Fabrication of core-satellite assemblies as chip-based sensors

The procedure was adapted from previously work[13] and briefly described below.

Deposition and DNA-functionalization of core AuNPs on an amino-modified substrate

A volume of 40 μL of 60 nm citrate-capped AuNPs (4.3 pM) was first placed on an aminopropyl-trimethoxysilane (APTMS)-treated coverslip for 2 minutes. The sample was rinsed and dried to yield anchored core AuNPs, which were then functionalized with Seq 1 using 10 μL of a solution containing 0.01 M PB, 0.4 M NaCl, 0.1% SDS, and DNA (2-5 μM) for 2 hours. The coverslip was rinsed with water and dried with compressed air.

To prevent non-specific binding of the satellite NPs on the amino-modified glass coverslip, the remaining amino groups were passivated using 5 mM mPEG-succinimidyl valerate solution in 0.1 M bicarbonate buffer (pH of 8.3) for 4 hours. Then the coverslip was treated with a 0.2 M solution of sulfo-NHS-acetate (sulfosuccinimidyl acetate, Thermo Scientific) in 0.1 M bicarbonate buffer (pH 8.3) for 4 hours. The sample was rinsed with water and dried with compressed air.

Layer-by-layer assembly of satellite nanoshells

To self-assemble the first layer of satellite NPs, a volume of 40 μL of Seq 2-Au nanoshells (30 pM) in 0.01 M PB, 0.32 M NaCl, and 0.01% SDS was incubated with core AuNPs immobilized on a coverslip for 60 min. The solution was replaced with buffer (0.01 M PB, 0.32 M NaCl) and the second set of satellite NPs, Seq 1-Au nanoshells, was added and incubated similarly. Each

layer of the assembly process was monitored by darkfield microscopy. The coverslip samples were stored in 0.01 M PB and 0.3 M NaCl at room temperature until sensing experiments.

Sensing Experiments

Sensing experiments were carried out in a sensing buffer of 0.01 M PB and 0.12 M NaCl. All samples were incubated at room temperature for at least one hour before the addition of analytes. Various volumes of a stock solution of 500 mM ATP in the sensing buffer were added to the sample to reach the specified concentration. Samples were incubated for a few minutes before dark-field images were collected.

Darkfield imaging, spectroscopy and analysis

Nanostructures in the sample area (100 x 100 μm^2) were visualized under darkfield using a Nikon TE-2000U inverted microscope fitted with a darkfield condenser at 60x objective magnification with an optional 1.5x lens. The microscope was connected to a CCD camera (Jenoptik) and a portable spectrometer (USB2000, Ocean Optics) via an optical fiber (diameter 100 μm). For single-nanostruscture scattering spectroscopy, a lamp reference spectrum was obtained by measuring defocused, scattered white light from a piece of kimwipe. The raw scattered spectrum of a nanostructure was measured at 90x magnification using custom Labview software and a PInano positioning stage (P-545, Physik Instrumente). The raw spectrum was subtracted by the dark spectrum and subsequently divided by the reference spectrum to yield the processed data. Darkfield images were captured at 60x magnification with an integration time of 200 ms and scattering spectra were measured at 90x magnification using custom Labview software and a PInano positioning stage (P-545, Physik Instrumente). The darkfield images were overlaid and converted to 8-bit JPEG grayscale. All image analysis was carried out using Igor as established previously. The coordinates of the center of the assemblies were identified by using the Localizer toolkit in Igor. The intensity of the surrounding 81 pixels for each assembly was averaged. For

color-code analysis, the RGB intensity was extrapolated from the original color darkfield images. The hue value of a pixel can be calculated from RGB information using the equation[36]

$H = \arctan\left(\frac{\sqrt{3}(G-B)}{(R-G)+(R-B)}\right)$. The average value of 81 pixels was calculated.

Finite-difference time-domain simulation

Theoretical modeling of the optical properties of the assembly was simulated using a three-dimensional finite-difference time-domain (FDTD) method with commercially available software (Lumerical FDTD Solutions, Ansys Lumerical Software ULC). All calculations were performed using a mesh size of 1 nm. The structures of the nanoshells were created by using a spherical Au particle overlaid with an etch material. Assemblies were created by randomly positioning 45-nm nanoshells of Au (with various shell thicknesses from 3 nm to 7 nm) around the top of a 60-nm diameter Au sphere. The distance between the closest particles was 10 nm.[13] Scattering spectra were simulated with a total-field scattered-field source for linearly polarized incident plane wave. Unpolarized spectra were obtained from the sum of the spectra with 0- and 90-degree polarizations. The background index was set to 1.33 simulating water.

Morphological characterization

A Quanta FEG 250 electron microscope operating at 10.0 kV at low vacuum (E-SEM mode) was used to obtained images at low magnification, and at high vacuum standard mode for correlative SEM-darkfield microscopy study. The assemblies were fabricated on an indium tin oxide-coated (ITO) substrate. A Quanta FEG 250 electron microscope operating at 10.0 kV in standard mode was used. The approximate locations of the solid-shell assemblies were identified via conductive ink markings at the edge of the substrate. A collage of darkfield optical images was captured for correlating the structures found in the SEM.

4.6 References

(1) Willets, K. A.; Van Duyne, R. P. Localized Surface Plasmon Resonance Spectroscopy and Sensing. *Annu. Rev. Phys. Chem* **2007**, *58*, 267–297.

(2) Cathcart, N.; Chen, J. I. L. Sensing Biomarkers with Plasmonics. *Anal. Chem.* **2020**, *92*, 7373–7381.

(3) Elghanian, R.; Storhoff, J. J.; Mucic, R. C.; Letsinger, R. L.; Mirkin, C. A. Selective Colorimetric Detection of Polynucleotides Based on the Distance-Dependent Optical Properties of Gold Nanoparticles. *Science (80-.).* **1997**, *277*, 1078–1081.

(4) Liu, J.; Lu, Y. Fast Colorimetric Sensing of Adenosine and Cocaine Based on a General Sensor Design Involving Aptamers and Nanoparticles. *Angew. Chemie Int. Ed.* **2006**, *45*, 90–94.

(5) Waldeisen, J. R.; Wang, T.; Ross, B. M.; Lee, L. P. Disassembly of a Core–Satellite Nanoassembled Substrate for Colorimetric Biomolecular Detection. *ACS Nano* **2011**, *5*, 5383–5389.

(6) Jun, Y.; Sheikholeslami, S.; Hostetter, D. R.; Tajon, C.; Craik, C. S.; Alivisatos, A. P. Continuous Imaging of Plasmon Rulers in Live Cells Reveals Early-Stage Caspase-3 Activation at the Single-Molecule Level. *Proc. Natl. Acad. Sci. U. S. A.* **2009**, *106*, 17735–17740.

(7) Xie, T.; Jing, C.; Long, Y. T. Single Plasmonic Nanoparticles as Ultrasensitive Sensors. *Analyst* **2017**, *142*, 409–420.

(8) Dijk, M. A. Van; Tchebotareva, A. L.; Orrit, M.; Lippitz, M.; Berciaud, S.; Van Dijk, M. A.; Tchebotareva, A. L.; Orrit, M.; Lippitz, M.; Berciaud, S.; *et al.* Absorption and Scattering Microscopy of Single Metal Nanoparticles. *Phys. Chem. Chem. Phys.* **2006**, *8*, 3486–3495.

(9) Sonntag, M. D.; Klingsporn, J. M.; Zrimsek, A. B.; Sharma, B.; Ruvuna, L. K.; Van Duyne, R. P. Molecular Plasmonics for Nanoscale Spectroscopy. *Chem. Soc. Rev.* **2014**, *43*, 1230–1247.

(10) Sagle, L. B.; Ruvuna, L. K.; Ruemmele, J. A.; Van Duyne, R. P. Advances in Localized Surface Plasmon Resonance Spectroscopy Biosensing. *Nanomedicine* **2011**, *6*, 1447–1462.

(11) Masson, J.-F. Portable and Field-Deployed Surface Plasmon Resonance and Plasmonic Sensors. *Analyst* **2020**, *145*, 3776–3800.

(12) Prodan, E.; Nordlander, P. Plasmon Hybridization in Spherical Nanoparticles. *J. Chem. Phys.* **2004**, *120*, 5444–5454.

(13) Nordlander, P.; Oubre, C.; Prodan, E.; Li, K.; Stockman, M. I. Plasmon Hybridization in Nanoparticle Dimers. *Nano Lett.* **2004**, *4*, 899–903.

(14) Sönnichsen, C.; Reinhard, B. M.; Liphardt, J.; Alivisatos, A. P.; Sonnichsen, C.; Reinhard, B. M.; Liphard, J.; Alivisatos, A. P. A Molecular Ruler Based on Plasmon Coupling of Single Gold and Silver Nanoparticles. *Nat. Biotechnol.* **2005**, *23*, 741–745.

(15) Le, N. H.; Nguyen, B. K.; Ye, G.; Peng, C.; Chen, J. I. L. Tuning the Sensing Performance of Multilayer Plasmonic Core-Satellite Assemblies for Rapid Detection of Targets from Lysed Cells. *ACS Sensors* **2017**, *2*, 1578–1583.

(16) Höller, R. P. M.; Dulle, M.; Thomä, S.; Mayer, M.; Steiner, A. M.; Förster, S.; Fery, A.; Kuttner, C.; Chanana, M. Protein-Assisted Assembly of Modular 3D Plasmonic Raspberry-like Core/Satellite Nanoclusters: Correlation of Structure and Optical Properties. *ACS Nano* **2016**, *10*, 5740–5750.

(17) Sebba, D. S.; Mock, J. J.; Smith, D. R.; LaBean, T. H.; Lazarides, A. A. Reconfigurable Core-Satellite Nanoassemblies as Molecularly-Driven Plasmonic Switches. *Nano Lett.* **2008**, *8*, 1803–1808.

(18) Sebba, D. S.; Labean, T. H.; Lazarides, A. A. Plasmon Coupling in Binary Metal Core-Satellite Assemblies. *Appl. Phys. B Lasers Opt.* **2008**, *93*, 69–78.

(19) Choi, I.; Song, H. D.; Lee, S.; Yang, Y. I.; Kang, T.; Yi, J. Core-Satellites Assembly of Silver Nanoparticles on a Single Gold Nanoparticle via Metal Ion-Mediated Complex. *J. Am. Chem. Soc.* **2012**, *134*, 12083–12090.

(20) Storhoff, J. J.; Lazarides, A. A.; Mucic, R. C.; Mirkin, C. A.; Letsinger, R. L.; Schatz, G. C. What Controls the Optical Properties of DNA-Linked Gold Nanoparticle Assemblies ? *J. Am. Chem. Soc.* **2000**, *122*, 4640–4650.

(21) Yoon, J. H.; Lim, J.; Yoon, S. Controlled Assembly and Plasmonic Properties of Asymmetric Core-Satellite Nanoassemblies. *ACS Nano* **2012**, *6*, 7199–7208.

(22) Yoon, J. H.; Zhou, Y.; Blaber, M. G.; Schatz, G. C.; Yoon, S. Surface Plasmon Coupling of Compositionally Heterogeneous Core-Satellite Nanoassemblies. *J. Phys. Chem. Lett.* **2013**, *4*, 1371–1378.

(23) Prodan, E.; Radloff, C.; Halas, N. J.; Nordlander, P. A Hybridization Model for the Plasmon Response of Complex Nanostructures. *Science* **2003**, *302*, 419–422.

(24) Zhao, J.; Pinchuk, A. O.; McMahon, J. M.; Li, S.; Ausman, L. K.; Atkinson, A. L.; Schatz, G. C. Methods for Describing the Electromagnetic Properties of Silver and Gold Nanoparticles. *Acc. Chem. Res.* **2008**, *41*, 1710–1720.

(25) Oldenburg, S. J.; Averitt, R. D.; Westcott, S. L.; Halas, N. J. Nanoengineering of Optical Resonances. *Chem. Phys. Lett.* **1998**, *288*, 243–247.

(26) Oldenburg, S. J.; Jackson, J. B.; Westcott, S. L.; Halas, N. J. Infrared Extinction Properties of Gold Nanoshells. *Appl. Phys. Lett.* **1999**, *75*, 2897–2899.

(27) Sheikholeslami, S.; Jun, Y. W.; Jain, P. K.; Alivisatos, A. P. Coupling of Optical Resonances in a Compositionally Asymmetric Plasmonic Nanoparticle Dimer. *Nano Lett.*

2010, *10*, 2655–2660.

(28) Wang, Y. C.; Rhéaume, É.; Lesage, F.; Kakkar, A. Synthetic Methodologies to Gold Nanoshells: An Overview. *Molecules* **2018**, *23*, 1–28.

(29) García-Soto, M. J.; González-Ortega, O. Synthesis of Silica-Core Gold Nanoshells and Some Modifications/Variations. *Gold Bull.* **2016**, *49*, 111–131.

(30) Rasch, M. R.; Sokolov, K. V; Korgel, B. A. Limitations on the Optical Tunability of Small Diameter Gold Nanoshells. *Langmuir* **2009**, *25*, 11777–11785.

(31) Cathcart, N.; Chen, J. I. L.; Kitaev, V. LSPR Tuning from 470 to 800 Nm and Improved Stability of Au-Ag Nanoparticles Formed by Gold Deposition and Rebuilding in the Presence of Poly(Styrenesulfonate). *Langmuir* **2018**, *34*, 612–621.

(32) Zhang, X.; Servos, M. R.; Liu, J. Instantaneous and Quantitative Functionalization of Gold Nanoparticles with Thiolated DNA Using a PH-Assisted and Surfactant-Free Route. *J. Am. Chem. Soc.* **2012**, *134*, 10–13.

(33) Jain, P. K.; Qian, W.; El-Sayed, M. A. Ultrafast Cooling of Photoexcited Electrons in Gold Nanoparticle-Thiolated DNA Conjugates Involves the Dissociation of the Gold-Thiol Bond. *J. Am. Chem. Soc.* **2006**, *128*, 2426–2433.

(34) Demers, L. M.; Mirkin, C. A.; Mucic, R. C.; Reynolds, R. A.; Letsinger, R. L.; Elghanian, R.; Viswanadham, G. A Fluorescence-Based Method for Determining the Surface Coverage and Hybridization Efficiency of Thiol-Capped Oligonucleotides Bound to Gold Thin Films and Nanoparticles. *Anal. Chem.* **2000**, *72*, 5535–5541.

(35) Le, N. H.; Ye, G.; Peng, C.; Chen, J. I. L. Metabolic Mapping with Plasmonic Nanoparticle Assemblies. *Analyst* **2020**, *145*, 2586–2594.

(36) Zhou, J.; Lei, G.; Zheng, L. L.; Gao, P. F.; Huang, C. Z. HSI Colour-Coded Analysis of Scattered Light of Single Plasmonic Nanoparticles. *Nanoscale* **2016**, *8*, 11467–11471.

(37) Traut, T. W. Physiological Concentrations of Purines and Pyrimidines. *Mol. Cell. Biochem.* **1994**, *140*, 1–22.

(38) Ghotra, G.; Nguyen, B. K.; Chen, J. I. L. DNA-Functionalized Gold Nanoparticles with Toehold-Mediated Strand Displacement for Nucleic Acid Sensors. *ACS Appl. Nano Mater.* **2020**, *3*, 10123–10132.

(39) Zhu, C.; Zhao, Y.; Yan, M.; Huang, Y.; Yan, J.; Bai, W.; Chen, A. A Sandwich Dipstick Assay for ATP Detection Based on Split Aptamer Fragments. *Anal. Bioanal. Chem.* **2016**, *408*, 4151–4158.

(40) Zhang, Z.; Oni, O.; Liu, J. New Insights into a Classic Aptamer: Binding Sites, Cooperativity and More Sensitive Adenosine Detection. *Nucleic Acids Res.* **2017**, *4567*, 2–10.

(41) Murshid, N.; Keogh, D.; Kitaev, V. Optimized Synthetic Protocols for Preparation of

Versatile Plasmonic Platform Based on Silver Nanoparticles with Pentagonal Symmetries. *Part. Part. Syst. Charact.* **2014**, *31*, 178–189.

(42) Ghotra, G.; Le, N. H.; Hayder, H.; Peng, C.; Chen, J. I. L. Multiplexed and Single-Cell Detection of MicroRNA with Plasmonic Nanoparticle Assemblies. *Can. J. Chem.* **2021**, *99*, 585–593.

Chapter 5- Multiplexed Detection with Plasmonic Nanoparticle Assemblies

Parts of this chapter have been published in:

1. Ghotra, G.; Le, N.H.; Hayder, H.; Peng, C.; Chen, J. I. L. *Can. J. Chem*. **2021**, 99, 585–593. The part of the publication on duplexing using solid-solid AuNP assemblies is presented herein.
2. Le, N. H.; Cathcart, N.; Kitaev, V.; Chen, J. I. L. Analyst **2022**, 147, 155-164. The part of the publication on duplexing using solid-solid and solid-shell AuNP assemblies is presented herein.

The work on developing the linkers for DNA-210 detection was carried out by Gurbrinder Ghotra. All experiments presented on multiplexing were carried out by Nguyen Le, including detailed optimizations that were not published.

5.1 Abstract

The detection platform based on core-satellite nanostructures has been developed for targets including proteins, nucleic acids, and metabolites. Here we present multiplexed detection using the assemblies for two different biomolecular targets – adenosine triphosphate (ATP) and a nucleic acid target (DNA-210). We modified the layer-by-layer assembly to enable the fabrication of a mixture of DNA-linked nanostructures on a common area. The duplexed assay was demonstrated by the selective detection of the two targets via disassembly. Furthermore, the optical properties of core-satellite assemblies can be tuned by using different nanoparticle morphologies. Two types of core-satellite nanostructures, comprising either solid core and solid satellite, or solid core and shell satellite, were fabricated with different linkers; the different scattered colors allowed us to identify the sensors for the different targets. We demonstrate the feasibility of multiplexing

based on the change in the scattering intensity and the color read-out. This methodology may be applied to the quantification of different analytes in the cellular microenvironment. In combination with portable imaging devices, the chip-based multiplex sensing platform may enable on-site detection as well as be a cost-effective analytical tool in resource-limited laboratory settings.

5.2 Introduction

A multiplexed assay allows for the simultaneous detection of multiple analytes, which is desirable for research and clinical applications. For example, measuring multiple targets in a single sample can reduce the sample volume, improve cost efficiency, and acquire a greater amount of information from a single experiment.[1,2] Multiplexed assays of proteins[3,4] and nucleic acids[5] are widely used in the biological and biomedical fields. Studies of genomics and proteomics generate an escalating number of sequence data and are facilitated by high-throughput detection and screening technologies. There are two commonly used multiplex assay formats – a conventional microarray or a suspension array. In a conventional microarray, specific probes are immobilized on a solid surface with a predetermined spatial location. The assay is commonly incorporated with an optical readout for quantitative analysis. The microarray technology can detect hundreds to thousands of different targets simultaneously. For example, a nucleic acid-based microarray can detect more than one thousand microRNAs[6] at once, and even proteins[7] if aptamers are employed. These assays are invaluable for biomarker discovery.[8] In contrast, a suspension array employs micro-beads or nanoparticles encoded by embedded fluorescent dye or quantum dots (QDs), with surface functionalization of antibodies or nucleic acid aptamers for the specific targets. For example, fluorescent dyes can be embedded into a polystyrene or silica microsphere to form a barcode bead. By entrapping different ratios of dyes into the microspheres to obtain optically distinct populations, there are more than 100 different bead sets commercially available – the

common product known as Luminex.[9] The Luminex assay uses a combination of fluorescent beads with flow cytometry to yield high multiplexing capabilities for proteins.[10] Conventional experiments utilize multiple organic dyes to code different analytes in a single experiment, but identification may be difficult because of spectral overlap and cross-talk among the different dyes and also the challenges in achieving and maintaining the brightness and stability of the fluorophores. Alternatively, QDs are semiconductors that have been used as a replacement for organic dyes because of broad excitation, narrow and tunable size-dependent emission spectra.[1,11] Due to the quantum confinement effect for particles of very small (<10 nm) dimensions, the excitation and emission peaks of QDs can be easily modulated from visible to NIR region by changing the QD diameters. A mixture of QDs of different colors can be simultaneously excited using a single wavelength, enabling for multiplexed assay. For instance, QDs with different colors were applied for the detection of three biomarker miRNA-20a, miRNA-20b, and miRNA-21 simultaneously from a sample.[12] When embedded into polystyrene microspheres, the barcoded QD beads yield multiple colors with a high level of brightness and even several intensity levels. Thus QD-polystyrene beads could potentially code up to 10,000 – 40,000 nucleic acid or protein sequences (based on the relationship intensity^{color}-1).[13] The mixture of QDs microbeads can be immobilized on a glass substrate and used as codes to simultaneously detect multiple DNA biomarkers, from infectious pathogens such as HIV, hepatitis B and C, and influenza. The assay can then be combined with a smartphone for the feasible design of a low-cost multiplexed assay.[14] However, there exists two major problems with the QD semiconductor materials – the potential human toxicity and cytotoxicity – that could impede its applications especially *in vitro* or *in vivo*.[15]

Plasmonic NPs can potentially compete with conventional optical transducers because of their advantages such as higher photostability than organic dyes, as well as chemical and biological

stability and noncytoxicity. In addition, LSPR-based assay has the advantage of requiring no specialized instrumentation and being low cost,[16] which could offer diagnostic capability at places where resources are limited, such as developing countries.[17] Plasmonic nanoparticles such as gold nanorods exhibit precisely tunable optical properties with the aspect ratios (length divided by width);[18–20] accordingly, gold nanorods have been explored for multiplexing capability either in suspension array or microarray.[21–23] Yu *et al.* utilized nanorods of three different aspect ratios to yield optical channels that are separated based on the LSPR wavelengths. A mixture of different nanorods was employed for simultaneous detection of three different antibodies in a buffer solution,[22] and then adapted to detect three cell surface markers to profile the phenotypes of cells.[21] In other studies, an LSPR microarray chip comprising of gold nanorods was used for the detection of six different cytokines in the serum matrix.[23] Besides a single nanostructure, complex nanostructures have been attracting attention because of field enhancement that is inherent from plasmon coupling.

Recently, researchers have developed optical detection platform based on complex core-satellite nanostructures for a variety of targets such as proteins, nucleic acid, and small biomolecules. As shown in previous chapters, the detection can be achieved through the optical change upon disassembly of the nanostructure, leading to dramatic changes in the light-scattering properties. This detection platform based on single plasmonic nanostructures and darkfield microscopy presents a simple, rapid, and straightforward method with high sensitivity and the potential for portability and reusability. However, previously reported chip-based nanoparticle assays have limited multiplexing capabilities. Here, we establish a multiplexing strategy for the detection of nucleic acid and adenosine triphosphate (ATP) species simultaneously on a two-dimensional substrate using plasmonic nanoparticle assemblies.

Besides ATP as the target,[24] our group adapted the assemblies for detecting a nucleic acid biomarker, miRNA-210, by engineering the DNA linkers to undergo a strand displacement reaction.[25] Our multiplexing approach is to fabricate two different types of assemblies for targeting either ATP or miRNA-210 on a common area through a layer-by-layer process. The method of fabrication and sequence designs were first optimized. As a step further for multiplexing, the tunable optical properties of nanostructures with different morphologies, presented in Chapter 4, was incorporated to expand the sensing platform toward automated imaging processing and data analysis. Our work can open the door to the analysis of different biomolecules in minute sample sizes and heterogeneous biological specimens.

5.3 Results and Discussion

5.3.1 The Working Principle of Duplexed Sensors

The common approach for multiplexing is through the fabrication of arrays; however, because our sensing platform is based on individual plasmonic nanostructures, a mixture of assemblies can be employed on a common sensing area. Multiplexing was achieved by

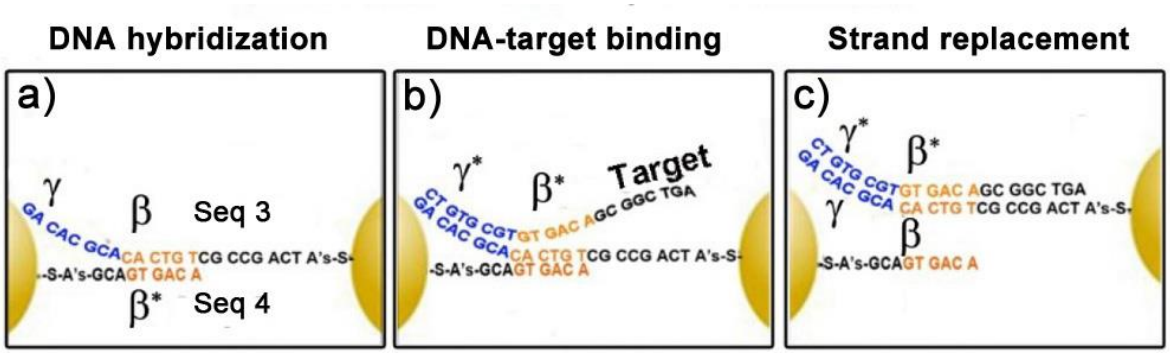

Figure 5.1. Toehold-Mediated Strand- Displacement Process for DNA on AuNPs. (a) DNA hybridization between Seq 3 and Seq 4 with 6 base-pair complement denoted as β and β^*. γ represents the sticky end toehold on Seq 3. (b) DNA target first binds to toehold regions and then strand migration leads to the complete displacement of Seq 4 (c).

constructing plasmonic nanoparticle assemblies targeting two different biomolecules: (i) ATP which was developed previously using a structural-switching aptamer[28–30] (see Chapter 2, 3 and 4) and (ii) DNA-210, the deoxy analog of microRNA-210 (denoted as miR-210), which is a regulator of numerous biological processes including cell proliferation, apoptosis, differentiation, angiogenesis, and mitochondrial metabolism.[31] Our group recently established the detection platform of miR-210 using core-satellite assemblies by incorporating DNA linkers that undergo the strand displacement reaction,[25] in which single-stranded DNA displaces a double-stranded DNA through the migration process and the reaction is initiated by a short sticky end, known as the toehold.[32,33] Figure 5.1 illustrates the strand displacement reaction for the DNA-210 target with the sticky end toehold sequence (denoted as γ). The duplex hybridization between Seq 3 and Seq 4 through the partial complement of six bases (β and β^* domain) can be displaced by DNA-210 through hybridization initiated at the toehold domain (γ) on Seq 3.

5.3.2 DNA Cross-Hybridization Challenge

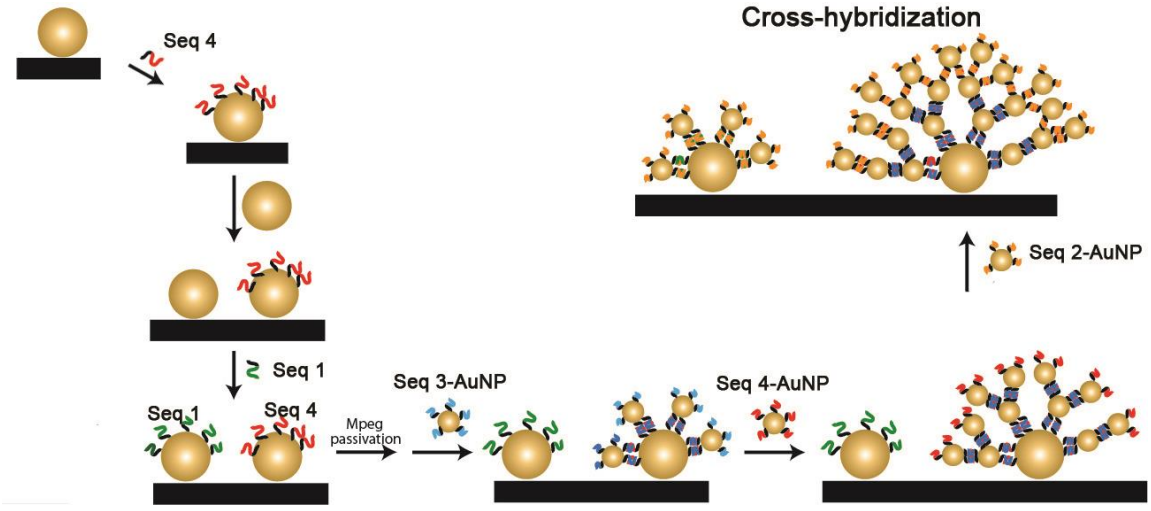

Scheme 5.1. Fabrication of duplex sensors in a common area. Core NPs were functionalized with either Seq 4 or Seq 1, for DNA-210 and ATP respectively.

Our initial plan was to directly adapt the layer-by-layer assembly in a stepwise process to yield duplexed sensors. Scheme 5.1 depicts the fabrication of the two different targeting assemblies on the same sensing area, where DNA-210-targeting assemblies were constructed first, followed by the preparation of ATP-targeting assemblies. However, initial trials showed the cross-hybridization between Seq 2-AuNP (for ATP sensor) and Seq 4-AuNP (for DNA-210 sensor); refer to the last step in Scheme 5.1. This issue was identified when we monitored the fabrication process using darkfield microscopy. Figure 5.2b shows the increase in the scattering intensity, compared with Figure 5.2a of the core NPs, when DNA-210-targeting assemblies were formed (green outlines). When we tried to build up the second set of the assemblies (for ATP sensing), an unexpected increase in the scattering intensity of both types of assemblies was observed (Fig. 5.2c).

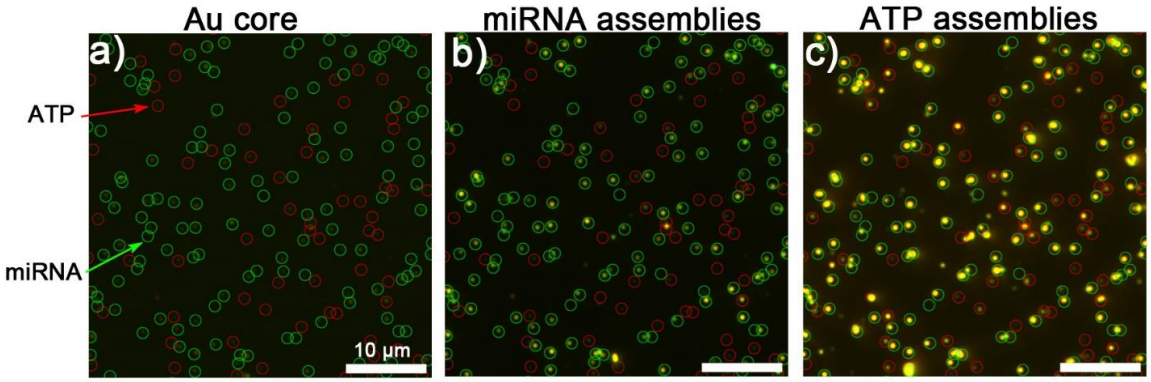

Figure 5.2. Monitoring optical properties of during the fabrication of duplexed sensors. Darkfield images of the assembly process: (a) core AuNPs functionalized with two sequences of DNA (green outlines for DNA-210 and red outlines for ATP); (b) after a two-layer buildup of core-satellite DNA-210 assemblies; and (c) after a three-layer buildup of core-satellite ATP assemblies in parallel with the cross-hybridization of DNA-210 assemblies.

Upon careful examination, there exists partial complementarity between Seq 4 (for ATP) and Seq 2 (for DNA-210). Scheme 5.2 illustrates the cross-hybridization between Seq 4 and Seq 2 strands with 6 complementary base-pairs, leading to the unintended self-assembly of the DNA-210 sensor with the satellite NPs designed for the ATP sensor. This issue may be overcome by redesigning new DNA linkers or introducing complementary DNA to cap parts of the existing strands on NPs to prevent cross-hybridization.

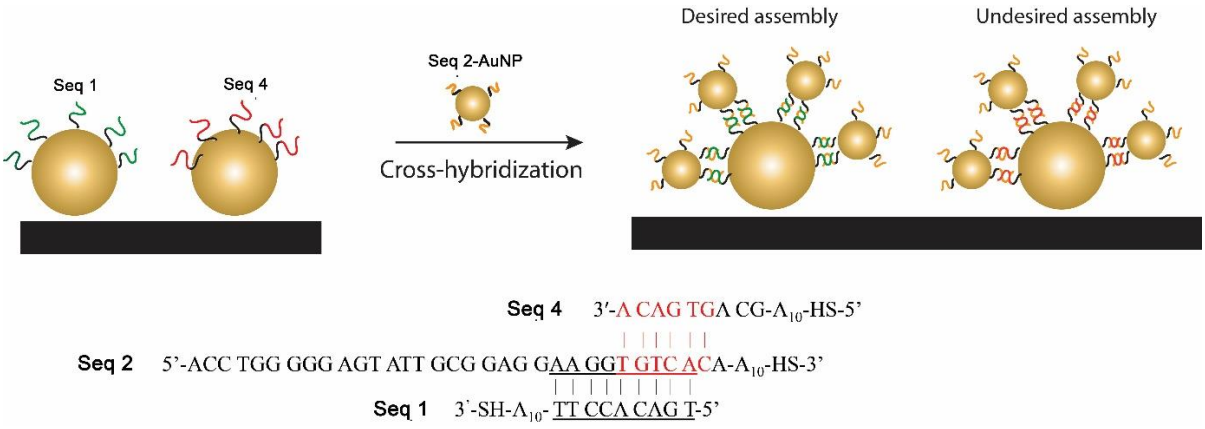

Scheme 5.2. Undesirable cross-hybridization between DNA Seq 2 and Seq 4 that leads to unselective assembly process. Seq 2 was designed to be hybridized with Seq 1.

5.3.3 Effect of Capping Sequence on DNA Cross-Hybridization.

We examined the cross-hybridization of Seq 4- and Seq 2-functionalized satellite NPs in solution. Scheme 5.3 depicts the aggregation of Seq 4- and Seq 2-satellite NPs and the strategy of introducing a cap sequence (Seq 5) to Seq 4-AuNPs to prevent cross-hybridization. We hypothesized that cross-hybridization can be overcome if free Seq 4 strands on AuNPs are unreactive. Figure 5.3a shows the LSPR absorbance spectra upon mixing Seq 2- and Seq 4-functionalized AuNPs. The LSPR peak red-shifted, dampened, and broadened over time, indicating the cross-hybridization between satellite NPs of different sensors and their aggregation. We then incorporated the cap Seq 5 to Seq 4-AuNP first before incubation with Seq 2-AuNPs. Figure 5.3b compares the changes in the LSPR: there was a negligible change when Seq 5 cap was included (black curve) vs a significant drop for Seq 2- and Seq 4-AuNPs without Seq 5 (red curve). It should be noted that the introduction of Seq 5 did not affect the hybridization of Seq 1- and Seq 2-AuNPs for the ATP sensor, as shown by the green curve in Fig. 5.3b. The results suggest that Seq 5 cap is effective at preventing cross-hybridization, while not interfering with the hybridization of ATP-targeting linkers. The introduction of complementary capping DNA is a

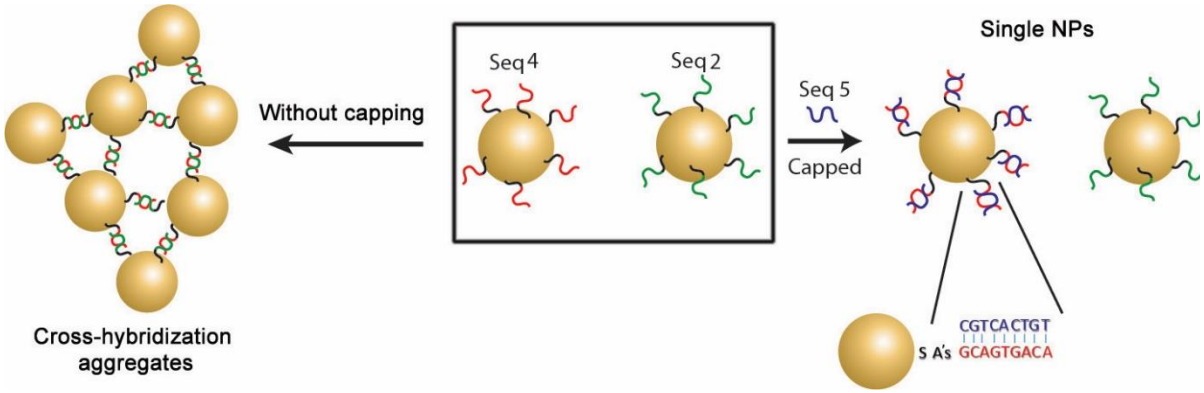

Scheme 5.3. Strategy to prevent the cross-hybridization of satellite NPs for different sensors. Seq 5, the capping DNA, has a complementarity of nine bases to Seq 4; the hybridization between Seq 5 and Seq 4 prevents the cross-hybridization between Seq 4 and Seq 2.

critical step for the fabrication of duplex assemblies through the stepwise layer-by-layer assembly on the substrate experiments, as detailed below.

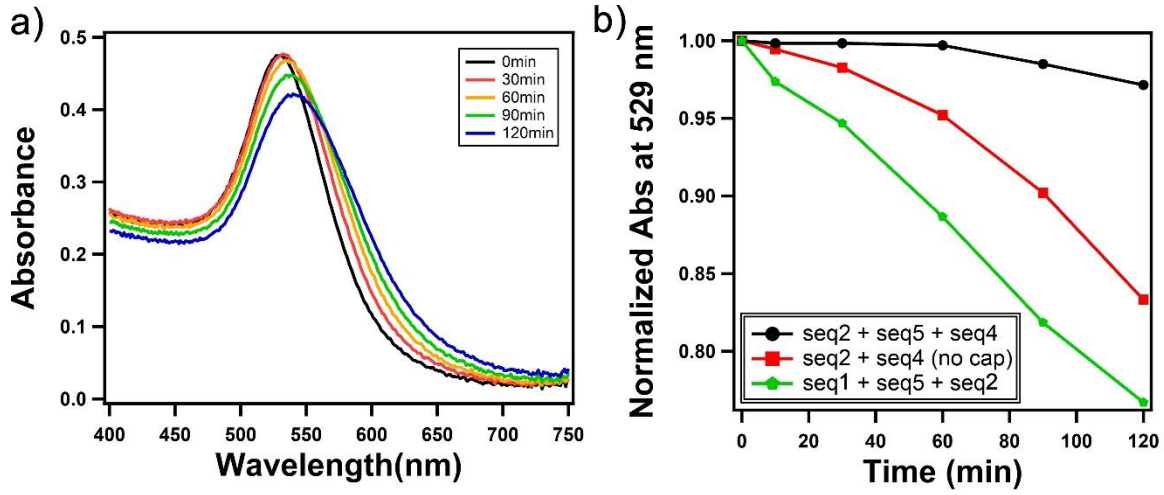

Figure 5.3. (a) Evolution of the absorbance spectra during the aggregation of DNA-AuNPs due to the cross-hybridization between Seq 2 and Seq 4. (b) Plots of the change in absorbance at 529 nm over time illustrating colloidal aggregation: Seq 2- and Seq 4-functionalized AuNPs without Seq 5 (red curve); Seq 5 on Seq 4-AuNPs before introducing Seq 2-AuNPs (black curve); Seq 1-AuNPs mixed with Seq 5 before introducing Seq 2-AuNPs (green curve).

5.3.4 Fabrication of Duplexed Sensors Using Solid-Solid Gold Nanoparticle Assemblies

Scheme 5.4 depicts the optimized method for fabricating two different targeting assemblies on the same sensing area, with the incorporation of Seq 5. The darkfield images captured after each step were used to delineate the nanostructures targeting the two biomolecules as shown in Figure 5.4. The core NPs thiolated with the different types of DNA sequences were firstly immobilized on ATPMS-silanized glass and followed by the layer-by-layer buildup to yield DNA-210 targeting assemblies (Figure 5.4b). Prior to assembling ATP sensors, we introduced the cap DNA (Seq 5) to hybridize free Seq 4 strands on the DNA-210-targeting structures. The layer-by-layer assembly with Seq 2- AuNP and Seq 1-AuNP then yielded the ATP-targeting nanostructures (Figure 5.4c) without affecting those targeting DNA-210. Figure 5.4d summarizes the changes in the scattering intensity during each assembly step. The optical response of two different targeting assemblies was subsequently used for the demonstration of multiplexed sensing.

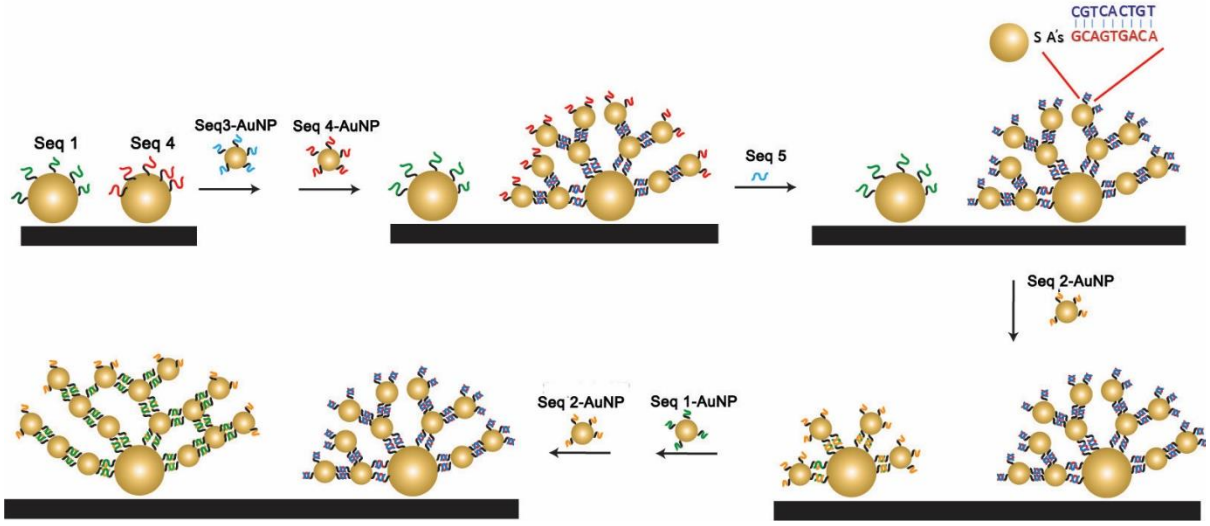

Scheme 5.4. Fabrication of duplex assemblies using Seq 5 as cap. The introduction of Seq 5 is essential for preventing the cross-hybridization.

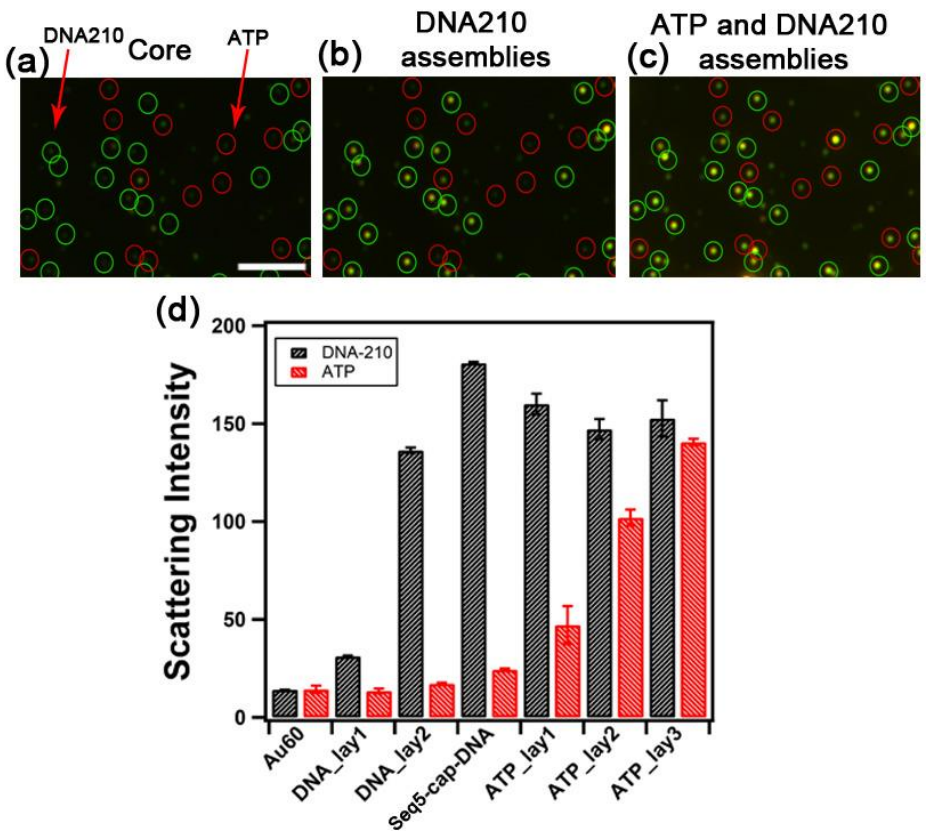

Figure 5.4. Darkfield images of the duplex assembly process: (a) core AuNPs functionalized with Seq 2 or Seq 3 (red outlines for DNA-210 and green outlines for ATP); (b) after two-layer buildup of core-satellite DNA-210 assemblies; and (c) after three-layer buildup of core-satellite ATP assemblies. (d) The scattering intensities of the two sets of assemblies during the fabrication process. The scale bar is 10 μm and the error bar represents the standard deviation of the mean of N=100 (DNA-210) and N=80 (ATP) assemblies.

5.3.5 Selective Disassembly

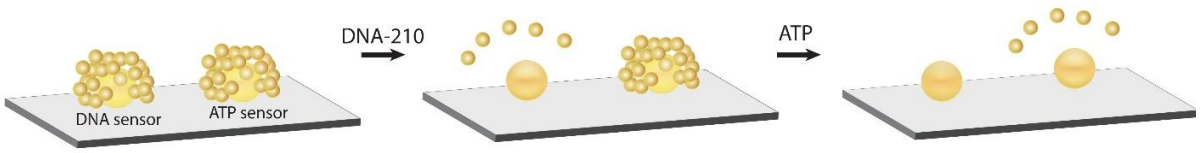

Scheme 5.5. Selective disassembly of duplex sensors of DNA-210 and ATP target fabricated on a sensing area.

We validated the selectivity and the sensing capability of the duplexed platform as illustrated in Scheme 5.5. Figure 5.5a shows the darkfield images of DNA-210- and ATP-targeting assemblies in the same area. When DNA-210 was introduced, only DNA-210-targeting assemblies (outlined in green) disassembled and exhibited a decrease in the scattering intensity as shown in Figure 5.5b; a negligible change in the scattering intensity was observed for ATP-targeting assemblies in the presence of DNA-210. The subsequent addition of ATP led to the disassembly of ATP sensors, as seen in Figure 5.5c. Figure 5.5d summarizes the changes in the scatteringintensity of the assemblies showing the selective response to the targets. We achieved

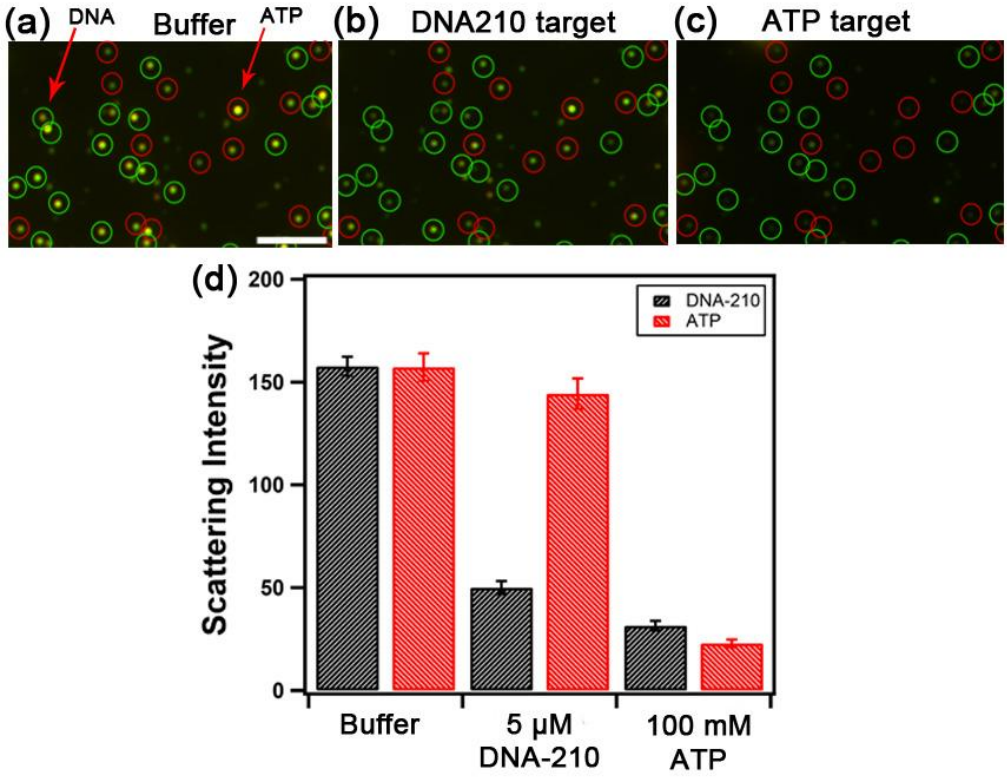

Figure 5.5. Duplexed sensing platform comprising DNA-210- and ATP-targeting assemblies. Darkfield images of the sequential sensing experiments: (a) duplex assemblies in buffer; (b) after incubation with excess DNA-210; and (c) after addition of excess ATP. (d) The scattering intensities of the two sets of assemblies in selective detection. The scale bar is 10 μm and the error bar represents the standard deviation of the mean of N=100 (DNA210) and N=80 (ATP) assemblies.

two different types of assemblies on a common sensing area to detect two different analytes selectively.

5.3.6 Multiplexing Using Different Morphology of Nanostructures

Building on the idea of multiplexing, we incorporated different morphologies of NP assemblies to tune the optical properties. The ability to tunable optical properties of NP assemblies with different building blocks was established (see Chapter 4). Herein, we demonstrate that NP assemblies of different morphologies (i.e. solid-solid and solid-shell) combined with the optimized linker chemistry can yield color-coded detection of DNA-210 and ATP. Figure 5.6a shows the darkfield images of the nanostructures targeting the two biomolecules, as outlined by green and red circles. Upon assembly, the optical properties of the two types of assemblies evolved differently and were distinguishable under darkfield microscopy as shown in Figure 5.6b. The solid-solid assemblies targeting DNA-210 exhibited bright yellow color, whereas ATP-targeting solid-shell assemblies displayed red or orange color. The difference in the scattered color results from the off-resonance coupling between the LSPR of different building blocks (see Chapter 4). We note that there are fractions of solid-shell and solid-solid assemblies displaying similarly bright yellow or red colors, likely because they are large and exhibit broad LSPR peaks. Nevertheless, a discernible difference in the scattered colors between most solid-solid and solid-shell assemblies was observed and was analyzed using the color-code method[27] as shown in Figure 5.6c. The initial hue values were 72 ± 4 degrees for solid-solid assemblies and 55 ± 3 degrees for solid-shell assemblies. This color difference in the initial scattering can be used as a color code to identify the targets in a mixture of NP assemblies. We extrapolated the scattering intensity of each assembly from darkfield images. Figure 5.6d shows the distribution of the scattering intensity of solid-solid (for DNA-210) and solid-shell (for ATP) assemblies with the initial scattering intensity values of

148 ± 6 and 68 ± 2, respectively. It should be noted that the intensity of the solid-shell assemblies captured was low due to the limited sensitivity of the camera at long wavelengths. The optical response of two different assemblies was subsequently used for multiplexed sensing.

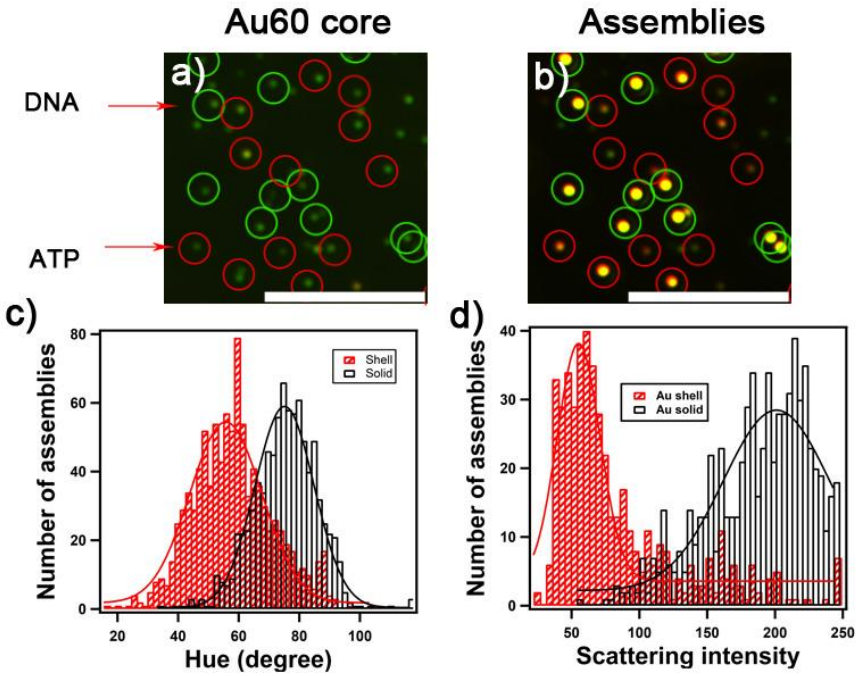

Figure 5.6. Monitoring the optical properties of duplexed sensors comprising DNA-210 (solid-solid) and ATP-targeting (solid-shell) assemblies. Darkfield images of (a) Au60 core NPs functionalized with two sequences of DNA (green outlines for DNA-210 and red outlines for ATP), and (b) after assembly Au solid and Au shell. (c) Distribution of scattering intensity of solid-solid (N=868) vs solid-shell (N=965) core-satellite assemblies obtained from image extrapolation, and (f) color distribution of light scattering by solid-solid (N= 691) vs solid-shell (N=478) assemblies expressed as hue in degrees. The scale bar is 10 µm.

Next, we examined the selectivity of the duplexed sensors. Figure 5.7a shows the darkfield images of DNA-210- and ATP-targeting assemblies in optimized buffer conditions in the same sensing area. Again, the introduction of DNA-210 only leads to the disassembly of DNA-210-targeting solid-solid assemblies (outlined in green) with a decrease in their scattering intensity from 154 to 53 (Fig 5.7d) and color change from yellow to green with an increased hue value from 69 to 83 (Fig 5.7e). The introduction of DNA-210 yielded a negligible change in the scattering

intensity and color of ATP-targeting Au shell assemblies (Figure 5.7b). The subsequent addition of ATP caused the disassembly of ATP sensors as shown in Figure 5.7c, where a decrease in the scattering intensity of ATP targeting assemblies (Fig 5.7d) and an increase in the hue value from 55 to 72 (Fig 5.7e) was observed. Figure 5.7d,e summarizes the changes in the optical properties

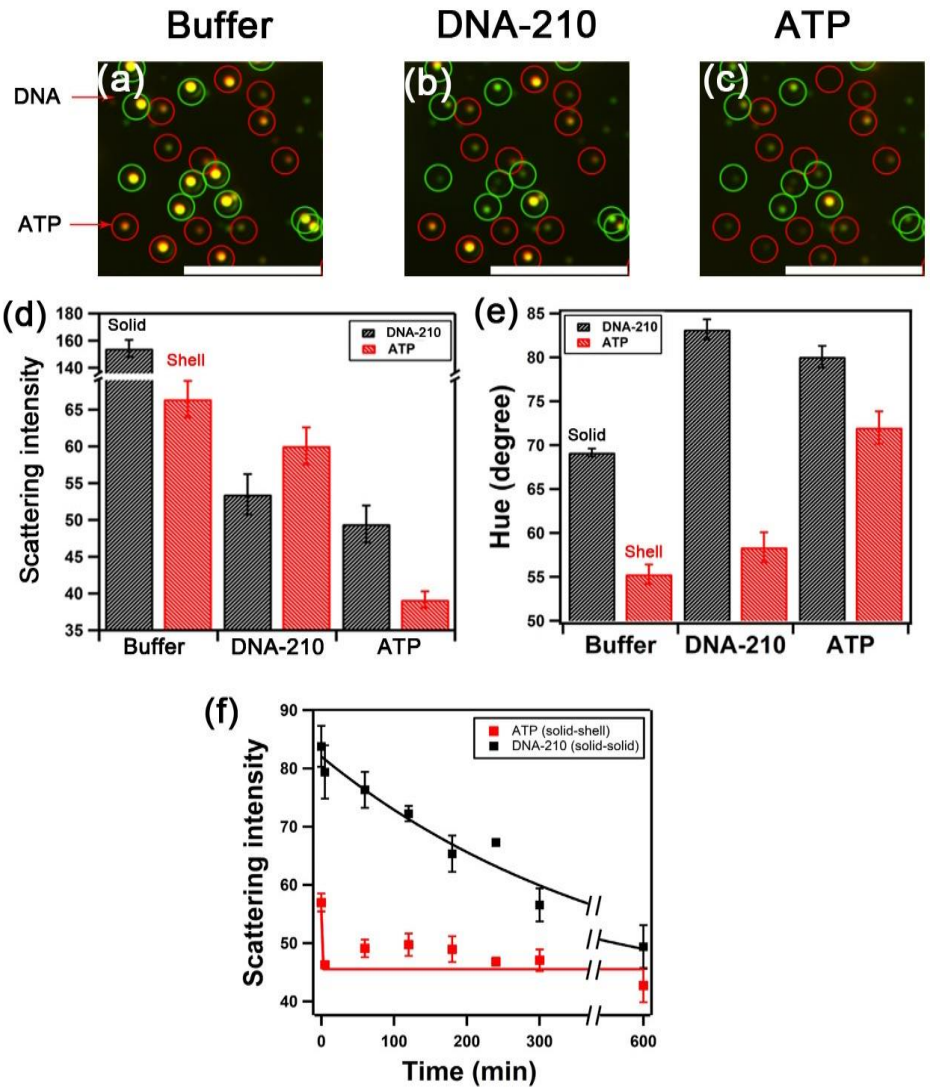

Figure 5.7. Duplexed sensing platform comprising DNA-210 (solid-solid) and ATP-targeting (solid-shell) assemblies. Darkfield images of sensing experiment: duplexed assemblies (a) in buffer; (b) after incubation with excess DNA-210; and (c) after addition of excess ATP. (d) Scattering intensity analysis and (e) color-code analysis of the two classes of assemblies upon the addition of DNA-210, followed by ATP. Error bars are standard deviations of replicate experiments. (f) Kinetics of disassembly of the duplex assemblies in 0.10 M NaCl phosphate buffer containing a mixture of the targets. The scale bar is 10 μm.

of the assemblies confirming the selective response to the targets and the quantification is possible by using previously established calibration curves (see Chapter 3). Furthermore, Figure 5.7f shows the time-dependent scattering signal of the duplex sensor in a mixture of ATP and DNA-210 at a buffer composition that maximizes the kinetics difference: the scattering intensity of the ATP solid-shell assemblies exhibited a fast decrease in contrast with the long decay of the DNA-210-targeting solid-solid assemblies. This finding demonstrates that the kinetics of disassembly of the two types of structures by a small molecule ATP compared with a nucleic acid for strand-displacement can provide another path for differentiation. By tuning the optical properties with different morphologies of satellite NPs, the discrete NP assemblies with different colors can serve as barcodes for a colorimetric assay. Our work presents the opportunity to develop multiplex chip-based plasmonic sensors combining different morphologies and biomolecular linker design.

5.4 Conclusion

We demonstrated multiplexed detection of ATP and DNA-210 targets using plasmonic nanoparticle assemblies. Through the layer-by-layer process using DNA linkers, the core-satellite NP assemblies for different targets can be fabricated on the same sensing area. We addressed the issue of cross-hybridization between DNA linkers by employing a cap DNA sequence, which is important when the design of the linkers is constrained by the targets. The duplexed assay demonstrated the selective detection of ATP and a nucleic acid target based on changes in the scattering intensity. Furthermore, by using solid-solid and solid-shell assemblies, we can achieve distinguishable color scatters to color-code the sensors. These color-coded nanostructures may be further developed to implement automated darkfield image analysis and as alternative barcode technologies of dyes and QDs. The methodology of fabricating multiplexed assemblies on the same sensing area opens the door to designing linkers targeting different microRNAs or proteins

for biomarker profiling. Additionally, this chip-based assay may also provide an alternative platform to elucidate multiple biomolecules in the cellular microenvironment.

5.5 Methods

Materials

Colloidal AuNP solutions were purchased from BBI Solutions. Illustra NAP-5 columns were purchased from GE Healthcare Life Sciences. Anhydrous ethanol and 2-propanol were purchased from Commercial Alcohol, and water used for all experiments was deionized to 18 MΩ using a Millipore system. All chemicals were purchased from Sigma Aldrich. Oligonucleotides were purchased from Integrated DNA Technologies. Thiolated DNA sequences were purified by HPLC, and nonthiolated DNA sequences were purified by standard desalting.

DNA sequence for ATP detection

Seq 1: 5'- T GAC ACC TTA_{10}-$(CH_2)_3$- SH- 3'

Seq 2: 5'- ACC TGG GGG AGT ATT GCG GAG GAA GGT GTC ACA A_{10}-$(CH_2)_3$- SH- 3'

DNA sequence for DNA-210 detection

DNA-210 (target): 5′- CTG TGC GTG TGA CAG CGG CTG A -3′

Seq 3 (Probe): 5′-SH-$(CH_2)_6$-AAA AAT CAG CCG CTG TCA CAC GCA CAG -3′

Seq 4: 5′ -SH-$(CH_2)_6$-A_{10} GCA GTG ACA -3′

Seq 5: 5′- TGT CAC TGC -3′ (cap sequence)

Functionalization of nanoparticles with DNA

The procedure was adapted from Chapter 4 and briefly described below.

The cleaved oligonucleotides of Seq 3 and Seq 4 (with ~ 0.1 OD at 260 nm) were mixed with 0.6 nM bis(p-sulfonatophenyl) phenylphosphine-capped AuNPs (~1 mg/mL of BSPP:AuNP) on a thermo-shaker (40°C, 650 rpm) for 30 min. The pH-assisted method was used to promote DNA

adsorption.[26] Subsequently, NaCl concentration was raised to 0.4 M NaCl at 50°C. The mixture was incubated for 12 h before washing with centrifugation and redispersion in a buffer containing 0.01 M phosphate buffer (PB), 0.05 M NaCl, 0.01% SDS, and 0.01% azide at 4°C.

Seq 1- and Seq 2-functionalized 45-nm decahedral Au shell NPs were prepared similarly, except for the final 0.3M NaCl in the salt aging process.

Aggregation in solution

To troubleshoot the cross-hybridization of Seq 2-AuNP with Seq 4-AuNP, aggregates were formed in solution by mixing the DNA-AuNPs at a one-to-one ratio (at total AuNP concentration of 0.15 nM in 0.01 M PB) in a microcuvette. The concentration of NaCl of the mixture was raised to 0.3 M. A UV−vis spectrophotometer measured the absorbance spectra at 10 min intervals for 2-3 h.

To test the functionality of the capping sequence, a colloidal solution of Seq 4-AuNP (0.15 nM) was incubated with Seq 5 (100 μM) in a buffer solution of 0.01 M PB, 0.3 M NaCl for 1-2 h. The particles were centrifuged to remove the excess Seq 5, and followed by mixing with Seq 2-AuNP in a buffer solution of 0.01 M PB, 0.3 M NaCl. A UV−vis spectrophotometer measured the absorbance spectra at 10 min intervals in 2-3 h.

Fabrication of core-satellite assemblies as chip-based sensors

The procedure was adapted from Chapter 4 and briefly described below.

Deposition and DNA-functionalization of core AuNPs on an amino-modified substrate

A volume of 40 μL of 60 nm citrate-capped AuNPs (15 pM) was first immobilized on an APTMS-treated coverslip for 2 minutes. The anchored core particles were then functionalized with Seq 4 using 10 μL of a solution containing 0.01 M PB, 0.7 M NaCl, 0.1% SDS, and DNA (2-5 μM) for 2 hours. The coverslip was rinsed with water and dried with compressed air. For deposition

of the second chip-based sensor, a volume of 40 μL of 60 nm AuNPs (30 pM) was immobilized on the APTMS-treated substrate. The substrate was then incubated with Seq 1 using 10 μL of a solution containing 0.01 M PB, 0.4 M NaCl, 0.1% SDS, and DNA (2-5 μM) for 2 hours. The coverslip was rinsed with water and dried with compressed air.

To prevent non-specific binding of the satellite nanoparticles on the amino-modified glass coverslip, the remaining amino groups were passivated using 10 mM mPEG-Succinimidyl Valerate (LaysanBio) in 0.1 M bicarbonate buffer (pH of 8.3) for 4 hours. Then the coverslip was treated with a 0.2 M solution of sulfo-NHS-acetate in 0.1 M bicarbonate buffer (pH 8.3) for 4 hours. The sample was rinsed with water and dried with compressed air.

Layer-by-layer assembly of satellite nanoparticles to fabricate chip-based duplexed sensors

The fabrication of chip-based sensors is adapted via a layer-by-layer assembly process. AuNPs assemblies targeting DNA-210 were firstly constructed, followed by the assembly of AuNPs assemblies targeting ATP. To assemble the first layer of 30-nm Au satellite nanoparticles, a volume of ~40 μL of Seq 3-AuNP in 0.01 M PB, 0.4 M NaCl, and 0.01% SDS was incubated with core AuNP on 0.6 nM the coverslip for 60 min. The solution was replaced with buffer (0.01 M PB, 0.4 M NaCl), subsequently the solution of Seq 4-AuNP was introduced at the same condition, and then the sample was washed with buffer. To cap Seq 4, the sample was incubated with Seq 5 in 0.01 M PB, 0.3 M NaCl for 1-2 hours, and washed with buffer (0.01 M PB, 0.3 M NaCl). To construct NP assemblies targeting ATP, a volume of 40 μL of 0.6 nM Seq 4-AuNP in 0.01 M PB, 0.3 M NaCl, and 0.01% SDS was incubated for 60 min to assemble the first layer of Au shell satellite NPs. The solution was washed with buffer (0.01 M PB, 0.32 M NaCl). The procedure was repeated with DNA-AuNP of alternating sequences to build up 3 layers in the core-satellite structure. The fabrication procedure is the same for Au solid-shell assemblies, except for

the buffer containing 0.32 M NaCl. The assembly of each layer was monitored by darkfield microscopy. The coverslip samples were stored in 0.01 M PB and 0.12 M NaCl until sensing experiments.

Darkfield microscope and Data analysis please refer to Chapter 4.

5.6 References

(1) Yao, J.; Yang, M.; Duan, Y. Chemistry, Biology, and Medicine of Fluorescent Nanomaterials and Related Systems: New Insights into Biosensing, Bioimaging, Genomics, Diagnostics, and Therapy. *Chem. Rev.* **2014**, *114*, 6130–6178.

(2) Fothergill, S. M.; Joyce, C.; Xie, F. Metal Enhanced Fluorescence Biosensing: From Ultra-Violet towards Second near-Infrared Window. *Nanoscale* **2018**, *10*, 20914–20929.

(3) Tobos, C. I.; Sheehan, A. J.; Duffy, D. C.; Rissin, D. M. Customizable Multiplex Antibody Array Immunoassays with Attomolar Sensitivities. *Anal. Chem.* **2020**, *92*, 5613–5619.

(4) Schena, M., Shalon, D., Davis, R. and Brown, P. Quantitative Monitoring of Gene Expression Patterns with a Complementary DNA Microarray. *Science* **1995**, *270*, 467–470.

(5) Templin, M. F.; Stoll, D.; Schrenk, M.; Traub, P. C.; Vöhringer, C. F.; Joos, T. O. Protein Microarray Technology. *Drug Discov. Today* **2002**, *7*, 815–822.

(6) Yin, J. Q.; Zhao, R. C.; Morris, K. V. Profiling MicroRNA Expression with Microarrays. *Trends Biotechnol.* **2008**, *26*, 70–76.

(7) Gold, L.; Walker, J. J.; Wilcox, S. K.; Williams, S. Advances in Human Proteomics at High Scale with the SOMAscan Proteomics Platform. *N. Biotechnol.* **2012**, *29*, 543–549.

(8) Gold, L.; Ayers, D.; Bertino, J.; Bock, C.; Bock, A.; Brody, E. N.; Carter, J.; Dalby, A. B.; Eaton, B. E.; Fitzwater, T.; *et al.* Aptamer-Based Multiplexed Proteomic Technology for Biomarker Discovery. *PLoS One* **2010**, *5*.

(9) Vignali, D. A. A. Multiplexed Particle-Based Flow Cytometric Assays. *J. Immunol. Methods* **2000**, *243*, 243–255.

(10) Burnham, C. A. D.; Doern, C.; Binder, S. R. *Microsphere-Based Multiplex Immunoassays: Development and Applications Using Luminex® XMAP® Technology*; Fourth Edi.; Elsevier Ltd, 2013.

(11) Parak, W. J.; Gerion, D.; Pellegrino, T.; Zanchet, D.; Micheel, C.; Williams, S. C.; Boudreau, R.; Le Gros, M. A.; Larabell, C. A.; Alivisatos, A. P. Biological Applications of Colloidal Nanocrystals. *Nanotechnology* **2003**, *14*, 15–27.

(12) Qiu, X.; Hildebrandt, N. Rapid and Multiplexed MicroRNA Diagnostic Assay Using

Quantum Dot-Based Forster Resonance Energy Transfer. *ACS Nano* **2015**, *9*, 8449–8457.

(13) Han, M.; Gao, X.; Su, J. Z.; Nie, S. Quantum-Dot-Tagged Microbeads for Multiplexed Optical Coding of Biomolecules. *Nat. Biotechnol.* **2001**, *19*, 631–635.

(14) Ming, K.; Kim, J.; Biondi, M. J.; Syed, A.; Chen, K.; Lam, A.; Ostrowski, M.; Rebbapragada, A.; Feld, J. J.; Chan, W. C. W. Integrated Quantum Dot Barcode Smartphone Optical Device for Wireless Multiplexed Diagnosis of Infected Patients. *ACS Nano* **2015**, *9*, 3060–3074.

(15) El-Sayed, I. H.; Huang, X.; El-Sayed, M. A. Surface Plasmon Resonance Scattering and Absorption of Anti-EGFR Antibody Conjugated Gold Nanoparticles in Cancer Diagnostics: Applications in Oral Cancer. *Nano Lett.* **2005**, *5*, 829–834.

(16) Mayer, K. M.; Hafner, J. H.; Antigen, A. À. Localized Surface Plasmon Resonance Sensors. *Chem. Rev.* **2011**, *111*, 3828–3857.

(17) Hay Burgess, D. C.; Wasserman, J.; Dahl, C. A. Global Health Diagnostics. *Nature* **2006**, *444 Suppl*, 1–2.

(18) Nikoobakht, B.; El-Sayed, M. A. Preparation and Growth Mechanism of Gold Nanorods (NRs) Using Seed-Mediated Growth Method. *Chem. Mater.* **2003**, *15*, 1957–1962.

(19) Jana, N. R.; Gearheart, L.; Murphy, C. J. Wet Chemical Synthesis of High Aspect Ratio Cylindrical Gold Nanorods. *J. Phys. Chem. B* **2001**, *105*, 4065–4067.

(20) Eustis, S.; El-Sayed, M. A.; Kasha, M. Why Gold Nanoparticles Are More Precious than Pretty Gold : Noble Metal Surface Plasmon Resonance and Its Enhancement of the Radiative and Nonradiative Properties of Nanocrystals of Different Shapes. *Chem. Soc. Rev.* **2006**, *35*, 209–217.

(21) Yu, C.; Nakshatri, H.; Irudayaraj, J. Identity Profiling of Cell Surface Markers by Multiplex Gold Nanorod Probes. *Nano Lett.* **2007**, *7*, 2300–2306.

(22) Yu, C.; Irudayaraj, J. Multiplex Biosensor Using Gold Nanorods. *Anal. Chem.* **2007**, *79*, 572–579.

(23) Chen, P.; Chung, M. T.; McHugh, W.; Nidetz, R.; Li, Y.; Fu, J.; Cornell, T. T.; Shanley, T. P.; Kurabayashi, K. Multiplex Serum Cytokine Immunoassay Using Nanoplasmonic Biosensor Microarrays. *ACS Nano* **2015**, *9*, 4173–4181.

(24) Le, N. H.; Nguyen, B. K.; Ye, G.; Peng, C.; Chen, J. I. L. Tuning the Sensing Performance of Multilayer Plasmonic Core-Satellite Assemblies for Rapid Detection of Targets from Lysed Cells. *ACS Sensors* **2017**, *2*, 1578–1583.

(25) Ghotra, G.; Nguyen, B. K.; Chen, J. I. L. DNA-Functionalized Gold Nanoparticles with Toehold-Mediated Strand Displacement for Nucleic Acid Sensors. *ACS Appl. Nano Mater.* **2020**, *3*, 10123–10132.

(26) Zhang, X.; Servos, M. R.; Liu, J. Instantaneous and Quantitative Functionalization of Gold Nanoparticles with Thiolated DNA Using a PH-Assisted and Surfactant-Free Route. *J. Am. Chem. Soc.* **2012**, *134*, 10–13.

(27) Zhou, J.; Lei, G.; Zheng, L. L.; Gao, P. F.; Huang, C. Z. HSI Colour-Coded Analysis of Scattered Light of Single Plasmonic Nanoparticles. *Nanoscale* **2016**, *8*, 11467–11471.

(28) Nutiu, R.; Li, Y. Structure-Switching Signaling Aptamers. *J. Am. Chem. Soc.* **2003**, *125*, 4771–4778.

(29) Nutiu, R.; Li, Y. In Vitro Selection of Structure-Switching Signaling Aptamers. *J. Am. Chem. Soc.* **2005**, *125*, 4771–4778.

(30) Lau, P. S.; Li, Y. Exploration of Structure-Switching in the Design of Aptamer Biosensors. *Adv. Biochem. Eng. Biotechnol.* **2014**, *140*, 69–92.

(31) Bavelloni, A.; Ramazzotti, G.; Poli, A.; Piazzi, M.; Focaccia, E.; Blalock, W.; Faenza, I. Mirna-210: A Current Overview. *Anticancer Res.* **2017**, *37*, 6511–6521.

(32) Zhang, D. Y.; Winfree, E. Control of DNA Strand Displacement Kinetics Using Toehold Exchange. *J. Am. Chem. Soc.* **2009**, *131*, 17303–17314.

(33) Tang, W.; Zhong, W.; Tan, Y.; Wang, G. A.; Li, F.; Liu, Y. DNA Strand Displacement Reaction: A Powerful Tool for Discriminating Single Nucleotide Variants. *Top. Curr. Chem.* **2020**, *378*, 1–30.

Chapter 6 – Conclusion, Limitations, and Future Directions

6.1 General Conclusion

This dissertation presented a quantitative sensing platform using discrete NP assemblies. With DNA-aptamer as linkers, sensing of model targets was achieved by disassembling the nanostructure, and the associated decrease in scattering intensity was readily captured by darkfield microscopy. Enhanced light scattering of the NP assemblies enables high-throughput image-based analysis of hundreds of structures in a single field of view using darkfield imaging. Additionally, the sensing performance, such as detection limit, dynamic range, and sensitivity can be tuned by controlling the size of assemblies. When NP assemblies are anchored on a flexible support, the analytes such as ATP from lysed cells can be directly detected by nearby plasmonic NP assemblies without separation or purification. The NP assemblies were also used to quantitate the concentration of ATP in cancer cells and map out molecular distributions on 2D heterogeneous surfaces. The sensing patches with embedded NP assemblies show the potential for on-site diagnostics or measurements. Furthermore, the optical properties of NP assemblies can be tuned to longer wavelengths using gold nanoshells. By fabricating different morphologies of NP assemblies with different DNA linkers in a common area, the duplex sensors among the mixture of NP assemblies can be easily identified based on colors, facilitating the multiplexed detection. We envision that the development of plasmonic sensing chips based on highly scattering single nanostructures may enable simple and low-cost analysis when they are incorporated with the portable imaging system. Plasmon coupling of core-satellite NP assemblies may also be of interest in other fields that seek to amplify the electromagnetic fields, such as surface-enhanced Raman scattering and solar energy conversion.

6.2 Limitations

Despite the successful analysis at the single-nanostructure level, some challenges need to be addressed. One is the uniformity of the morphology of plasmonic nanoparticles. It is well known that the size and shape strongly affect the LSPR of plasmonic nanoparticles. The size and morphology variations led to broad LSPR and contributed to different optical signals between nanostructures. The other limitation involves instrumentation, where the spectral sensitivity of a common charge-coupled device is in the visible range. Therefore, imaging discrete nanostructures are most effective when the LSPR matches the detector's optical response curve. Thus, experimental designs for tuning the LSPR are limited due to materials properties and the detector's spectral response. Moreover, the sensing platform via the disassembly of NP assemblies requires the reconfiguration of DNA linkers upon the binding target. The linkers should be able to deconstruct NP assemblies to generate the detection signal, thus limiting the detection for various analytes. Accordingly, establishing sensors to improve diversity often requires many efforts, such as designing and optimizing linkers and fabrication.

6.3 Future Directions

The results presented in this dissertation have proved that the sensing platforms based on NP assemblies have great potential for detecting metabolites and biomarkers in the cellular environment. Further work may be carried out in the following areas.

First, multiplexed assays can be further developed and applied to in vitro systems, such as mapping out the cellular microenvironment. For example, a hypoxic microenvironment in which oxygen concentration is reduced remarkably can affect the cellular metabolism of both ATP production and miRNA-210 expression. It has been reported that hypoxic cells up-regulate miR-210 expression[1] and diminish ATP production by lowering the activity of the electron transport

chain through activation of the transcription factor hypoxia-inducible factor-1.[2,3] The duplexed sensors using NP assemblies can measure the concentration of ATP and miRNA-210; hence we can validate their correlation at the single-cell level, which is difficult to achieve with conventional techniques (e.g. flow cytometry).

Second, the chip-based sensing using single NP can be further expanded to detect different targets by incorporating linkers for targeting other molecules (i.e. vascular endothelial growth factor, VEGF). VEGF is a regulator of angiogenesis, a process in which new blood vessels form from pre-existing ones by activating the VEGF-receptor tyrosine kinases in endothelial cells.[4] The overexpression or downregulation of VEGF is associated with cancers. It plays a crucial role in tumor growth and metastasis.[5] VEGF has been used as a biomarker for various types of human diseases and cancers. Different analytical techniques to quantitatively analyze VEGF were reported, including ELISA assays,[6] fluorescent spectrometry,[7] and electrochemical immunosensors.[8] Several researchers have reported different nucleic acid aptamers that can bind to high abundant $VEGF_{165}$ with dissociation constant (K_d) in nano- and picomolar range,[9,10] and the aptasensors for VEGF protein with high sensitivity have been developed. Recently, an optical aptasensor based on fluorescence resonance energy transfer (FRET) using semiconductor quantum dots (QDs) for detection of $VEGF_{165}$ was reported as shown in Figure 6.1.[11] The hybridization of aptamer-functionalized QDs with the partially complementary nucleic acid-functionalized black-hole quencher (BHQ2) results in FRET quenching of the QDs. The presence of VEGF stimulated the dehybidization of the duplex through the formation of the aptamer/VEGF complex, leading to the quencher-free QDs and turn-on the luminescence of the QDs (Fig. 6.1b). This sensing platform enabled the analysis of VEGF with a detection limit of ca 1 pM. We can adapt the DNA linker design for the detection of the VEGF protein with the platform using NP assemblies. At first, the

DNA linker sequences and surface DNA density will be optimized to ensure the high stability of aptamer-functionalized NPs and disassembly upon binding of the VEGF target. Next, we can fabricate the core-satellite nanostructure on a substrate for the detection of VEGF based on DF images. Then we can explore the sensing patch assay or "stick-and-peel" for detection of circulated serum $VEGF_{165}$ directly from the blood that can have the potential for a clinical cancer diagnostic. Moreover, several studies have found a correlation between miR-210 and VEGF expression in the hypoxic microenvironment. In particular, a hypoxic microenvironment can induce angiogenesis by up-regulating numerous VEGF proteins including $VEGF_{165}$, and overexpressing miRNA-210 in human umbilical vein endothelial cells.[12] A long-term work may aim to develop a multiplexed assay using single nanostructure of NP assemblies linked by different aptamers for detection of $VEGF_{165}$ protein and miRNA-210 in hypoxic cells. Furthermore, we can also focus on detection of VEGF protein in tumor microenvironments using NP assemblies. Studies have found that the fast growth of tumor cells results in overexpression of VEGF which triggers the formation of tumor blood vessels for the supply of nutrients and oxygen to the cancer cells;[5] hence, local detection of VEGF in the population of heterogeneous tumor cells can aid researchers to understand differentiation, proliferation and metastasis process of cancer cells and also can be used as a predictive factor for malignancy.[8] To achieve local detection, we can explore the sensing patch assay to map VEGF of the tissue fixation. VEGF can be either secreted or expunged from tissue samples hence can bind to aptamer linkers and trigger optical signals of NP assemblies. This methodology can be validated by immunohistochemistry staining. Subsequently, we can apply this methodology to study the heterogeneity of VEGF on the tumor sample.

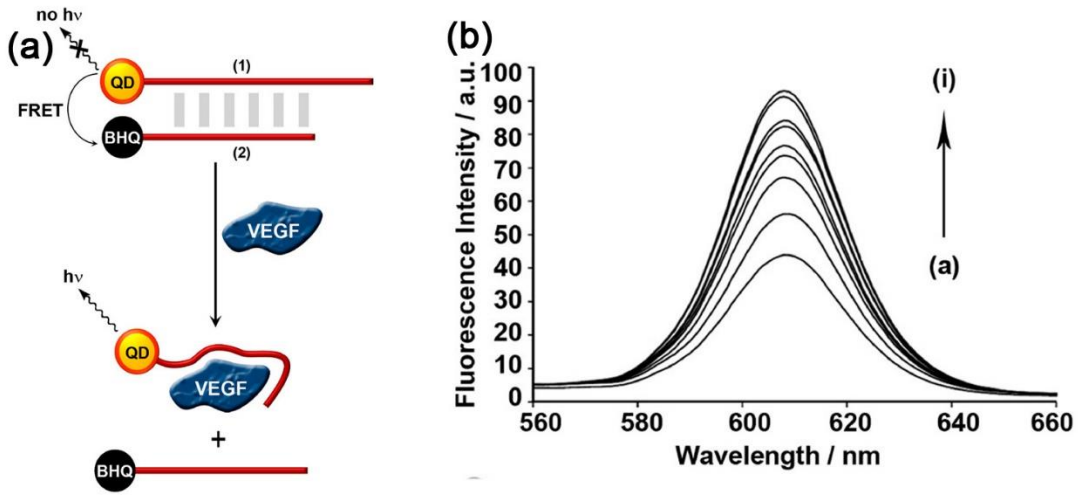

Figure 6.1. (a) Schematic optical aptasensor of $VEGF_{165}$ protein by CdSe/ZnS QDs modified with VEGF aptamer**.** (b) Time-dependent luminescence changes of the QDs at $\lambda = 620$ nm upon treatment with VEGF. Spectra were recorded at time intervals of 5 min. Reprint with permission from ref 11. Copyright 2012 American Chemical Society.

Finally, the works in the thesis were performed with a research-grade inverted microscope, and hence are not applicable in resource-limited settings. On the other hand, the strong light scattering properties of plasmonic nanostructures allows for their imaging with consumer-grade systems such as smartphone cameras. Thus, future work on building a portable, cost-effective and easy-to-operate imaging device can advance the field of analytical biosensors based on single nanostructures for point-of-care (POC) applications and on-site diagnostics. It is foreseeable that a smartphone can be used for microscopy imaging, wherein the scattered colors of NP via oblique-angle illumination are captured by the built-in camera, and their images are readily analyzed using a smartphone app. A recent report demonstrated the mobile phone-based darkfield microscope device, consisting of the cellphone camera equipped with in-house designed accessories including LEDs light source, condenser, and objective lens as shown in Figure 6.2 that were used to quantify nanoparticle signal and demonstrated to be comparable to benchtop DFM at low magnification

(~10X–20X).[13] However, this portable DFM device was found the limit of low optical signal quality due to weak and uneven sample illumination from a multi-LED light source and optical focusing. We may adapt this design but with the improvements of optical quality including the single LED light source with stronger illumination intensity and a custom-design box with the adjustable distance of sample to optical lens and condenser to refine the focusing. Nevertheless, future challenges in the development of portable LSPR-based devices can lie in both hardware and software, which may include optimizing sensing chips with high sensitivity, integrating components and devices (e.g. optical lens, sample holder, light source, and condenser), and programming a smartphone app for color analysis.[14,15]

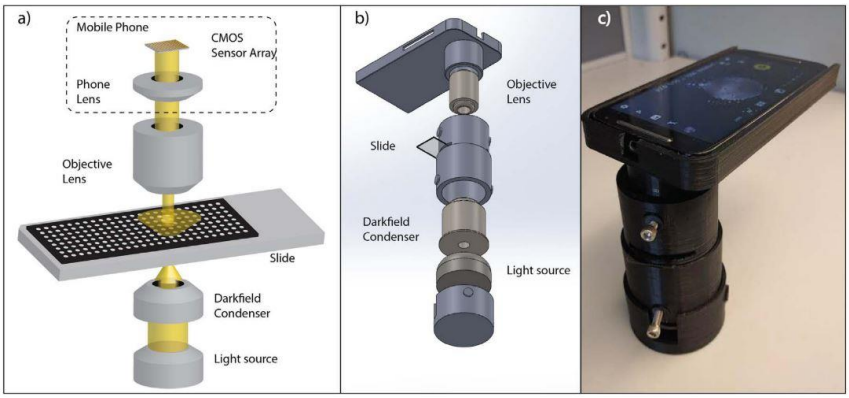

Figure 6.2. Mobile darkfield microscope system (a) layout schematic, (b) assembly and (c) working prototype. Reprint with permission from ref 13. Copyright 2017 Elsevier.

6.4. References

(1) Bavelloni, A.; Ramazzotti, G.; Poli, A.; Piazzi, M.; Focaccia, E.; Blalock, W.; Faenza, I. Mirna-210: A Current Overview. *Anticancer Res.* **2017**, *37*, 6511–6521.

(2) Wheaton, W. W.; Chandel, N. S. Hypoxia. 2. Hypoxia Regulates Cellular Metabolism. *Am. J. Physiol. - Cell Physiol.* **2011**, *300*, c385-393.

(3) Costales, M. G.; Haga, C. L.; Velagapudi, S. P.; Childs-Disney, J. L.; Phinney, D. G.; Disney, M. D. Small Molecule Inhibition of MicroRNA-210 Reprograms an Oncogenic Hypoxic Circuit. *J. Am. Chem. Soc.* **2017**, *139*, 3446–3455.

(4) Neufeld, G.; Cohen, T.; Gengrinovitch, S.; Poltorak, Z. Vascular Endothelial Growth

Factor (VEGF) and Its Receptors. *FASEB* **1999**, *13*, 9–22.

(5) Apte, R. S.; Chen, D. S.; Ferrara, N. VEGF in Signaling and Disease: Beyond Discovery and Development. *Cell* **2019**, *176*, 1248–1264.

(6) Scapini, P.; Calzetti, F.; Cassatella, M. A. On the Detection of Neutrophil-Derived Vascular Endothelial Growth Factor (VEGF). *J. Immunol. Methods* **1999**, *232*, 121–129.

(7) Lan, J.; Li, L.; Liu, Y.; Yan, L.; Li, C.; Chen, J.; Chen, X. Upconversion Luminescence Assay for the Detection of the Vascular Endothelial Growth Factor, a Biomarker for Breast Cancer. *Microchim. Acta* **2016**, *183*, 3201–3208.

(8) Prabhulkar, S.; Alwarappan, S.; Liu, G.; Li, C. Z. Amperometric Micro-Immunosensor for the Detection of Tumor Biomarker. *Biosens. Bioelectron.* **2009**, *24*, 3524–3530.

(9) Potty, A. S. R.; Kourentzi, K.; Fang, H.; Jackson, G. W.; Zhang, X.; Legge, G. B.; Willson, R. C. Biophysical Characterization of DNA Aptamer Interactions with Vascular Endothelial Growth Factor. *Biopolymers* **2009**, *91*, 145–156.

(10) Nonaka, Y.; Sode, K.; Ikebukuro, K. Screening and Improvement of an Anti-VEGF DNA Aptamer. *Molecules* **2010**, *15*, 215–225.

(11) Freeman, R.; Girsh, J.; Fang-ju Jou, A.; Annie Ho, J.; Hug, T.; Dernedde, J.; Willner, I. Optical Aptasensors for the Analysis of the Vascular Endothelial Growth Factor (VEGF). *Anal. Chem.* **2012**, *84*, 6192–6198.

(12) Huang, X.; Zuo, J. Emerging Roles of MiR-210 and Other Non-Coding RNAs in the Hypoxic Response. *Acta Biochim. Biophys. Sin. (Shanghai).* **2014**, *46*, 220–232.

(13) Sun, D.; Hu, T. Y. A Low Cost Mobile Phone Dark-Field Microscope for Nanoparticle-Based Quantitative Studies. *Biosens. Bioelectron.* **2018**, *99*, 513–518.

(14) Huang, X.; Xu, D.; Chen, J.; Liu, J.; Li, Y.; Song, J.; Ma, X.; Guo, J. Smartphone-Based Analytical Biosensors. *Analyst* **2018**, *143*, 5339–5351.

(15) Roda, A.; Calabretta, M. M.; Calabria, D.; Caliceti, C.; Cevenini, L.; Lopreside, A.; Zangheri, M. *Smartphone-Based Biosensors for Bioanalytics: A Critical Review*; Elsevier Ltd, 2017; Vol. 77.

Appendix

(This appendix includes further background information on Finite-Difference Time-Domain, darkfield microscopy, and image-based analysis)

A1. Finite-Difference Time-Domain

Although a variety of nanoparticle shapes have been synthesized, their plasmonic properties cannot be solved by Mie theory as is the case for spheres or rods. The Finite-Difference Time-Domain (FDTD) is a numerical method to solve Maxwell's equations for electromagnetic simulations of almost any arbitrarily complex geometries. A typical FDTD setup for the simulation of nanoparticles is illustrated in Figure A1. The incoming wave hits targets containing one or several nanoparticles. The electromagnetic field excites the plasmons in the individual nanoparticles. The plasmon on individual nanoparticles interacts, leading to an induced new total field that can be used to generate optical cross-sections.[1]

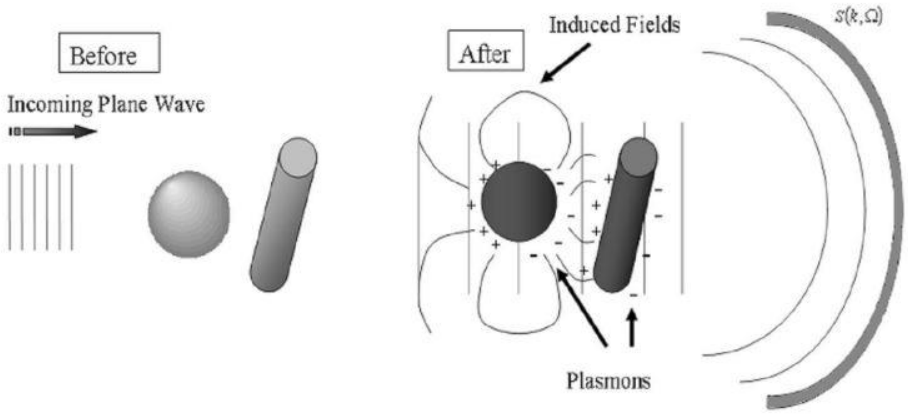

Figure A1. A typical finite-difference time-domain experiment. Nanoparticles are illuminated with a wave plane. A surface plasmon is excited on individual nanoparticles and creates an electromagnetic field, which can be used to generate cross-section. Reprinted with permission from ref 1.

As defined, FDTD simply discretizes Maxwell's equation both in time and domain with central difference approximations. In other words, the equations of electric and magnetic fields are solved numerically on a discrete grid in both space and time. To do so, the numerically finite algorithm developed by Yee is applied to solve Maxwell's equations by using grids for computing the electric field $\vec{E}$ and magnetic field $\vec{H}$ in a leapfrog time manner. Figure A2 shows that a 3D Yee cell contains each electric field component (E_x, E_y, E_z) surrounded by four magnetic field components (H_x, H_y, H_z), and each magnetic field component (H_x, H_y, H_z) surrounded by four electric field components (E_x, E_y, E_z). For example, in yz plan, H_x is surrounded by four electric field components (E_y and E_z) as illustrated in the red circle in Figure A2. The derivative of H_x can be calculated by E_y and E_Z at two different domains according to Faraday's law, which stated that the partial derivative of an arbitrary H-component with respect to time, which equals the curl of the electric field on that exact point. Therefore, the derivative of H_x can be calculated approximately by the central difference of the surrounding E-components. Likewise, the partial derivative of an arbitrary E-component with respect to time can be approximately expressed by the surrounding H-components. The discretized electric and magnetic field components in a time domain can be defined and the magnetic field and electric field can be approximated using a leapfrog scheme. For instance, the derivative H and E can be defined following the sequence: $H_0 \rightarrow E_{1/2} \rightarrow H_1 \rightarrow E_{3/2} \rightarrow H_2$, etc. Consequently, the partial derivative of an arbitrary E (or H) component with respect to time is approximately expressed by the central difference of the neighboring discretized components in time. The finite difference can then be used to simulate the frequency spectra of nanoparticles using Fourier transforms.

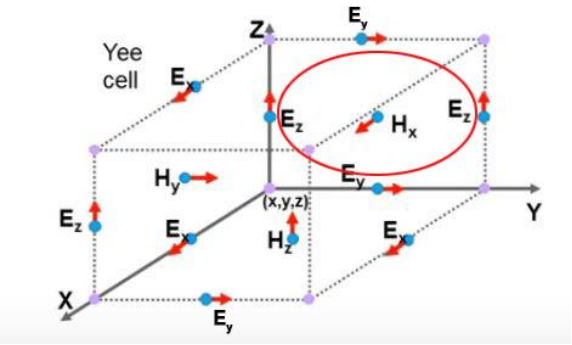

Figure A2. Arrangement of electric and magnetic field components on a Yee cell (x,y,z). In a Yee cell, each magnetic field vector in a half grid of cell is circulated in a closed-loop by the electric field and each electric field vector is circulated by magnetic field in this cell and adjacent cell. Adapted with permission from ref 2.

A1.1 Numerical Algorithm

In general, Maxwell's equations are given in differential form with a medium of permittivity ε and permeability μ

$$\mu \frac{\partial \vec{H}}{\partial t} = -\nabla \times \vec{E}$$

$$\varepsilon \frac{\partial \vec{E}}{\partial t} = \nabla \times \vec{H} - J$$

in which E represents the electric field, H represents the magnetic field and $J = J_c + J_i$ is a sum of the electrical current where $J_c = conductivity\ (\sigma) \times E$ and J_i is the source current density. Two vector equations where each vector equation can be decomposed into three scalar equations for three-dimensional space as represented with the following six scalar equations for the Cartesian coordinate system (x,y,z)

$$\frac{\partial E_x}{\partial t} = \frac{1}{\varepsilon_x}\left(\frac{\partial H_z}{\partial y} - \frac{\partial H_y}{\partial z} - \sigma_x E_x - J_{ix}\right) \quad \text{(A1)}$$

$$\frac{\partial E_y}{\partial t} = \frac{1}{\varepsilon_y}\left(\frac{\partial H_x}{\partial z} - \frac{\partial H_z}{\partial y} - \sigma_y E_y - J_{iy}\right) \quad \text{(A2)}$$

$$\frac{\partial E_z}{\partial t} = \frac{1}{\varepsilon_z}\left(\frac{\partial H_y}{\partial x} - \frac{\partial H_x}{\partial y} - \sigma_z E_z - J_{iz}\right) \quad \text{(A3)}$$

$$\frac{\partial H_x}{\partial t} = \frac{1}{\mu_x}\left(\frac{\partial E_y}{\partial z} - \frac{\partial E_z}{\partial y}\right) \quad \text{(A4)}$$

$$\frac{\partial H_y}{\partial t} = \frac{1}{\mu_y}\left(\frac{\partial E_z}{\partial x} - \frac{\partial E_x}{\partial z}\right) \quad \text{(A5)}$$

$$\frac{\partial H_z}{\partial t} = \frac{1}{\mu_z}\left(\frac{\partial E_x}{\partial y} - \frac{\partial E_y}{\partial x}\right) \quad \text{(A6)}$$

By applying the FDTD method, the discrete spatial positions of the field components have a specific arrangement in the Yee cell. Figure A3 shows the electric field E_x vector is surrounded by four magnetic field vectors that are curling around the electric field vector, thus simulating Ampere's law.

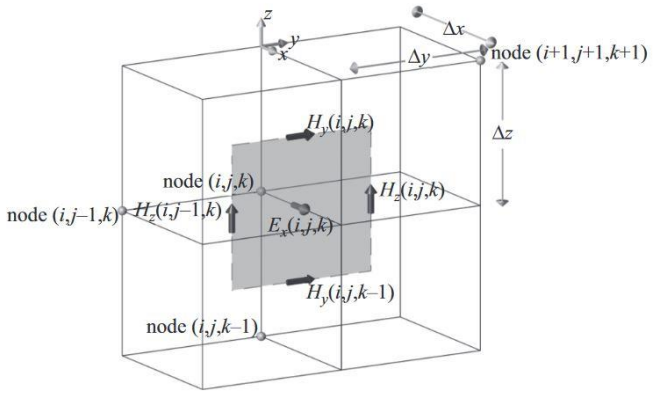

Figure A3. Field components around E_x in indexed cell (i,j,k)

By approximation of second-order differentiation

$$f'(x) \approx \frac{f(x + \Delta x/2) - f(x - \Delta x/2)}{\Delta x}$$

The electric field E_x^{n+1} can be calculated from equation A1

$$\frac{E_x^{n+1}(i,j,k) - E_x^n(i,j,k)}{\Delta t} = \frac{1}{\varepsilon_x(i,j,k)}\frac{H_z^{n+(1/2)}(i,j,k) - H_z^{n+(1/2)}((i,j-1,k)}{\Delta y} - \frac{1}{\varepsilon_x(i,j,k)}\frac{H_z^{n+(1/2)}(i,j,k) - H_z^{n+(1/2)}((i,j,k-1)}{\Delta z} - \frac{\sigma_x^e(i,j,k)}{\varepsilon_x(i,j,k)}E_x^{n+(1/2)}(i,j,k) - \frac{1}{\varepsilon_x(i,j,k)}J_{ix}^{n+(1/2)}(i,j,k) \quad \text{(A7)}$$

The equation demonstrates the approximation of the future value of an electric field component by using the past values of the electric field component, the magnetic field components, and the source components. This form of an equation is called an FDTD updating equation. Similarly, updating equations of $E_y^{n+1}$and E_z^{n+1} can also be obtained from equations A2 and A3, respectively.

The updating equations can be obtained for magnetic field components following the same methodology. Figure A4 shows each magnetic field H_x vector surrounded by four electric field vectors that are curling around the magnetic field vector, thus simulating Faraday's law. It should be noted that the H component is half of the grid in the Yee cell, thus domain is calculated by n+1/2

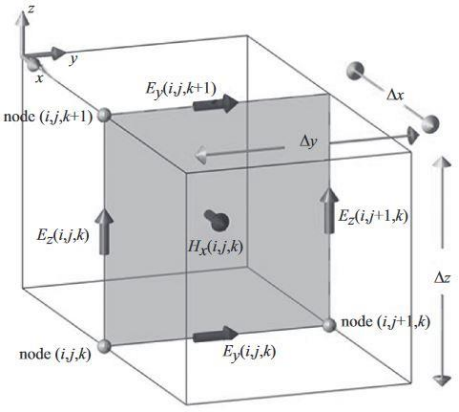

Figure A4. Field components around H_x in indexed cell (i,j,k)

The magnetic field $H_x^{n+1/2}$ in indexed cell (i,j,k) is approximated from equation A4

$$H_x^{n+(1/2)}(i,j,k) = H_x^{n-(1/2)}(i,j,k) + \frac{\Delta t}{\mu_x(i,j,k)}\left(\frac{E_y^n(i,j,k+1) - E_y^n((i,j,k)}{\Delta z} - \frac{E_z^n(i,j+1,k) - E_z^n(i,j,k)}{\Delta y}\right) \quad \text{(A8)}$$

Similarly, update equation for magnetic field $H_y^{n+(1/2)}$ is derived from equation A5 and $H_z^{n+(1/2)}$ is derived from equation A6. Therefore, six updated equations containing magnetic and electric fields in different times and domains are defined.

A1.2 Simulation Procedures

Once the FDTD updating equations are derived, FDTD simulation can be constructed as illustrated in Figure A5. The first step in this algorithm is to construct a working space containing a rectangular mesh that represents Yee cells as shown in Figure A6. Space includes the objects, material types, and sources that can be used to define parameters for the simulation. It should be noted that mesh can control simulation quantities because electromagnetic field or other material properties are calculated at each mesh point. Using a smaller mesh allows for a more accurate simulation but there exists a substantial cost. As the mesh is smaller, the simulation time and memory will increase. Before starting the simulation, the coefficient terms from updated equations are first calculated and stored. The field components are solved with initial values starting at zeros and then induced in the space due to sources as the iteration proceeds. The FDTD iterations continue indefinitely until some stop command is applied or automatic termination of the simulation when most of the energy has left the simulation volume.

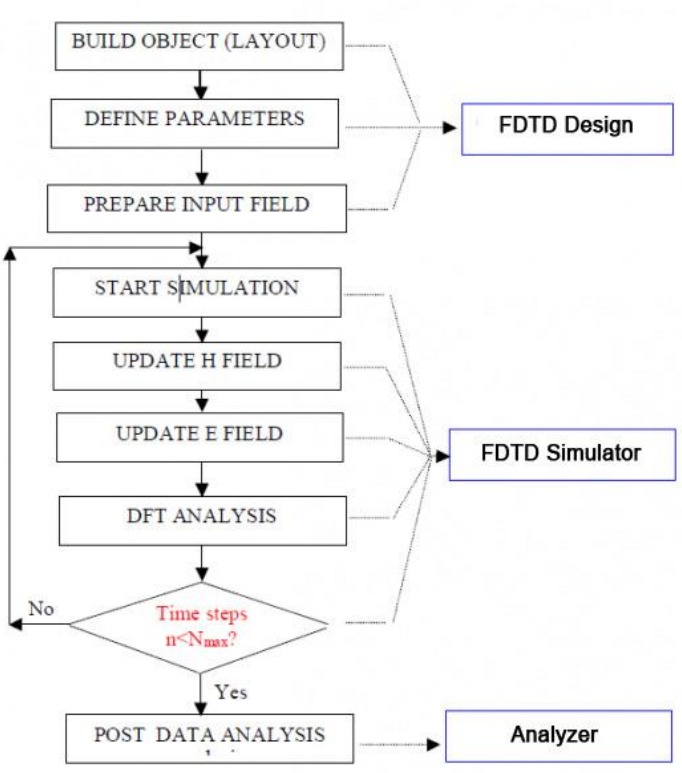

Figure A5. Finite-difference time-domain simulation procedure

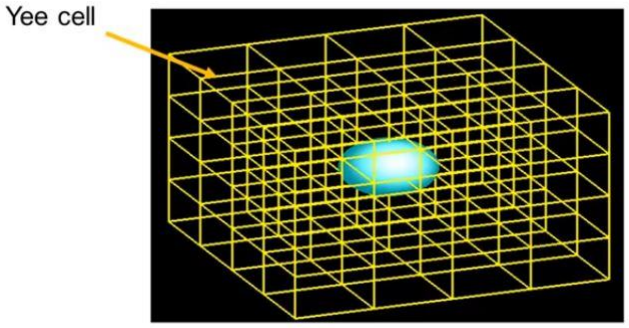

Figure A6. The Finite-difference time-domain simulation is constructed based on multiple Yee cells. Reproduced with permission from ref 3

This method can be applied in both two and three dimensions, FDTD methods have been extensively applied to studies of nanomaterial optical properties. As an application of FDTD on the 3D nanostructure, we simulated scattering spectra of core-satellite assemblies with incremental numbers of particles randomly placed around the core (see Chapters 3 and 4). The simulated spectrum was used to guide the experimental design of complex nanostructure.

A2. Darkfield Microscopy

The strong surface plasmon resonance of plasmonic nanoparticles makes them excellent light scattering. Notably, the optical cross-section is 4-5 orders magnitude greater than commonly used fluorophores.[4] For example, the scattering molar coefficient of 40-nm AuNP is 7.7 x 10^9 M^{-1} cm^{-1} compared to 1.1x 10^4 M^{-1} cm^{-1} indocyanine green and 1.2 x 10^5 M^{-1} cm^{-1} rhodamine fluorescein molecules.[5] Because of the high scattering cross-section, individual plasmonic NP can be easily visualized with a darkfield microscope. Along with the dramatic use of nanoparticles, darkfield microscopy becomes a typical technique for spectroscopy of a single nanoparticle.[6,7] In principle, a white light source illuminates the sample through a condenser. The scattered light is then collected through an objective and split to a true-color digital camera for acquiring images, as well as a spectrometer for single-particle scattering spectra. Both the darkfield microscope and the critical pieces will be discussed.

Two ways of set-up a darkfield microscope can be either invert (Figure A7a) or upright (Fig A7b). A typical darkfield microscope consists of a dark-field condenser, white light illumination, and a color charge-coupled device (CCD) camera or a spectrometer. Figure A7c illustrates the transmission of white light through the condenser equipped with a dark-field ring to produce a hollow cone of illumination at a large angle. With a large enough illumination angle, only a small amount of incident light can radiate the sample while most direct light is transmitted

through the sample and does not enter the objective lenses. By using an objective with a numerical aperture smaller than the dark-field condenser, only the scattered light from the sample will be collected by the objective lenses. As a result, the background appears dark, and only observe bright features that scatter the light. This differs from the brightfield microscopy where the solid-cone rather than hollow-cone illumination is incident on the sample. In brightfield microscopy, the features can be observed by two mechanisms – either transmitted through a transparent sample or reflected by a reflective sample. The transmitted or reflected light from the sample together with the incident light enters the objective lenses, as a result producing features on bright background. Commonly, plasmonic nanostructures cannot be imaged well with bright-field microscopy because their structure is much smaller than the diffraction limit of visible light and the light intensity of individual structures is relatively lower than the bright background. Moreover, the low noise of the dark image background has better signal-to-noise ratios than the bright image background. Therefore, the darkfield microscope works effectively for spectroscopy of nanostructures in such a way that only scattered light is collected when illumination, thus yielding high contrast images and spectra.

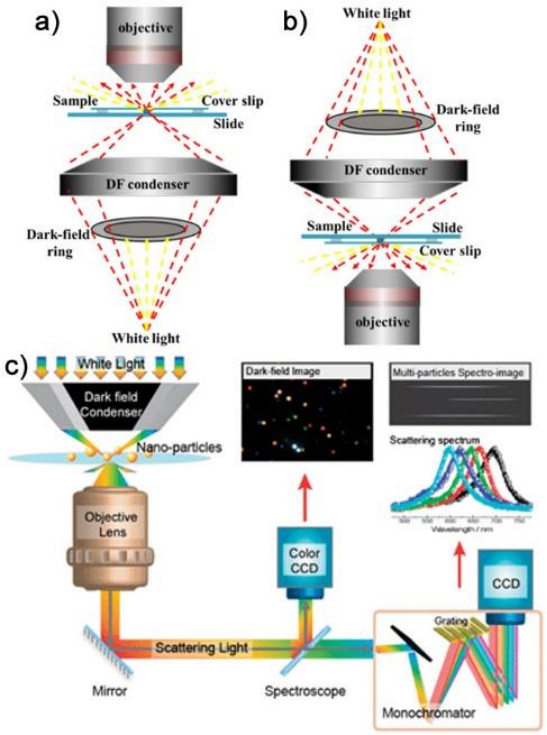

Figure A7. Upright (a) and invert (b) types of dark-field microscope. c) invert dark-field microscope coupled with color CCD for images or spectrometer for measurement of scattering spectrum. Reprinted with permission from ref 7 and ref 8.

A3. Image-Based Analysis of Plasmonic Nanoparticles

Along with the remarkable use of darkfield microscopy for a single nanoparticle, it is necessary to develop a more simple, rapid, and time-efficient method for data analysis of many nanoparticles. The traditional spectrometer with a monochromator is very straightforward and simple, but taking a single spectrum limits its application. Although the development of hyperspectral spectrometer could offer throughput acquisition of spectrum and increase scanning speed, the disadvantages such as complex design, lower light transmissivity, and expenses are considered of their use. The readout of the colors of single nanoparticles could be more efficient than obtaining individual spectra. The extract color-coded RGB (red/green/blue) or HSI (hue/saturation/intensity) using image processing is considering an alternative. Hundreds or even

thousands of single nanoparticles could be processed and/or converted to spectra. RGB and HSI methods will be discussed below.

A3.1 RGB (Red/Green/Blue) Color-Code Image Processing

With scattered colors of plasmonic nanoparticles, the RGB color-coded method is commonly used for image processing. The colors of scattering light are created by mixing three colors of red (R), green (G), and blue (B). In general, each R, G, and B color has 0–256 levels of brightness for a 24-bit image, thus we can get 256^3 = 16.8 million different colors. Each color can represent the values of chromaticity and intensity from red, green, and blue colors. For example, blue can be matched by (R G B) = (0 0 255), while the RGB values of (255 0 0) indicate that a light is red. Thus, using computer software (i.e. MathLab, Igor), the colors of the scattering light of individual nanoparticles can be decoded with the RGB system. These colors of scattering light are calculated using the following equations:

$$P_R = V_R/(V_R + V_G + V_B)$$

$$P_G = V_G/ (V_R + V_G + V_B)$$

$$P_B = V_B/(V_R + V_G + V_B) =1 - P_R – P_G$$

Wherein, P_R, P_G, and P_B are the percentages of R, G, and B color values (V_R, V_G, and V_B) of a particle, respectively. By mapping RGB values onto the chromaticity diagram, the RGB variance information of single nanoparticles can be converted to spectral wavelength by MathLab. For example, Jing *et al.*[9] measured the diameters of single AuNPs using simulated spectral wavelength from RGB value and they could obtain the spectral wavelengths of thousands of nanoparticles within 3 mins. Undeniably, RGB processing offers a rapid method compared with the spectrometer which could only record the spectra of 1−10 particles at once. In another application, the RGB method can also be used to study complex reactions. Liu *et al.*[10] studied the binding of thiols to single Au NPs by analyzing the color variance of the images of single Au nanoparticles. Hao *et*

al.[11] detected H_2S using individual spherical Au-Ag core-shell plasmonic nanoparticles by the spectrum shifts which are converted from color images. With the availability of sensitive digital color cameras nowadays, the readout of the colors of single nanoparticles could bring much attention because of the simple implementation and rapid technique for acquiring the scattering spectrum of a single nanoparticle.

A3.2 HSI (Hue/Saturation/Intensity) Color System

The hue-saturation-intensity (HSI) color system is also an attractive color-code model for image processing because it represents color similarly to human visual perception compared to RBG. Figure A8 illustrates the HSI color system, in which the intensity is the image brightness and the hue and saturation values express the aspect of the image – the hue represents the basic color (i.e. red, blue, yellow, purple, etc.) and the saturation is the amount of a given hue added to white (such as dark red, medium red, light red). In this representation, the hue component is given by an angular value ranging from 0 to 360 degrees, for example, red is 0^o, yellow is 60^o, green is 120^o, blue is 240^o, and magenta is 300^o; the saturation represents the level of mixing with the white color, which has the range of [0, 1]; the intensity represents the luminance information and ranges between [0, 1], for example, zero intensity is black, and full intensity white.

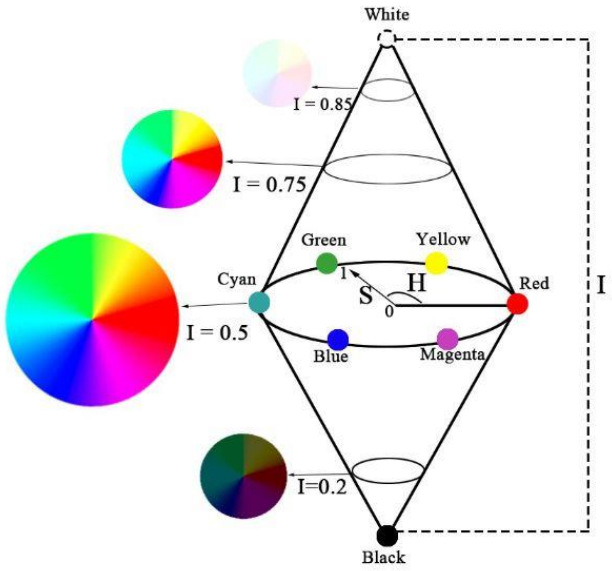

Figure A8. HSI (hue, saturation, and intensity) color model. The I axis represents the intensity of brightness changing from black to white. The H and S axes are polar coordinates on the plane orthogonal to I, in which H is the angle in this plane and represents the color (red is 0°, yellow is 60°, green is 120°, blue is 240°, and magenta is 300°). S is the magnitude of the color vector projected in the plane orthogonal to I and represents the difference between pastel colors (low saturation) and vibrant colors (high saturation). Reprinted with permission from ref 12.

The HSI coordinates can be transformed from the RGB following the equations:[13]

$$H = arctan(\frac{\sqrt{3(G-B)}}{(R-G)+(R-B)})$$

$$S = 1 - \frac{3[min(R,G,B)]}{R+G+B}$$

$$I = 1/3(R+G+B)$$

The hue values correspond to the spectrum and color of the scattered light, making it possible to use for analyzing the scattered light of images. The image processing based on hue value can be used to demonstrate the binding event. With the color change interpreted by hue value, Zhou *et*

al.[14] demonstrated the adsorption of DNA on the surface of AuNPs. The image processing technique is a promising approach for automated analysis. The color readouts can use to build the colorimetric-based algorithm that can create an artificial network for automatic analysis. For example, Liu *et al.* created the colorimetric algorithm of NP clusters and used them to classify the cluster size in the cellular uptake study.[15] The color algorithm was able to recognize the nanoparticles in the images and quantitatively measure their size. Additionally, the color scattered profile from NPs can train artificial networks (i.e machine learning or deep learning), which statistically learns to distinguish between the scattering light of plasmonic nanoparticles and background scattering signals in complex media. This deep learning approach was used to monitor the activity of protein Cyt c during apoptosis by recognizing the aptamer-functionalized gold nanorods in the living cells.[16] The imaging processing using HSI shows a promising technique in the potential for automatic analysis and throughput.

A4. References

(1) Oubre, C.; Nordlander, P. Finite Diference Time Domain Studies of Optical Properties of Nanoshell Structures. *Proceeding SPIE* **2003**, *5221*, 133–143.

(2) Choroszucho, A. Analysis of the Influence of the Complex Structure of Clay Hollow Bricks on the Values of Electric Field Intensity by Using the FDTD Method. *Arch. Electr. Eng.* **2016**, *65*, 745–759.

(3) Umashankar, K.; Taflove, A. A Novel Method to Analyze Electromagnetic Scattering of Complex Objects. *IEEE Trans. Electromagn. Compat.* **1982**, *24*, 397–405.

(4) Jain, P. K.; Huang, X.; El-Sayed, I. H.; El-Sayed, M. A. Review of Some Interesting Surface Plasmon Resonance-Enhanced Properties of Noble Metal Nanoparticles and Their Applications to Biosystems. *Plasmonics* **2007**, *2*, 107–118.

(5) Jain, P. K.; Lee, K. S.; El-Sayed, I. H.; El-Sayed, M. A. Calculated Absorption and Scattering Properties of Gold Nanoparticles of Different Size, Shape, and Composition: Applications in Biological Imaging and Biomedicine. *J. Phys. Chem. B* **2006**, *110*, 7238–7248.

(6) Gao, P. F.; Lei, G.; Huang, C. Z. Dark-Field Microscopy: Recent Advances in Accurate Analysis and Emerging Applications. *Anal. Chem.* **2021**, *93*, 4707–4726.

(7) Wang, H.; Zhang, T.; Zhou, X. Dark-Field Spectroscopy: Development, Applications and Perspectives in Single Nanoparticle Catalysis. *J. Phys. Condens. Matter* **2019**, *31*, 473001.

(8) Li, Y.; Jing, C.; Zhang, L.; Long, Y.-T.; Soc, C. Resonance Scattering Particles as Biological Nanosensors in Vitro and in Vivo. *Chem. Soc. Rev.* **2012**, *41*, 632–642.

(9) Jing, C.; Gu, Z.; Ying, Y. L.; Li, D. W.; Zhang, L.; Long, Y. T. Chrominance to Dimension: A Real-Time Method for Measuring the Size of Single Gold Nanoparticles. *Anal. Chem.* **2012**, *84*, 4284–4291.

(10) Liu, Y.; Ling, J.; Huang, C. Z. Individually Color-Coded Plasmonic Nanoparticles for RGB Analysis. *Chem. Commun.* **2011**, *47*, 8121–8123.

(11) Hao, J.; Xiong, B.; Cheng, X.; He, Y.; Yeung, E. S. High-Throughput Sul Fi de Sensing with Colorimetric Analysis of Single Au − Ag Core − Shell Nanoparticles. *Anal. Chem.* **2014**, *86*, 4663–4667.

(12) Zhou, J.; Gao, P. F.; Zhang, H. Z.; Lei, G.; Zheng, L. L.; Liu, H.; Huang, C. Z. Color Resolution Improvement of the Dark-Field Microscopy Imaging of Single Light Scattering Plasmonic Nanoprobes for MicroRNA Visual Detection. *Nanoscale* **2017**, *9*, 4593–4600.

(13) Cheng, H. D.; Jiang, X. H.; Sun, Y.; Wang, J. Color Image Segmentation: Advances and Prospects. *Pattern Recognit.* **2001**, *34*, 2259–2281.

(14) Zhou, J.; Lei, G.; Zheng, L. L.; Gao, P. F.; Huang, C. Z. HSI Colour-Coded Analysis of Scattered Light of Single Plasmonic Nanoparticles. *Nanoscale* **2016**, *8*, 11467–11471.

(15) Liu, M.; Mao, X.; Huang, L.; Fan, C.; Tian, Y.; Li, Q. Automated Nanoplasmonic Analysis of Spherical Nucleic Acids Clusters in Single Cells. *Anal. Chem.* **2020**, *92*, 1333–1339.

(16) Song, M. K.; Chen, S. X.; Hu, P. P.; Huang, C. Z.; Zhou, J. Automated Plasmonic Resonance Scattering Imaging Analysis via Deep Learning. *Anal. Chem.* **2021**, *93*, 2619–2626.

List of Publications

(4) **Le, N. H.**; Cathcart, N.; Kitaev, V.; Chen, J. I. L. Core-satellite assembly of gold nanoshells on solid gold nanoparticles for a color coding plasmonic. *Analyst* **2022**, 147, 155-164.

(3) Ghotra, G.; **Le, N. H.**; Hayder, H.; Peng, C.; Chen, J. I. L. Multiplexed and Single-Cell Detection of MicroRNA with Plasmonic Nanoparticle Assemblies. *Can. J. Chem.* **2021**, *99*, 585–593.

(2) **Le, N. H.**; Ye, G.; Peng, C.; Chen, J. I. L. Metabolic Mapping with Plasmonic Nanoparticle Assemblies. *Analyst* **2020**, *145*, 2586–2594. (Themed collection: Analytical Nanoscience)

(1) **Le, N. H.**; Nguyen, B. K.; Ye, G.; Peng, C.; Chen, J. I. L. Tuning the Sensing Performance of Multilayer Plasmonic Core-Satellite Assemblies for Rapid Detection of Targets from Lysed Cells. *ACS Sensors* **2017**, *2*, 1578–1583.